Politecnico di Torino

Master's degree in mechanical engineering A.a. 2024/2025

Additive Manufacturing of Graded TPMS and Voronoi Lattices in AlSi10Mg: From Design to Mechanical Characterization

Academic Supervisor:

Prof. Abdollah Saboori

Candidate:

Alireza Kavei

Master Thesis

Abstract

Additive Manufacturing of Graded TPMS and Voronoi Lattices in AlSi10Mg: From Design to Mechanical Characterization

Alireza Kavei

Politecnico Di Torino

Mechanical Engineering Master science

Supervisor: Prof. Abdollah SABOORI

Co-supervisor: Mohammad Taghian Todeshki

2025

Laser Powder Bed Fusion (LPBF), a type of additive manufacturing, allows for the production of metallic lattice structures with highly adaptable geometries and graded material properties. Functionally Graded Lattice Structures (FGLS) are advantageous for high-performance applications, including biomedical implants. These advanced structures, produced through additive manufacturing (AM), exhibit spatially varying mechanical properties that are crucial for mimicking biological gradients, thereby reducing stress shielding and promoting better integration. This thesis explores the design, fabrication, and mechanical characterization of FGLS using AlSi10Mg, targeting potential biomedical applications. Three advanced lattice topologies were investigated: Gyroid, Split-P (a TPMS-derived surface), and Stochastic Voronoi, selected for their known mechanical performance and bioinspired architectures. Tensile (dog-bone shaped) and compression (cubic) specimens were fabricated via LPBF, with functional gradation introduced by varying strut and wall thickness along the specimen length. The mechanical properties, including elastic modulus, ultimate tensile and compressive strength, and energy absorption, were evaluated through quasi-static tensile and compression tests. High-resolution computed tomography (CT) scans were used to capture the as-built geometry, verify dimensional accuracy, and identify potential manufacturing defects. These images were further analyzed to assess internal fidelity, strut thickness deviations, and porosity, supporting the mechanical testing with geometric validation. This study fills a critical gap by directly comparing Gyroid, Split-P, and Stochastic Voronoi FGLS structures, all fabricated identically but with varying design parameters.

Keywords: Functionally Graded Lattice Structures (FGLS); Structural Metamaterials; Laser Powder Bed Fusion (LPBF); Design for Additive Manufacturing (DfAM).

Contents

1 Introduction

1.1 Overview of Additive Manufacturing

Additive Manufacturing (AM), commonly known as 3D printing, is a paradigm shift in manufacturing, fundamentally changing how we conceive, design, and produce physical objects [1]. Unlike traditional subtractive manufacturing processes, which create a final product by methodically removing material from a larger block, such as through milling, turning, or grinding, additive manufacturing constructs objects layer-by-layer directly from a digital model [2]. This concept of adding material to only where it is needed offers unprecedented design freedom, enables the creation of highly complex geometries, and provides a pathway for rapid prototyping, customized production, and decentralized manufacturing [3,4]. The process begins with a three-dimensional digital design, typically created using Computer-Aided Design (CAD) software. This CAD model is then converted into a standardized file format, most commonly the stereolithography (STL) format, which approximates the surfaces of the model with a mesh of triangles. Specialized software then slices this digital file into hundreds or thousands of thin, two-dimensional cross-sectional layers (Figure 1). These layers serve as a precise blueprint that the AM machine follows, depositing, fusing, or solidifying material sequentially to build the final part from the bottom up [5]. Many different AM technologies exist, each using unique methods, materials, and applications, but they are all united by their layer-wise approach [6].
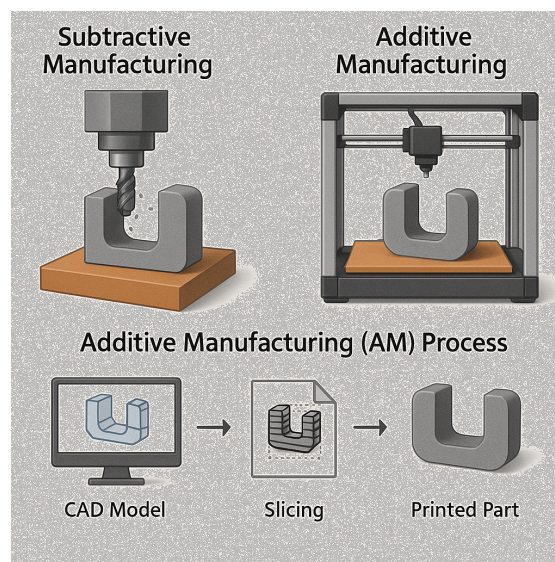

Figure 1) Subtractive vs. Additive manufacturing and the steps of AM process, Image generated using AI.

The term "Additive Manufacturing" is the official industry standard established by the ASTM International Committee F42 on Additive Manufacturing Technologies, chosen to reflect the process's industrial capabilities beyond just visualization or prototyping [7]. The formal definition provided by ASTM specifies AM as a "process of joining materials to make objects from 3D model data, usually layer upon layer, as opposed to subtractive manufacturing methodologies". This crucial difference separates manufacturing complexity from cost because of the additive approach. In subtractive manufacturing, creating intricate internal features, lattice structures, or organically shaped components can be prohibitively expensive or technologically impossible due to tool access limitations [8]. Alternatively, AM creates these complex features inexpensively and quickly since their complexity is managed by the digital slicing algorithm and layer-by-layer deposition. This capability has profound implications for mechanical engineering, enabling the design of components that are optimized for performance rather than for manufacturability. For instance, engineers can design parts with internal cooling channels that follow the component's contours, create lightweight structures with topologically optimized internal lattices, or consolidate multiple individual parts into a single, complex assembly, thereby reducing weight, assembly time, and potential points of failure [9].

The historical roots of additive manufacturing can be traced back to the early 1980s, a period of intense innovation in digital manufacturing technologies. The first patented and commercialized AM technology was Stereolithography (SLA), invented by Charles (Chuck) W. Hull in 1984, who subsequently co-founded 3D Systems [10]. Hull's invention utilized a UV laser to selectively cure and solidify photopolymer resin in a vat, layer by layer. This innovative work created the base for the whole field and showed that building physical objects directly from digital information is achievable. Around the same time, other core AM processes were also being developed. In 1988, Carl Deckard at the University of Texas at Austin filed a patent for Selective Laser Sintering (SLS), a powder bed fusion process that uses a laser to sinter powdered material, initially polymers [11]. This was a significant advancement as it expanded the material palette beyond photopolymers and eliminated the need for support structures for many geometries, as the surrounding powder bed provided inherent support [12]. Shortly thereafter, in 1989, S. Scott Crump invented Fused Deposition Modeling (FDM), another landmark technology that he commercialized through his company, Stratasys [13]. FDM works by extruding a thermoplastic filament through a heated nozzle, depositing the molten material layer by layer in a path defined by the digital model. Because of its ease of use, low cost, and the use of durable thermoplastics, it quickly became one of the most popular additive manufacturing technologies, primarily for rapid prototyping and later, for final products [14]. SLA, SLS, and FDM—three foundational technologies—underpinned the additive manufacturing industry (Figure 2), establishing the core principles of vat polymerization, powder bed fusion, and material extrusion.

Throughout the 1990s and early 2000s, the field continued to evolve with the introduction of new technologies and the refinement of existing ones, largely operating under the umbrella term of "Rapid Prototyping". Visual models and functional prototypes were the key application of this era, significantly

accelerating product development by providing engineers and designers with the ability to physically interact with and test their ideas more swiftly than previously possible using traditional methods [15].
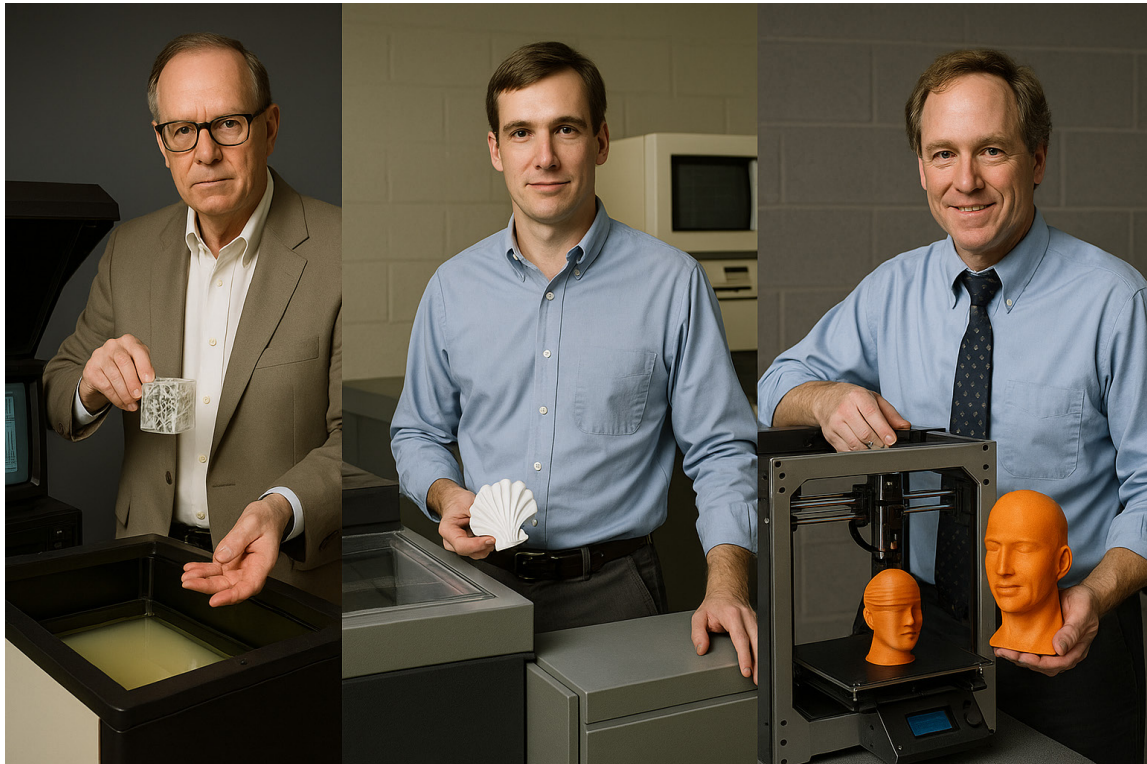

Figure 2) Pioneers of 3D Printing (Image generated using AI) : Chuck Hull with the first SLA machine, Carl Deckard beside an early SLS system, and S. Scott Crump demonstrating FDM technology—each showcasing the revolutionary inventions that laid the foundation of additive manufacturing.

Technologies such as Laminated Object Manufacturing (LOM), which builds parts by laminating and cutting sheets of material, and Solid Ground Curing (SGC) emerged, though they ultimately saw less commercial success [16]. A significant milestone was the development of direct metal printing technologies. The first commercially viable metal AM system, based on Selective Laser Melting (SLM), a full-melting variant of SLS, was developed at the Fraunhofer Institute ILT in Germany in the mid-1990s [17]. This innovation enabled the utilization of AM in the production of high-performance, functional metal components for demanding sectors such as aerospace and medicine, extending its application beyond prototyping. The expiration of key patents, starting with the FDM patent in 2009, triggered a surge of innovation and competition, dramatically lowering the cost of entry-level AM systems and contributing to the rise of the "maker movement" [18]. The widespread adoption of the technology boosted public awareness and the availability of desktop 3D printers, alongside continued advancements in the speed, precision, and material capabilities of industrial systems. Today, additive manufacturing is a fully developed manufacturing solution, impacting nearly all sectors by transforming supply

chains, business models, and engineering design; this contrasts sharply with its early days as a niche prototyping technology [19].

In order to bring clarity and consistency to this rapidly evolving field, the ASTM F42 committee has developed a seven-category classification system for AM processes. This framework is crucial for engineers to understand the capabilities and limitations of different technologies and to select the appropriate process for a given application [29]. The seven categories are: Vat Photopolymerization, Material Jetting, Binder Jetting, Material Extrusion, Powder Bed Fusion, Sheet Lamination, and Directed Energy Deposition as presented in Figure 3 [7].
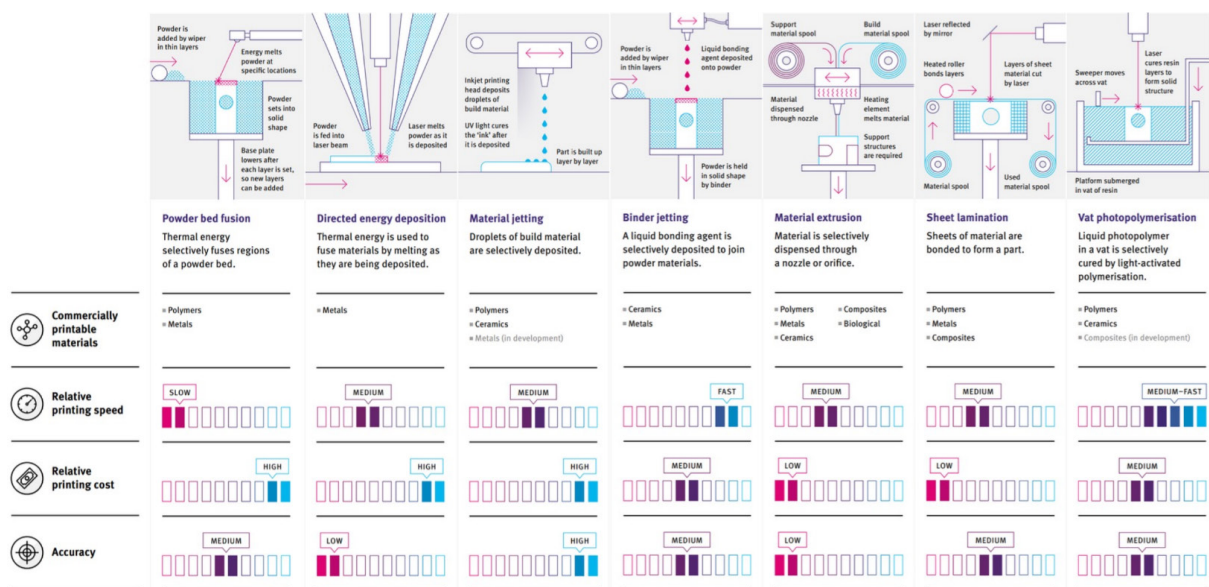

Figure 3) Overview and comparison of additive manufacturing (AM) processes based on operating principles, compatible materials, printing speed, cost, and accuracy [20].

Vat Photopolymerization processes build parts by selectively curing liquid photopolymer resin using light-activated polymerization. Stereolithography (SLA) is the archetypal process, using a UV laser to trace the cross-section of a layer onto the surface of the resin. Newer variations, such as Digital Light Processing (DLP), use a digital projector to expose the entire layer at once, significantly increasing build speed [21]. These processes are known for producing parts with exceptional surface finish and fine feature detail, making them ideal for visual prototypes, dental and medical models, and casting patterns [22].

Material Jetting mimics a 2D inkjet printer but uses photopolymer or wax droplets instead of ink. These droplets are deposited onto a build platform and cured immediately by a UV light source accompanying the print head. This technique produces highly accurate parts, combining various materials and colors in a single build to create realistic, multi-material prototypes and anatomical models [23].

8

Binder Jetting uses a print head to selectively deposit a liquid binding agent onto a thin layer of powdered material—which can be sand, metal, or ceramic. The binder "glues" the powder particles together to form a cross-section of the part [24]. The process is repeated layer by layer, and once complete, the part is in a "green" state, held together by the binder. For metal parts, a secondary post-processing step, such as sintering or infiltration with a low-melting-point metal like bronze, is required to achieve final density and strength [25]. A key advantage of binder jetting is its speed and its ability to produce large parts, avoiding the residual stresses commonly found in fusion processes [26].

Material Extrusion, of which Fused Deposition Modeling (FDM) is the most common example, involves feeding a continuous filament of thermoplastic or composite material through a heated nozzle. The nozzle melts the material and extrudes it onto the build platform, tracing the layer's geometry. The material cools and solidifies, fusing to the layer below [27]. The technology is prized for its ease of use, dependability, and the wide array of materials available, including common plastics (ABS and PLA), high-performance polymers (PEEK and ULTEM), and composites reinforced with carbon fiber or glass [28].

Powder Bed Fusion (PBF) encompasses a range of technologies that use thermal energy to selectively fuse regions of a powder bed. This encompasses polymer processes like Selective Laser Sintering (SLS), and metal processes such as Selective Laser Melting and Electron Beam Melting. While SLS uses a laser to sinter polymer particles, SLM and EBM utilize lasers or electron beams, respectively, to fully melt and consolidate metallic powders, achieving densities greater than 99% in many cases [29]. PBF processes are a dominant force in industrial AM, used to produce complex, lightweight, and robust end-use parts for aerospace, automotive, and medical implant applications.

Sheet Lamination builds objects by stacking and bonding thin sheets of material. The shape of each layer is cut, typically by a laser or a knife, either before or after bonding. Materials can range from paper and plastics to metal foils [30]. While not as common today for structural parts, this process is very fast and low-cost for producing large-scale visual models. A modern variant, Ultrasonic Additive Manufacturing (UAM), uses ultrasonic vibrations to weld thin metal foils together at low temperatures, allowing for the embedding of electronics and sensors within solid metal structures [31].

Finally, Directed Energy Deposition (DED) involves melting material as it is being deposited, often through a nozzle mounted on a multi-axis arm. A focused thermal source, such as a laser or electron beam, creates a melt pool on the substrate, and powdered or wire feedstock is fed directly into that melt pool, where it melts and solidifies [32]. DED is not limited to building chambers and can be used to add features to existing large components or to repair high-value parts, such as turbine blades or molds. It is characterized by high deposition rates and the ability to create large metal parts, making it a key technology for repair and hybrid manufacturing applications [33].

1.2 Materials in Additive Manufacturing

The portfolio of materials available for additive manufacturing has expanded dramatically, moving far beyond the early photopolymers and waxes to include a vast array of engineering-grade polymers, metals, ceramics, and composites [34]. The choice of material is inextricably linked to the chosen AM process and is a critical determinant of the final part's mechanical properties, thermal resistance, chemical stability, and cost [35]. In the realm of polymers, thermoplastics are the most widely used, particularly in material extrusion processes. Acrylonitrile Butadiene Styrene (ABS) and Polylactic Acid (PLA) are frequently used in prototyping because they are both inexpensive and easy to 3D print [36]. For more demanding engineering applications, high-performance thermoplastics such as Polyetheretherketone, and Polyamides like PA, or nylon are employed. These materials offer superior mechanical strength, high-temperature resistance, and chemical inertness, making them suitable for functional parts in automotive and aerospace industries. Thermosetting polymers, or photopolymers, are the foundation of vat photopolymerization. These resins can be formulated to exhibit a wide range of properties, from soft and flexible elastomers to hard, stiff, and high-temperature-resistant materials that can mimic engineering plastics [37].

Metal additive manufacturing has revolutionized the production of complex, high-value components. The most commonly used metal alloys in PBF and DED processes include titanium alloys (e.g., Ti-6Al-4V), which are favored in aerospace and medical implants for their high strength-to-weight ratio and excellent biocompatibility [38]. Nickel-based superalloys, such as Inconel 718 and 625, are used for parts that must operate in extreme environments, such as jet engine components and gas turbines, due to their outstanding high-temperature strength and corrosion resistance [39]. Stainless steels (e.g., 316L) and tool steels (e.g., H13) are widely used for industrial tooling, fixtures, and corrosion-resistant components due to their good mechanical properties and processability. Aluminum alloys (e.g., AlSi10Mg) offer lightweighting solutions for the automotive and aerospace sectors, while cobalt-chrome alloys are prevalent in dental and orthopedic implants [40]. The layer-by-layer fabrication and rapid solidification inherent in metal AM processes result in unique, fine-grained microstructures that often lead to mechanical properties superior to those of traditionally cast or even wrought materials [41]. However, these processes can also introduce challenges such as residual stresses, porosity, and anisotropy, which must be carefully managed through process parameter optimization and post-processing treatments like heat treatment or Hot Isostatic Pressing (HIP) [42].

Ceramics, known for their extreme hardness, high-temperature stability, and chemical resistance, are also being integrated into the AM landscape, although they present significant challenges due to their brittle nature and very high melting points [43]. AM of ceramics is typically achieved through indirect methods, such as binder jetting, material jetting, or vat photopolymerization of a ceramic-loaded polymer slurry (a process known as stereolithography of ceramics or LCM) [44]. The initial, "green" part requires a multi-stage post-processing cycle. This involves debinding—removing the polymer binder—followed by high-temperature sintering to densify the ceramic and create a functional component. This allows the creation of intricate ceramic parts, such as customized medical implants (e.g., zirconia or hydroxyapatite), catalyst supports, and investment casting

cores—items that would be challenging or impossible to produce using traditional ceramic forming methods [44]. Figure 4 shows some examples of using ceramic materials in AM.
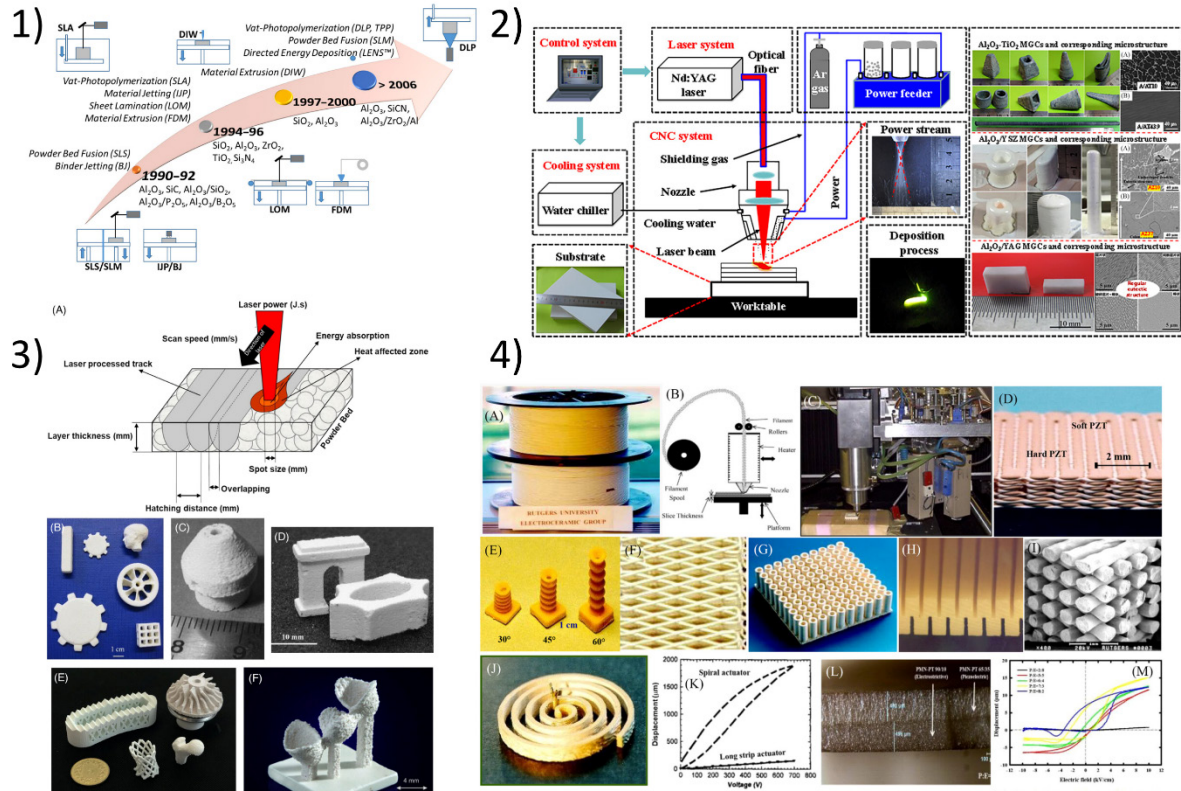

Figure 4) The additive manufacturing of ceramics [45]; 1) A brief overview of early attempts made for ceramic AM. 2) Schematic representation of the laser-directed energy deposition (LDED) system and typical deposition structures. 3) An overview of the SLS/M process and various parts fabricated via SLS/M. 4)The fused deposition of ceramics™ (FDC™) process.

Additive manufacturing is also expanding into composites (Figure 5), allowing for parts with custom properties through material combinations. Reinforcing a polymer matrix with short or continuous fibers is the most frequent approach. The stiffness and strength of base polymers are significantly increased by using material extrusion systems adapted to print with thermoplastic filaments filled with chopped carbon fibers, glass fibers, or carbon nanotubes. A more advanced technique involves the simultaneous extrusion of a thermoplastic and a continuous fiber reinforcement (e.g., carbon, glass, or Kevlar), allowing for the strategic placement of fibers along critical load paths to create exceptionally strong and lightweight components [46]. The ability to mix different base photopolymers at the voxel level, a feature of multi-material jetting technologies, allows for the creation of "digital materials"-composites with precisely tailored mechanical properties, gradients, or

functionalities. This ability to design materials at a microstructural level opens up new possibilities for creating functionally graded materials and complex multi-functional devices [47].
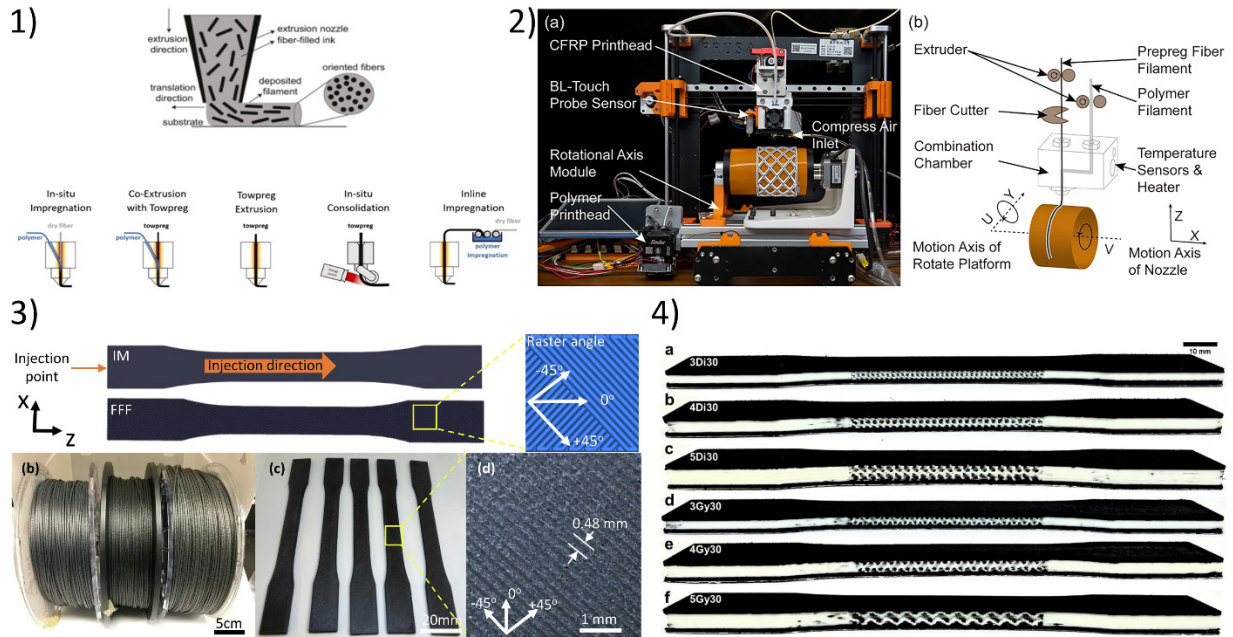

Figure 5) The additive manufacturing of composites; 1) Material extrusion of short fiber reinforced composites and different material extrusion of continuous fiber reinforced composites [48]. 2) The workflow of the surface mapping based conformal path planning method with geometry calibration [49]. 3) Schematic of a dog-bone specimen along with images of composite filaments and FFF printed ASTM specimens [50]. 4) Printed specimens of the composite sandwich cellular structures at different unitcell sizes [51].

Additive manufacturing is increasingly becoming more industrialized, automated, and integrated into digital manufacturing. The focus of current technological trends is on improving speed, reliability, and repeatability, and broadening the scope of usable materials. Hardware advancements, including multi-laser PBF systems and improved print heads, are dramatically shortening production times, thus enhancing AM's competitiveness in mass manufacturing. In-situ monitoring systems using cameras and pyrometers to track each layer in real time are vital for ensuring part quality and obtaining certification for critical applications [52]. The wealth of data, coupled with machine learning, enables self-correcting AM systems capable of real-time defect detection and mitigation, transitioning from inspection to comprehensive quality assurance [53]. Furthermore, significant research is focused on developing new materials specifically designed for AM processes, moving beyond simply adapting existing materials to creating alloys and polymers that leverage the unique thermal cycles of AM to achieve unprecedented properties. As technology matures, its role is expanding beyond prototyping and niche manufacturing; it's becoming a standard production method, spurring innovation in areas

including personalized medicine, sustainable energy, resilient supply chains, and aerospace. The principles of AM are not just changing how parts are made, but are fundamentally reshaping how engineers think about design, enabling a future where complexity is free and products are limited only by the human imagination.

1.3 Design for Additive Manufacturing

Design for Additive Manufacturing (DfAM) is a specialized product development approach that uses the strengths of additive manufacturing (AM) while addressing its limitations. DfAM breaks free from the geometric constraints of traditional manufacturing, using layer-by-layer fabrication to create designs previously considered impossible [54]. This new design philosophy extends beyond just adapting existing designs for AM processes; it fundamentally rethinks product architecture to maximize performance, reduce material consumption, and consolidate parts, thereby unlocking significant advantages in weight reduction, functional integration, and customization. DfAM's core capability lies in creating intricate internal geometries, complex curves, and structures with varying densities, enabling engineers to explore manufacturing limits and optimize parts for specific functions [55].

The shift from Design for Manufacturing (DfM) principles, which typically emphasize simplicity, ease of assembly, and manufacturability through conventional methods like machining, casting, or molding, is profound [56]. In contrast to traditional methods, DfAM handles complexity efficiently, allowing for the creation of organically shaped parts, lattice structures, and integrated functionalities without the usual high costs. This allows for parts with high strength-to-weight ratios, improved thermal management, and better energy absorption, all achieved through strategic micro- and macro-scale design of internal and external geometry [57]. Furthermore, DfAM facilitates part consolidation, where multiple components of an assembly can be redesigned and manufactured as a single, monolithic unit, thereby reducing assembly time, minimizing potential failure points, and simplifying supply chains [58]. The Figure 6 illustrates moving from DfM to DfAM.
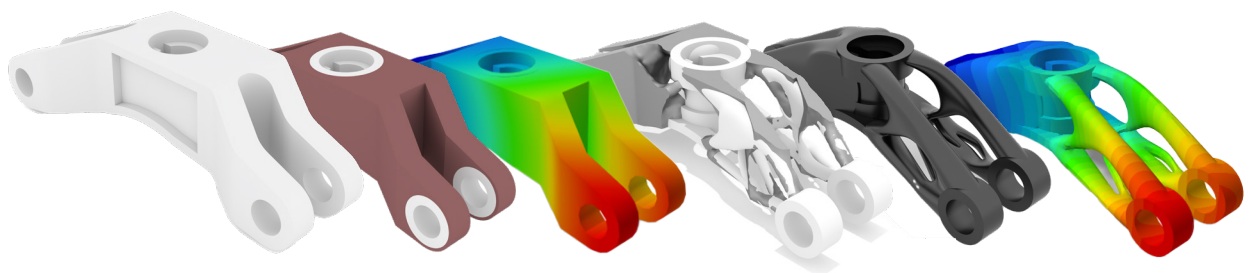

Figure 6) Transition from DfM to DfAM, moving from left to right.

A strong understanding of the chosen AM process, its materials, and its potential for anisotropy and defects is crucial for effective DfAM. For instance, considerations such as build orientation, support structure requirements, residual stresses, and post-processing steps are integral to the design phase, as they significantly influence the final part quality, mechanical performance, and cost [59]. Designers use computational tools, including topology optimization, generative design, and simulation, to significantly improve DfAM. These tools allow exploration of a vast design space to identify optimal geometries that meet performance criteria while adhering to manufacturing constraints [60]. The creation of highly efficient, lightweight, and organically-shaped, bionic structures, inspired by nature, is enabled by these tools. The integration of these advanced design methodologies with AM technologies is continuously expanding the applications of additive manufacturing beyond prototyping into the realm of high-performance end-use components across diverse industries, from aerospace and medical to automotive and consumer goods [61].

1.4 Lattice Structures in Additive Manufacturing

Because of their special properties and the freedom of AM design, lattice structures are playing a larger role in DfAM. These structures, Figure 7, are typically composed of repeating unit cells, forming a network of interconnected struts or surfaces that occupy a fraction of the total volume while providing structural integrity [62]. The primary motivation behind using lattice structures is to achieve exceptional strength-to-weight ratios, making them ideal for lightweight applications in aerospace, automotive, and medical implants. The substitution of solid material with strategically designed voids in lattice structures allows for considerable mass reduction in components, while maintaining or even improving mechanical properties.

Lightweighting is just one advantage of lattice structures; they also offer a wide array of functionalities unattainable with solid materials. Their high surface area-to-volume ratio makes them excellent candidates for applications requiring efficient heat transfer, such as heat exchangers and thermal management systems [63]. For biomedical applications, the porous interconnected structure of many lattice designs is highly advantageous, facilitating bone ingrowth within implants, acting as a scaffold for tissue engineering, and enabling drug delivery. Moreover, the ability of lattices to absorb significant energy makes them suitable for applications requiring crashworthiness, such as protective gear, where controlled deformation dissipates kinetic energy [64]. The ability to tailor the mechanical response of a component by varying the geometry, size, and type of unit cell within the lattice structure provides unprecedented design flexibility.

Despite their numerous advantages, the design and fabrication of lattice structures present unique challenges. The geometric complexity requires advanced computational design tools and sophisticated AM processes capable of accurately reproducing intricate features. Simulation and analysis of lattice structures are computationally intensive due to their highly heterogeneous nature [62]. Furthermore, post-processing considerations, such as the removal of uncured powder or support structures from the internal voids, can be complex and time-consuming, impacting manufacturing efficiency and cost. However, continued research and

development in AM technologies, materials science, and computational design are increasing the use of lattice structures in various engineering applications.
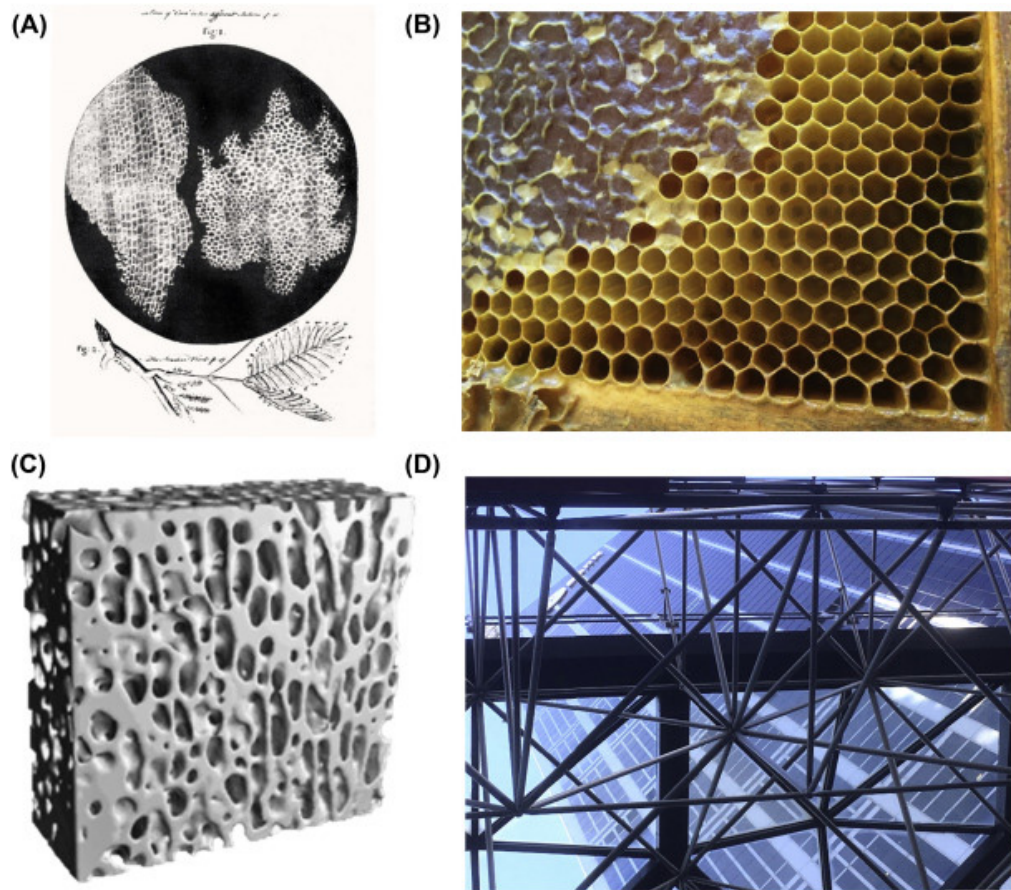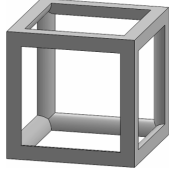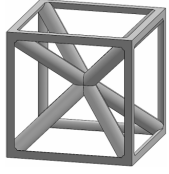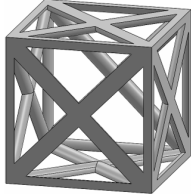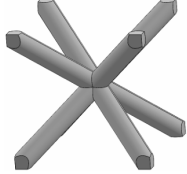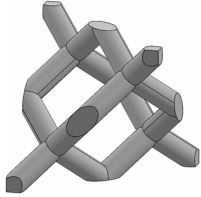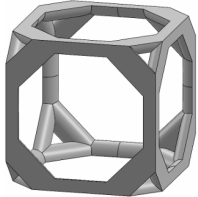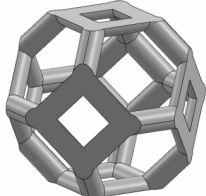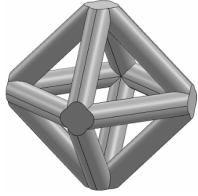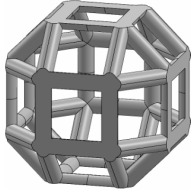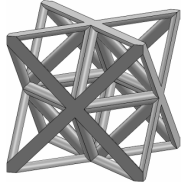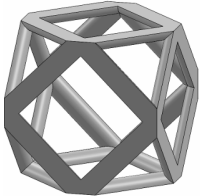

Figure 7) Cellular and lattice structures [65]: (A) First observation of a cellular structure, reported for cork by Robert Hooke in 1665, (B) open hexagonal cellular structure of honeycomb, partially filled with honey, (C) naturally occurring lattice structure observed in trabecular bone, (D) civil engineering lattice used to efficiently span space (note pin-jointed connections).

1.4.1 Common Lattice Structure Types

Various lattice structures have been developed and explored for additive manufacturing, each offering distinct advantages based on their geometric configuration and resulting mechanical properties. These can broadly be categorized into strut-based (or truss-based) lattices and surface-based lattices, with each type optimized for different functional requirements. Table 1 shows 11 types of unit cells, including simple cubic, body-centered cubic, face-centered cubic, body center, diamond, truncated cube, truncated octahedron (a.k.a. Kelvin), octahedron, rhombicuboctahedron, octet-cross (a.k.a. octet-truss), and cuboctahedron [66].

15

Table 1) Unit cell types considered for the lattice generation [66].

Unit Cell Topology	Image	Unit Cell Topology	Image
Simple cubic		Body-centered cubic	
Face-centered cubic		Body center	
Diamond		Truncated cub	
Truncated octahedron (a.k.a. Kelvin)		Octahedron	
Rhombicuboctahedron		Octet-cross (a.k.a. octet-truss)	
Cuboctahedron			

Strut-based lattices are characterized by a network of interconnected beams or struts that form the structural framework. They are often derived from basic geometric tessellations and can be designed to exhibit specific mechanical responses [67]. The Body-Centered Cubic (BCC) unit-cell consists of eight corners and one central node, with struts connecting the central node to each corner. Variants such as BCC-Z, in which vertical struts are added, are also common. BCC structures generally offer good stiffness and strength, particularly in

compression, and can be relatively easy to print with certain additive manufacturing (AM) processes. However, they may exhibit anisotropy and have limitations in energy absorption compared to more complex designs [68].

The Face-Centered Cubic (FCC) unit cell, on the other hand, has nodes at each corner and at the center of each face, with struts connecting these nodes. FCC structures are suitable for energy absorption applications due to their ability to deform plastically and their ductility [69]. However, their angled struts can complicate printing and may need extra support.

The Octet-Truss is a highly stiff and strong lattice structure derived from the octahedral tessellation, with struts arranged in a manner that provides high isotropic stiffness. This high-performing structure excels under compression and tension, making it ideal for aerospace applications demanding high specific strength and stiffness [70]. Manufacturing the Octet-Truss can be challenging due to its complex geometry, particularly the overhangs and the need to remove support structures.

Another noteworthy strut-based structure is the Kelvin cell, also referred to as the Weaire–Phelan structure. Though often considered a polyhedral or cellular structure, it can be represented as a strut-based lattice composed of truncated octahedra and irregular hexagons that form a space-filling tessellation [71]. This geometry's superior energy absorption and nearly uniform mechanical properties make it ideal for applications like impact absorption and foams.

Honeycomb structures are known for their hexagonal cells, similar to a natural honeycomb. While traditionally used in two-dimensional sandwich panel cores, three-dimensional honeycomb-like architectures can also be generated and fabricated through AM techniques. These structures offer exceptionally high out-of-plane stiffness and strength relative to their density, and they are highly efficient at distributing loads when compressed perpendicular to the cell walls [72]. Nevertheless, the mechanical response of honeycomb lattices is highly anisotropic, displaying significant directional dependence on the applied load. Additionally, fabricating complex 3D honeycombs with precise cell geometries can be challenging, particularly in achieving consistent wall thickness and corner radii [73]. Honeycomb structures are widely used in sandwich panels for aerospace and automotive applications that require lightweighting and directional energy absorption, even with their limitations.

1.4.2 Triply Periodic Minimal Surface Structures

Triply Periodic Minimal Surfaces (TPMS) represent a distinct and highly advantageous class of lattice structures for additive manufacturing, offering superior performance characteristics compared to many strut-based or honeycomb designs [74]. Minimal surfaces are defined as surfaces with zero mean curvature everywhere, meaning they locally minimize their surface area (Figure 8). TPMS are a type of minimal surfaces that are triply periodic, repeating in three directions to create a complex network dividing space into two regions. This unique topological property ensures a smooth, continuous surface without self-intersections, which is

highly beneficial for AM fabrication by minimizing stress concentrations and enabling self-supporting geometries [75].
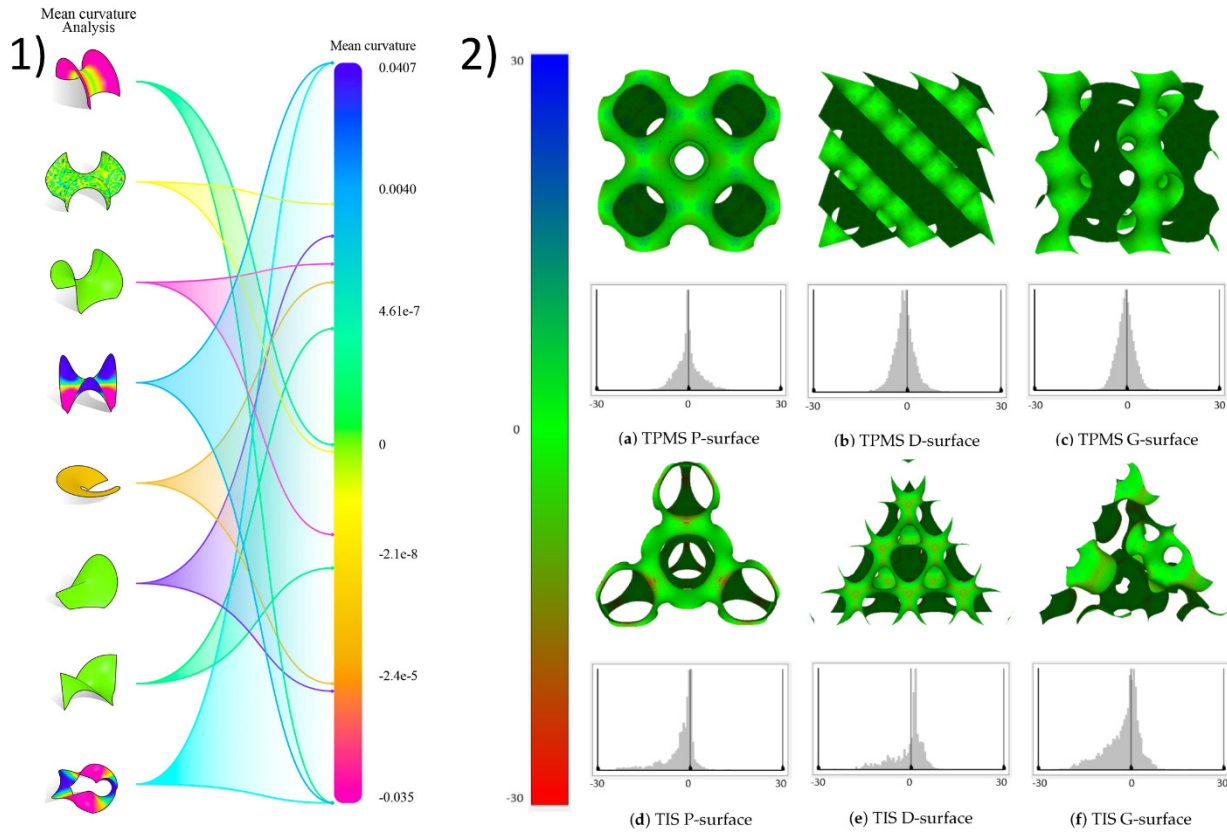
Figure 8) Illustration of a zero mean curvatures; 1) Pool of surfaces analysis of mean curvature [76]. 2) Distribution maps of the mean curvature and corresponding histograms for TPMSs and tetrahedral implicit surface (TIS) [77].

The continuous and smooth nature of TPMS structures provides several advantages over traditional strut-based lattices. Firstly, the absence of sharp corners and junctions, common in strut-based designs, leads to a more uniform stress distribution and reduces stress concentrations, thereby enhancing fatigue resistance and overall structural integrity. Secondly, the smooth, interconnected channels within TPMS structures promote efficient fluid flow and mass transport, making them ideal for applications such as heat exchangers, filters, and biomedical scaffolds where fluid permeability and high surface area are critical [78]. Moreover, many AM-fabricated TPMS structures are self-supporting, especially those made using powder bed fusion, minimizing the need for support, simplifying post-processing, and reducing waste. The self-supporting property is a consequence of their intricate curvature and continuous surfaces, which typically meet the critical angle requirements for overhangs in additive manufacturing processes [79].

The mechanical properties of TPMS structures can be tailored by manipulating parameters such as unit cell size, wall thickness, and relative density. They often exhibit more isotropic mechanical responses compared to other lattice types, which is desirable in applications where loads can come from various directions. Their biomimetic potential, mirroring structures found in natural materials like cancellous bone, also makes them highly attractive for biomedical engineering [80]. Among the myriad of TPMS structures, Gyroid, Primitive (P), and Diamond (D) are the most commonly studied, along with more recent developments like the Split-P and stochastic Voronoi.

The Gyroid surface, illustrated in Figure 9, is arguably the most widely studied and utilized triply periodic minimal surface structure in additive manufacturing due to its exceptional properties and ease of fabrication [81]. Mathematically, it can be approximated by the implicit equation: $sin(x)cos(y) + sin(y)cos(z) + sin(z)cos(x) = C$, where C is a constant that controls the surface thickness. The Gyroid consists of a continuous, non-orientable surface that separates space into two equally complex and distinct, but interconnected, channels. It is known for its highly isotropic mechanical properties, meaning its response to loads is largely independent of direction. This isotropy, combined with its smooth and continuous surfaces, makes it highly resilient to stress concentrations, contributing to superior fatigue performance [82]. Crucially for AM, the Gyroid structure is largely self-supporting, allowing for its fabrication with minimal or no additional support structures in many AM processes, particularly in powder bed fusion. Because of its unique interconnected channels, fluid flows efficiently, making it perfect for applications requiring efficient thermal exchange or distribution. Gyroid lattices are extensively explored for lightweight structural components in aerospace and automotive industries, high-efficiency heat exchangers, biomedical implants—due to biocompatibility and porosity for bone ingrowth—and as scaffolds for tissue engineering. Its smooth surface also aids in cleaning and sterilization in medical applications [83].

The Primitive (P) TPMS, often referred to as the Schwarz Primitive (P), is another fundamental minimal surface, mathematically described by the implicit equation: $cos(x) + cos(y) + cos(z) = C$. The Primitive surface forms a network of straight, orthogonal channels that are highly interconnected and extend along the principal axes [87]. This results in a simpler, more rectilinear morphology compared to the Gyroid. While the classic Primitive surface creates relatively uniform channels, the Split-P refers to design variations that modify these channels, to achieve specific flow characteristics or tailored anisotropic mechanical responses [88]. Due to its aligned channels, the Primitive and its variants can lead to more directional mechanical properties, with stronger responses along the channel directions. The well-defined and separate channels are advantageous in applications where predictable fluid flow or load-bearing capacity along specific axes are needed. As with other TPMS, its smooth surfaces contribute to reduced stress concentrations. Primitive and Split-P structures are explored for filtering applications, heat exchange where directional flow is beneficial, and structural components where tailored anisotropy might be desirable [89]. Their distinct channel architecture can also make them suitable for microfluidic devices or bioreactors, allowing for controlled fluid transport paths.

19
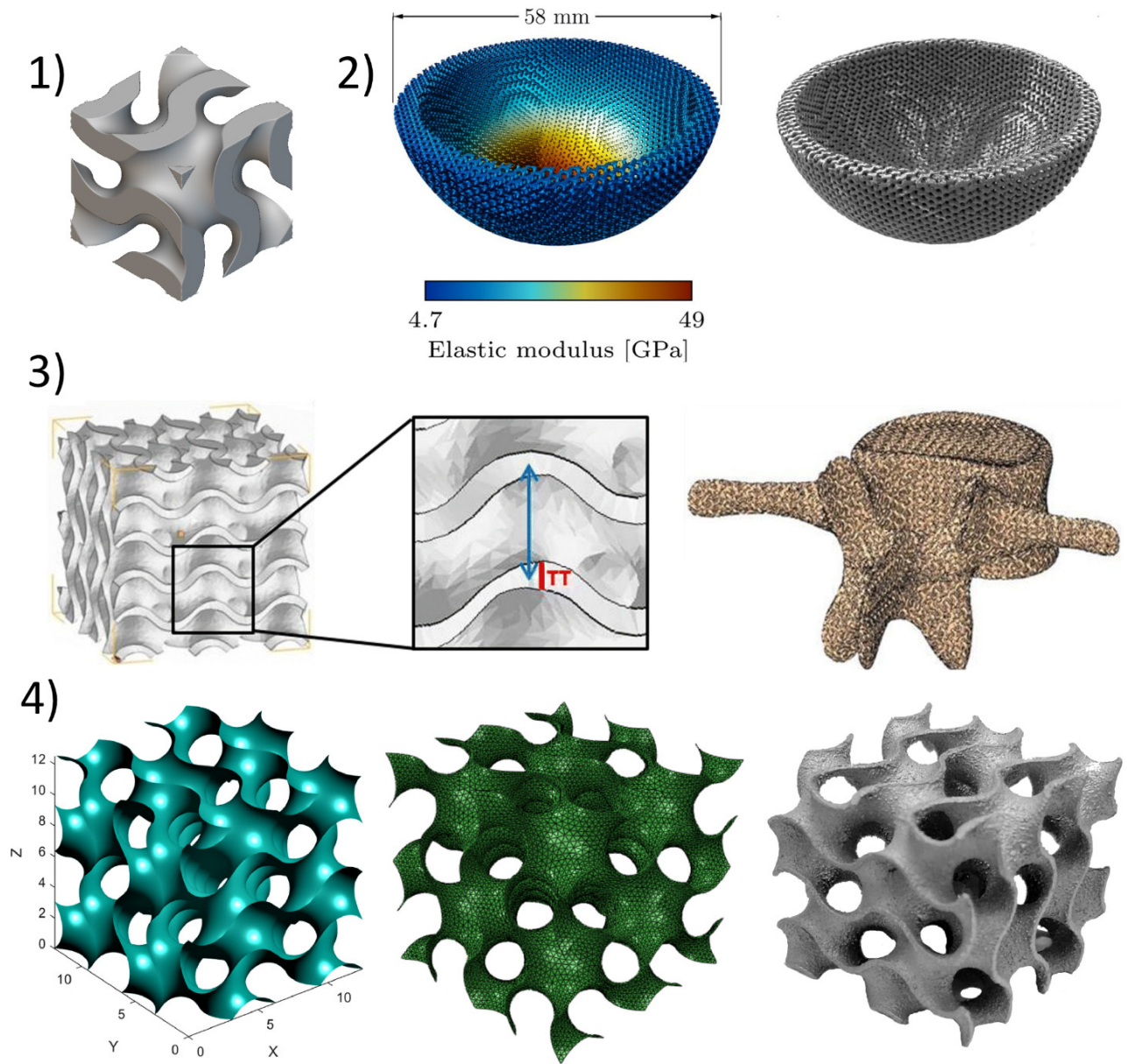
Figure 9) Gyroid lattices; 1) Gyroid cell. 2) The shell of an acetabular implant was assigned a skeletal-gyroid infill of varying volume fraction to match a desired stiffness distribution [84]. 3) Gyroid structure for simulation of cancellous bone. TS, trabecular spacing; TT, trabecular thickness and intersection between gyroid block and inner part of the vertebra [85]. 4) Gyroid iso-surface, FE mesh, and manufactured sample [86].
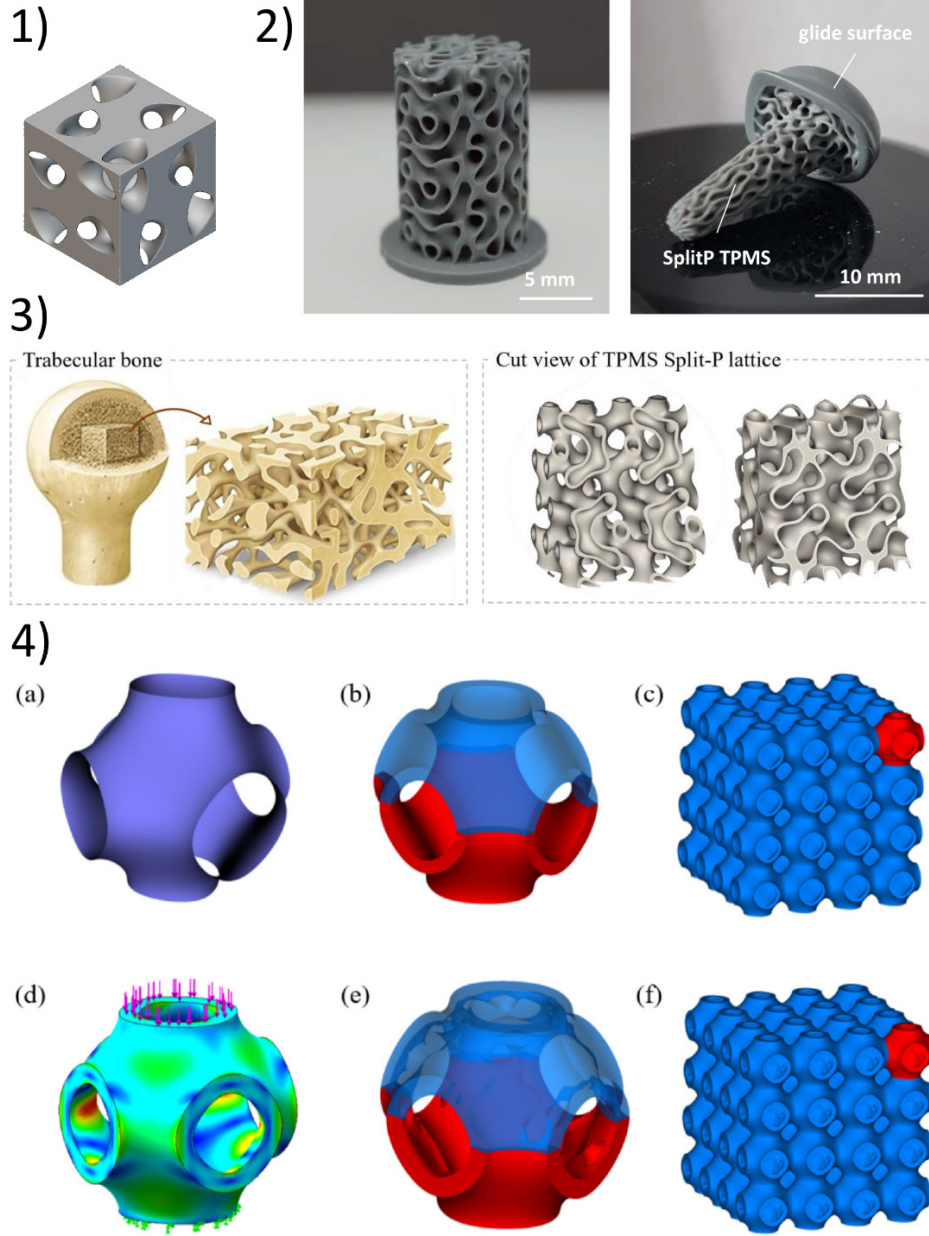
Figure 10) The Split-P cell presented in (1); 2) A cylindrical TPMS (SplitP design) component on base-plate and example of on finger implant with inner dense core, outer porous SplitP structure, and a polished glide surface [90]. 3) Schematic representation of the porous cellular structure of trabecular bone and sectional view of TPMS Split-P lattice resembling the morphology of trabecular bone [91]. 4) Design of the optimized P-TPMS scaffolds. (a) Schwarz Primitive surface; (b) P-TPMS unit cell; (c) P-TPMS scaffolds with uniform sheet thickness; (d) optimized process; (e) optimized P-TPMS unit cell; (f) P-TPMS scaffolds with optimized thickness [91].

The Diamond (D) TPMS, also known as the Schwarz Diamond (D), is characterized by a complex, interconnected pore network that resembles the atomic structure of a diamond lattice [78]. Its implicit mathematical representation is $sin(x)sin(y)sin(z) + sin(x)cos(y)cos(z) + cos(x)sin(y)cos(z) + cos(x)cos(y)sin(z) = C$. The Diamond structure is known for its high degree of interconnectedness and its ability to provide

excellent mechanical properties, often exhibiting a balance between stiffness and energy absorption. Like the Gyroid, it possesses a continuous, smooth surface, which contributes to reduced stress concentrations and good fatigue performance [92]. Its unique pore structure makes it especially useful in applications needing complex fluid pathways, such as filtration and reaction engineering. It is generally considered self-supporting for AM, although its complexity can sometimes demand more precise printing parameters [93]. The high porosity and interconnected nature of diamond lattices make them ideal scaffold materials in biomedical applications, as they promote cell infiltration and nutrient exchange, much like cancellous bone. They are also explored for structural applications where high specific strength and energy absorption are desired, and in catalytic converters or filters due to their intricate internal surface area [94].

The I-WP (Isolated Plate Woven) TPMS is a more complex minimal surface, recognized for its unique interwoven and isolated plate-like architecture. It is mathematically defined by an implicit function involving combinations of trigonometric terms, similar to other TPMS, creating a visually distinct and functionally intriguing structure. The I-WP surface has a unique woven look, created by a network of interconnected plates and channels. In contrast to Gyroid or Primitive structures, which typically produce single, continuous channels, I-WP structures usually form more isolated, but interconnected, pore networks [95]. This can lead to different flow dynamics and mechanical responses. Its high surface area-to-volume ratio and robust structure are well-known. The complex geometry enables unique tailoring of mechanical properties and fluid transport, frequently showing properties unlike those of other TPMS structures. While still largely self-supporting in AM, its intricate features might require careful consideration of building parameters. I-WP structures are being investigated for advanced heat exchangers, filters, and biomedical scaffolds where specific pore geometries and surface area characteristics are desired [96]. This unique internal structure offers advantages in damping applications and allows for lightweight components with customized anisotropic properties.

The Neovius TPMS, often considered a member of the Gyroid family due to its similar topological features, is another highly interconnected minimal surface. Its implicit mathematical equation is defined by a cubic surface form: *3(cos(x) + cos(y) + cos(z)) + 4cos(x)cos(y)cos(z) = C*. Compared to the Gyroid structure, the Neovius surface presents a network of interconnected channels with improved openness and reduced tortuosity, while preserving a continuous, smooth topology. It contains a single, maze-like channel that extends throughout space, much like the Gyroid, which makes it highly suitable for applications involving fluid flow. The structure is characterized by its relatively large open areas and less complex curvature compared to some other TPMS, which can potentially aid in manufacturability and post-processing, especially for larger pore sizes [97]. Its mechanical properties generally demonstrate good isotropy, thus ensuring resilience against multi-axial loading. The investigation of Neovius structures primarily focuses on applications demanding high flow rates, including fluid mixers, catalytic supports, and heat exchangers, where open porosity is essential for optimal performance. Its smooth internal surfaces and interconnectedness also make it suitable for biomedical scaffolds where larger pore sizes for cell infiltration and vascularization are beneficial [98].

The Fischer-Koch S (FKS) TPMS is a more complex and aesthetically intricate minimal surface. It is often described by a higher-order implicit equation, resulting in a unique geometry with multiple interconnected channels and distinctive curvatures. FKS surfaces produce intricate channel networks containing distinct regions. Its design offers a unique balance of porosity and structural integrity, often leading to specific anisotropic mechanical responses depending on the direction of load application. The complex architecture of the FKS structure results in a high surface area, making it particularly beneficial for applications that demand extensive interfacial contact or numerous reaction sites. Precise AM control is crucial for this complex structure's fabrication; post-processing may be harder than for simpler TPMS structures [99]. FKS structures are being investigated for advanced catalytic converters, high-surface-area filters, and specialized biomedical implants where a highly complex and interconnected pore network is desired for optimized biological integration or unique fluid transport properties. Its potential for tailored anisotropy also opens doors for specific load-bearing components [100].

Stochastic Voronoi structures represent a unique class of lattice structures that leverage stochastic tessellations to create irregular, interconnected cellular networks. A Voronoi tessellation divides space into regions based on the distance to a set of discrete "seed" points; when these seed points are randomly distributed, a stochastic Voronoi structure is generated [101]. Unlike periodic lattices, stochastic Voronoi structures consist of irregularly shaped, randomly sized cells that fill space. This inherent randomness mimics the micro-architecture of many natural materials, such as cancellous bone [102]. The irregular nature of the cells and their interconnectedness lead to highly isotropic mechanical properties, often superior to those of periodic lattices under complex loading conditions, as stress is distributed more broadly across the heterogeneous network. These structures also exhibit excellent energy absorption capabilities and a high degree of biocompatibility due to their natural-like porosity and high surface area, making them particularly suitable for bio-integration [103]. Their random nature means they are more tolerant of minor manufacturing flaws than perfectly regular designs. Stochastic Voronoi structures are extensively used in biomedical applications for bone scaffolds, orthopedic implants, and tissue engineering, where their biomimetic properties promote cell attachment and nutrient flow. They are also explored for energy absorption, sound absorption, and filtration systems where irregular porosity is advantageous. Their ability to replicate natural structures makes them valuable for custom prosthetics and other personalized medical devices [103].

1.5 Functionally Graded Materials and Functionally Graded Lattice Structures

Functionally Graded Materials (FGMs) are high-performance materials whose composition, microstructure, or properties change gradually or abruptly across their volume. The spatial variability is carefully engineered to fulfill particular performance criteria, including stress reduction at interfaces, better thermal management, enhanced durability, and customized mechanical responses [109]. Traditional manufacturing methods struggle to produce true FGMs with precise control over the gradient, often leading to

distinct layers or interfaces. However, additive manufacturing processes, with their inherent layer-by-layer deposition capabilities, are uniquely positioned to fabricate complex FGMs with unprecedented control over spatial variations in material properties and structural architecture [110].
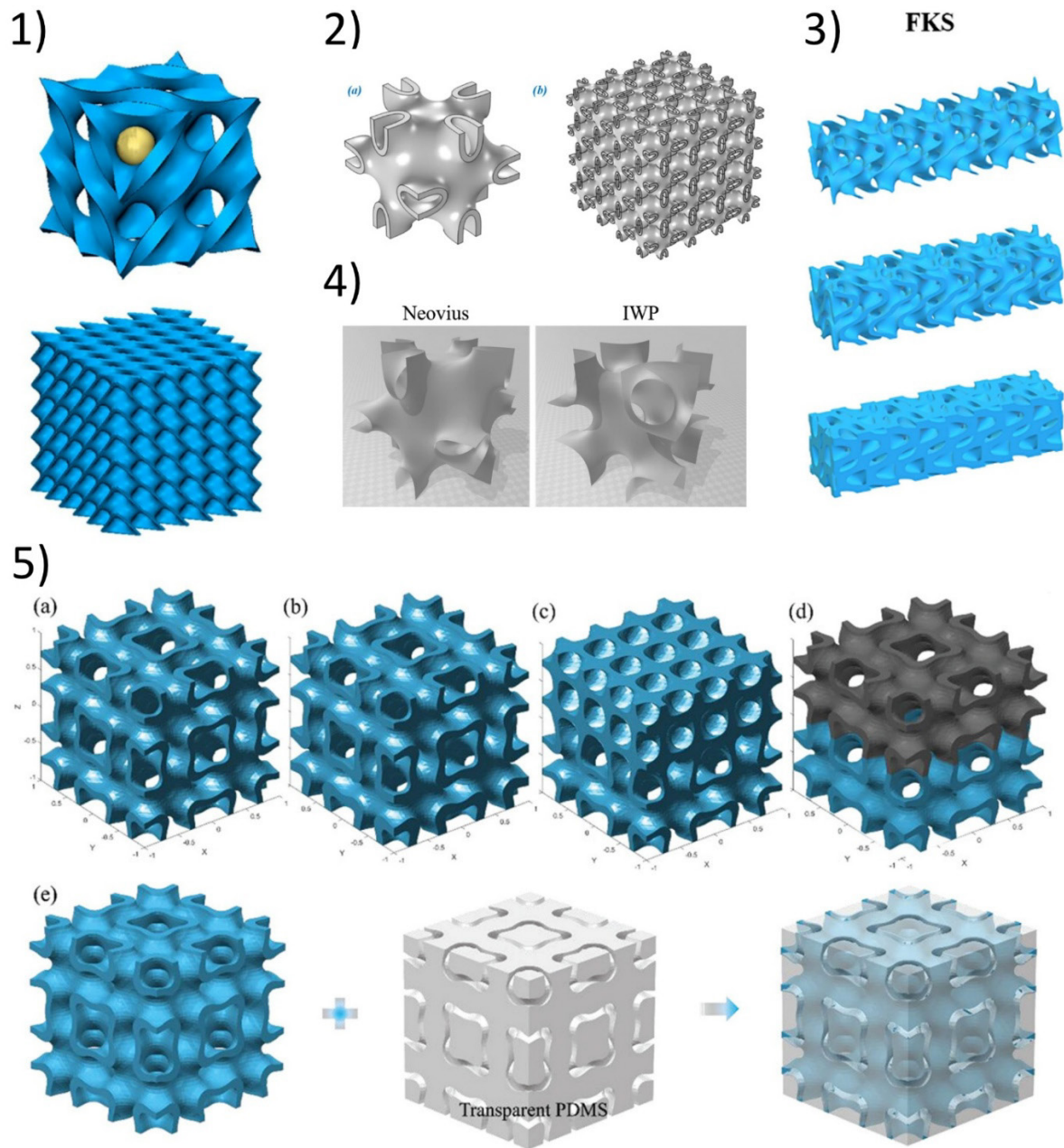
Figure 11) Illustration of the tpms structures; 1) The diamond lattice where pore sizes are marked by yellow [104]. 2) CAD drawing of the Neovius-lattice: (a) one unit cell, (b) three-dimensionally periodic 64 (4×4×4) cells [105]. 3) FKS models with different volume fractions [106]. 4) Comparison between Neovius and IWP [107]. 5) Design of TPMS lattice structures. (a) Uniform IWP structure as control sample. (b) IWP structure with density gradient. (c) Hybrid configurations of IWP and Diamond cell. (d) IWP structure with hybrid materials of PLA and carbon fiber reinforced PLA. (e) IWP structure with filled polydimethylsiloxane (PDMS) [108].

The application of FGM principles within additive manufacturing can manifest in various ways, including compositional grading (varying the ratio of different materials), microstructural grading (controlling grain size or phase distribution), or as is particularly relevant here, physical grading of lattice structures, so called Functionally Graded Lattice Structures (FGLS). This FGLS involves systematically changing the geometric parameters of the lattice unit cells across a component to achieve a continuous or stepped gradient in mechanical properties, without changing the base material composition. Local lattice density, stiffness, and strength are instead tuned by varying parameters like strut diameter, wall thickness, cell size, or unit cell type, depending on location within the structure [111].

Consider a component where a specific region requires higher stiffness and strength, while another needs greater flexibility or energy absorption. Through physical grading, the lattice within the high-stress region can be designed with thicker struts or a smaller unit cell size, leading to a higher relative density and thus increased local mechanical properties. Conversely, in regions where weight reduction or compliance is prioritized, thinner struts or larger unit cells can be employed to create a lower relative density [112]. This continuous variation in lattice geometry eliminates abrupt changes in material properties, which are common sources of stress concentrations and premature failure in traditionally joined or multi-material components. The resulting component is a single, monolithic part with spatially optimized properties tailored to specific loading conditions or functional requirements.

The primary mechanism for achieving functional grading in lattice structures, as emphasized, is the physical modification of the lattice geometry, specifically by varying the thickness of the lattice elements (struts or surface walls) or the overall cell size. For instance, a component designed to dissipate impact energy might feature a lattice with a denser, stiffer region at the impact point that gradually transitions to a less dense, more compliant region away from it [113]. This gradient in stiffness and energy absorption is achieved by incrementally reducing the strut diameter or increasing the cell size, rather than by changing the material type itself. This approach ensures continuity of the material and avoids interface issues, while still allowing for a wide range of localized property tailoring [114]. Beyond mechanical advantages, FGLS support enhanced thermal and biological performance in multifunctional components. Varying lattice density and connectivity allows designers to control local thermal conductivity, enabling integrated cooling solutions or heat dissipation systems tailored to specific application needs [115]. In biomedical implants, spatially graded porosity—achieved by adjusting lattice cell size or strut thickness—optimizes both initial mechanical support and long-term biological integration, improving osseointegration while reducing stress shielding. Moreover, by enabling precise material placement, FGLS promote material efficiency, significantly cutting down on waste, production costs, and environmental impact [116].

Designing physically graded lattice structures requires sophisticated computational tools, including explicit grading functions or optimization algorithms, to define the variation of lattice parameters within the desired volume. These tools allow designers to specify how the strut thickness, cell size, or relative density should

change along specific directions or based on local stress analysis [117]. The ability of AM to precisely deposit material layer by layer makes the fabrication of such intricate, graded geometries entirely feasible, opening new frontiers in material and structural engineering.

2 states of art

Laser powder bed fusion of the aluminum alloy AlSi10Mg enables fabrication of complex lattice metamaterials with tailored mechanical properties. Gyroid, split-P, and stochastic Voronoi lattices are of particular interest for lightweight, high-performance structures. Gyroid is a triply periodic minimal surface noted for isotropic stiffness and large surface area. The split-P surface is a related TPMS variant recently applied in metal lattices, while Voronoi lattices mimic stochastic, trabecular architectures. Functionally graded versions of these lattices – e.g. with variable strut or wall thickness – allow smooth density variation and improved performance in targeted regions. Many recent studies have explored LPBF AlSi10Mg lattices for compression and tensile behavior. In the following, key works are summarized by the author and year, describing what was done and their findings. For example: *"Noronha et al. (2024) investigated AlSi10Mg hollow-strut lattices fabricated by LPBF, and found that their relative yield strength reaches the Gibson–Ashby upper limit [118]."* Each study's context and results are highlighted.

2.1 Gyroid Lattice Studies

Barrios et al. (2022) conducted a systematic comparison of six AlSi10Mg lattice types (including gyroid and Voronoi) under quasi-static compression [119]. They reported that TPMS lattices (especially diamond and gyroid) had the best energy-absorption performance, while stochastic Voronoi and auxetic lattices had much lower specific energy absorption (SEA) for a given peak stress. In particular, gyroid lattices achieved high specific energy absorption and desirable plateau behavior. Their results imply that among diverse designs, gyroid and similar TPMS structures are superior for energy-absorbing applications, whereas Voronoi offers tunability but lower efficiency.

Maskery et al. (2016) and Chen et al. (2023) investigated the effect of density grading on gyroid structures. Maskery et al. found that LPBF-printed AlSi10Mg gyroid and other lattices had similar energy absorption before densification, and that heat treatment improved overall absorption [120]. Chen et al. showed that the effective stiffness of graded TPMS structures could be predicted by composite theory [121]. These studies indicate that graded gyroid lattices can be tuned via cell wall thickness without sacrificing initial energy absorption.

Sun et al. (2024) compared gradient gyroid ("Gradient-Gyroid") with other graded cell types under compression [122]. They found the gradient split-P design outperformed gradient gyroid in compressive strength and energy absorption, but gradient gyroid still provided strong performance.

2.2 Split-P Lattice Studies

The split-P lattice is a newer TPMS-like geometry (related to the classical P surface) adapted for AM. Sun et al. (2024) explicitly analyzed AlSi10Mg split-P lattices. They created Gradient-SplitP structures (with continuous density gradient) and compared them to other graded lattices [122]. The gradient split-P design showed superior compressive performance versus graded gyroid and lidinoid. At similar apparent density (~0.796), the gradient split-P achieved the highest specific strength and energy absorption (SEA ≈ 23.57 MJ/m³).

Sun et al. note that split-P's architecture yields a more favorable stress distribution under load, explaining its outperformance. They attribute high efficiency to optimized strut layouts in split-P geometry. This suggests that split-P lattices are at least as promising as gyroids for high-strength, graded designs. Though few AlSi10Mg works exist on Split-P, related studies in Ti6Al4V show Split-P's bone-scaffold potential. For example, Liu et al. (2021) designed split-P scaffolds that approached bone stiffness.

2.3 Stochastic Voronoi Lattice Studies

Barrios et al. (2022) included a Voronoi lattice in their experimental comparison [119]. They found that the Voronoi lattice had low specific energy absorption and low densification efficiency, although it was highly tunable. In their hierarchy, Voronoi's performance was at the lower end, significantly worse than gyroid. The authors explain that the irregular strut connectivity in Voronoi yields early failure and uneven stress distribution under compression.

Deng et al. (2024) designed porous UKA (unicompartmental knee) tibial implants with Voronoi lattices (seed spacing ~2 mm, strut ~280 μm) at 70–90% porosity. Quasi-static compression of sample lattices showed stretch-dominated behavior. Under gait loading FE simulations, the Voronoi implant yielded ~44–80% higher mean stress in the medial tibial plateau vs conventional solid UKA, closely matching native bone stress [123]. Developed by Colamartino et al. (2023) empirical models relating parent material properties to 3D Voronoi foam compressive behavior. Their analysis showed Voronoi lattices have higher mechanical efficiency (strength-to-weight) than natural open-cell foams [124].

Cheloni et al. (2025), although using Ti, their study is informative. Testing functionally-graded BCC, gyroid, diamond, Voronoi, they found TPMS lattices (gyroid/diamond) exhibited more uniform stress fields, whereas BCC/Voronoi had stress concentrators [125]. Diamond had the highest ultimate strength (~430 MPa), with gyroid second (~396 MPa). Voronoi lattices, despite lower peak strength, distribute stress more evenly, which can be beneficial for implants to avoid local failure.

2.4 Applications in Biomedical

A significant frontier in biomedical engineering is the development of implants that can integrate seamlessly with host tissues, particularly at the interface between soft and hard tissues (e.g., tendon-to-bone or cartilage-to-bone) [126]. These biological junctions are themselves functionally graded, exhibiting a natural, continuous transition in composition, structure, and mechanical properties. Replicating this gradient is essential for restoring function and preventing implant failure.

FGLS are ideally suited to address this challenge. By designing a lattice with a stiffness gradient that matches the transition from soft tissue (low modulus) to hard bone (high modulus), it is possible to create an "integration zone" that promotes tissue regeneration and ensures stable mechanical fixation. Mahmoud and Elbestawi (2017) reviewed the application of FGLS in orthopedic implants and concluded that they are a superior solution for mitigating stress shielding, a major cause of aseptic loosening in hip and knee implants [126].

Recent research has focused specifically on this interface. Toosi et al. (2024) highlighted that additively manufactured porous scaffolds designed with gradients in pore size and stiffness can effectively guide the regeneration of different tissue types, such as cartilage and subchondral bone in osteochondral defects [127]. A study by Wang et al. (2022) utilized a biomimetic design strategy for Ti-6Al-4V scaffolds, showing that graded porosity not only enhanced osseointegration but also promoted a more uniform stress distribution at the bone-implant interface [128]. The use of TPMS and stochastic Voronoi topologies within these FGLS is particularly promising. The continuous surfaces of TPMS structures provide an excellent substrate for cell attachment, while the biomimetic nature of stochastic lattices can more closely replicate the complex architecture of the natural tissue transition zone [129]. One aim of this thesis is to compare these advanced topologies in an FGLS framework to assess their suitability for this demanding application.

2.5 Conclusion and Research Gaps

Recent studies (2016–2025) demonstrate the potential of LPBF AlSi10Mg lattices (gyroid, split-P, Voronoi) for lightweight structural and biomedical applications. Gyroid and split-P (TPMS) lattices, especially in graded form, achieve high compressive strength and energy absorption. Voronoi lattices offer robust performance with excellent stress distribution and tunable porosity. AlSi10Mg as the base material is justified by its low density, corrosion resistance, and amenability to heat treatment[130]. These material-geometry combinations are promising for orthopedic implants because they better match bone stiffness than dense metals, thus reducing stress shielding. The ability to create custom implant scaffolds that match patient anatomy precisely will be possible through advanced high-resolution LPBF fabrication and precise cell gradient control. A review of the literature reveals graded gyroid, split-P, and Voronoi AlSi10Mg lattices as promising candidates for load-bearing implants due to their optimal combination of strength, weight reduction, and biocompatibility.

The literature clearly establishes that additively manufactured lattice structures, particularly TPMS and stochastic Voronoi topologies, offer significant advantages for creating high-performance, lightweight components. The field is progressively moving from uniform lattices to functionally graded designs (FGLS) to meet the demands of advanced applications, especially in the biomedical sector. The challenge of creating stable and functional soft-hard tissue interfaces remains a major research focus, with FGLS emerging as the most promising solution.

However, a direct and systematic comparison of the mechanical performance of different advanced lattice topologies (Gyroid, Split-P, and Stochastic Voronoi) within a functionally graded framework is still lacking. While many studies focus on a single topology, there is a clear gap in understanding the relative advantages and disadvantages of each when designed with identical property gradients and fabricated under the same conditions.

This thesis aims to address this gap by:

1. Designing, fabricating, and mechanically testing FGLS based on Gyroid, Split-P, and stochastic Voronoi topologies with controlled, graded thickness parameters.
2. Conducting a comparative analysis of their compressive and tensile properties, failure mechanisms, and energy absorption capabilities and while doing the fractography to interpret the failure.
3. Utilizing CT scan data to verify the as-built geometries and inform the analysis of their mechanical behavior.

By undertaking this comprehensive comparison, this research will provide valuable insights for engineers and designers, helping to establish clear guidelines on which lattice architecture is best suited for specific loading conditions and, ultimately, for the demanding application of biomimetic soft-hard tissue implants.

3 Materials and Method

The FGLS design phase includes developing the lattice structure, choosing the appropriate lattice topology, identifying the unit cell types, and defining the lattice parameters to achieve the intended boundary conditions [131]. The selection of unit cell geometry represents a critical aspect of the lattice design process. Many CAD software platforms offer extensive libraries of unit cell configurations, which are commonly used in the design of lightweight, additively manufactured components. Effective additive manufacturing of the part, fulfilling its intended function, necessitates careful consideration of geometry, material selection, and manufacturing process [132]. In this study, nTopology software [133], was employed to design and generate various architected lattice structures, including gyroid, split-P, and stochastic geometries, enabling tailored spatial gradation and complex geometry control. Emphasis is placed on the computational design and modeling in nTopology, including the geometric configurations, lattice types, and parameter definitions. The designed specimens were then fabricated by laser powder bed fusion on a TruePrint 1000 machine using AlSi10Mg powder as the feedstock material. Following fabrication, quality assessment of the samples was performed via X-ray computed tomography scanning. Mechanical characterization was carried out through uniaxial tensile and compression tests to determine the key mechanical properties, and fracture surface analysis was conducted by scanning electron microscopy (SEM) to explain the underlying failure mechanisms.

3.1 Lattice Structure Design and Modelling

Dog-bone-shaped tensile specimens and Cubic-shaped compression specimens were designed with lattice architecture in their gauge sections. The tensile samples followed a standard dog-bone geometry with a reduced cross-section (gauge) in the center; the gauge region incorporated a lattice structure and featured slight thickness variation along its length to transition smoothly into the solid gripping ends (ensuring failure occurs in the lattice region) as shown in Figure 12-a1. The compression, Figure 12-a2, samples were designed as 30 x 15 x 15 mm^3 cubes in which 20 mm of the height is lattice (the gauge section) sandwiched between solid tips of 5 mm thickness at the top and bottom. These solid end caps facilitate uniform load introduction during compression. Figure 12-b1 shows a schematic of the tensile specimen with a lattice-filled gauge, and Figure 12-b2 shows the compression specimen with a lattice core and solid end plates. To minimize stress concentrations in both tensile and compression samples, rounded transitions connected the lattice to the solid parts as illustrated in Figure 12-c.
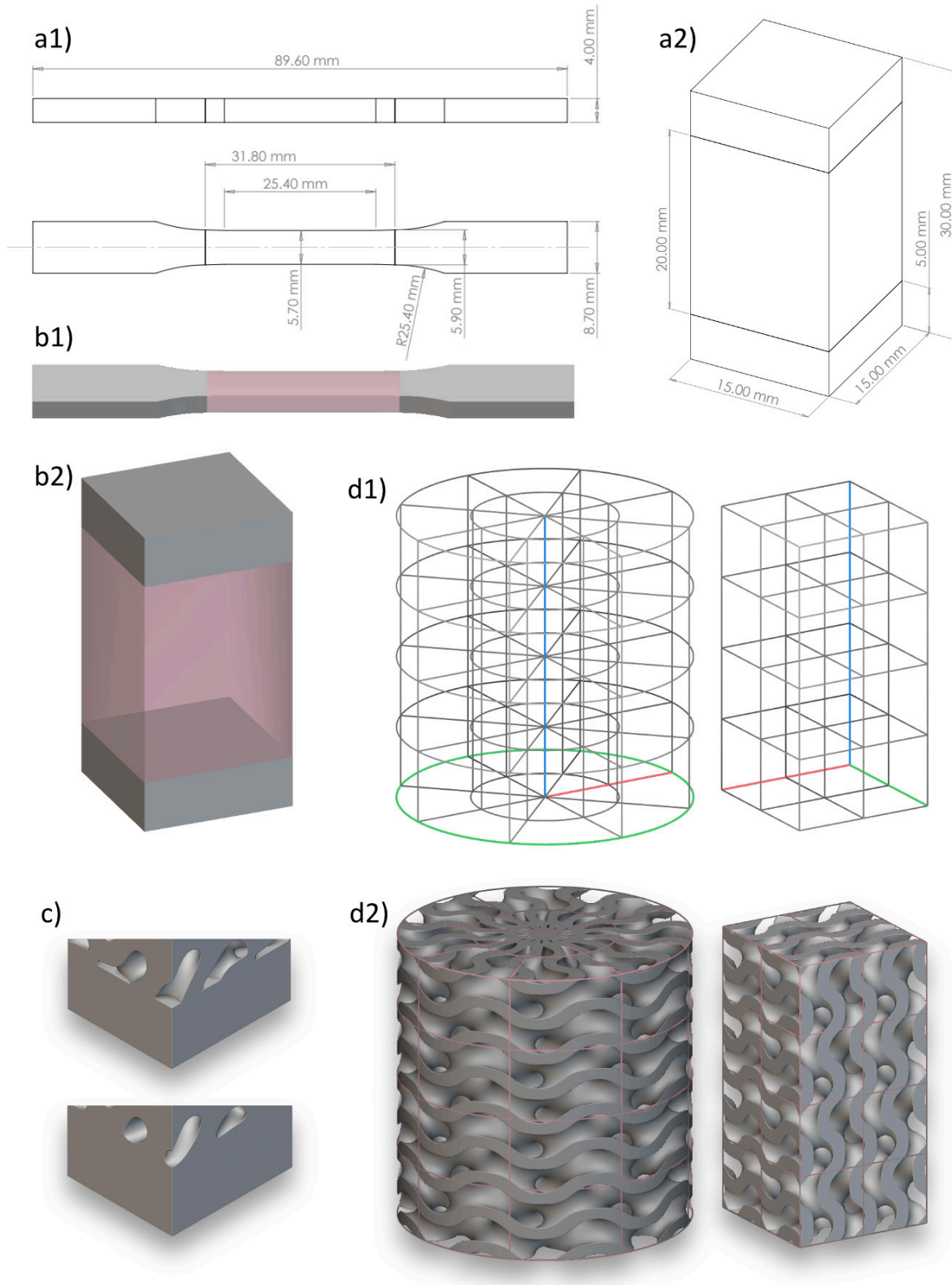
Figure 12) Design phase cubic samples for compression test and the dog-bone shape for tensile test: a1, a2) The layout of the specimens. b) Corresponding solid models (grey) and lattice part (red) showing the transition regions between the solid and the lattice–void zone for (b1) tensile and (b2) compression specimens. c) Rounded transitions smoothly joined the lattice to the solid components. d) Lattice generation workflow for both cubic and cylindrical cell maps.

Three lattice topologies were implemented: (1) Gyroid TPMS, (2) Split-P TPMS, and (3) a stochastic Voronoi-based lattice. The design process began by specifying a unit cell for each topology and then applying an appropriate cell map to fill the intended specimen volume. The lattice is built from repeating units called unit cells. Each lattice topology—like the Gyroid, Split-P—has a unique unit cell geometry that defines its structural and mechanical properties [134]. A cell map refers to the arrangement and distribution of unit cells within a lattice structure. It defines how unit cells are organized and connected to fill the entire volume of the structure [135]. Designing lattice structures requires careful consideration of both unit cell and cell map parameters. The size of the unit cell determines the repeating pattern, completely filling the volume specified by the cell map. Besides, the type of unit cell—whether cylindrical or cubic—has a significant impact on the resultant structure's geometry and mechanical properties [136].

Considering Gyroid and Split-P lattice structures, for the dog-bone shaped tensile specimens, only the cubic cell map was used, with unit cell dimensions of 3 mm × 3 mm × 3 mm. While for the compression test specimens, two types of cell mapping strategies were applied: cubic and cylindrical (Figure 12-d1 and d2). The cubic cell map used unit cells with dimensions of 7.5 mm × 7.5 mm × 7.5 mm; and for the cylindrical cell map, the design was defined by three parameters: a cell radius of 7.5 mm, a cell height of 7.5 mm, and an arc count (angular divisions) of 8. Regarding the stochastic Voronoi-based lattice structures, first the seed points were randomly distributed within the designated gauge region, with a specific point spacing for both dog-bone shaped tensile specimens and cubic compression test specimens. Then, by defining a strut thickness, the Voronoi diagram was converted into a solid lattice structure. In nTopology, after mapping, a Trim operation was used so that any protruding cells were cut flush with the specimen surface, yielding a lattice that exactly fills the intended gauge volume.

The thickness of the lattice structures followed a scalar field (Figure 13), with the minimum thickness defined at the center of the gauge and gradually increasing toward the maximum at the ends. The way lattice thickness was determined for different lattice types was a critical aspect of the model. In nTopology, two methods were used to define the wall thickness of TPMS unit cells: the Offset method and the Exact Thickness method. The Offset method controls thickness by applying a positive or negative distance to the mid-surface of the TPMS geometry, effectively shifting the surface outward or inward. The computationally efficient method is well-suited for design exploration; it was used to design the Split-P lattice structure. Conversely, the Exact Thickness method enables users to define a target wall thickness, which the software refines to closely match the desired value; it was applied to the Gyroid and stochastic Voronoi-based lattice structure designs.

Regardless of the chosen method to apply the thickness, to ensure a fair comparison across different lattice structures, the minimum and maximum thickness values within the gauge section were adjusted so that each specimen contained the specific total volume of solid material. This strategy was used to isolate the effect of geometry alone on mechanical performance.
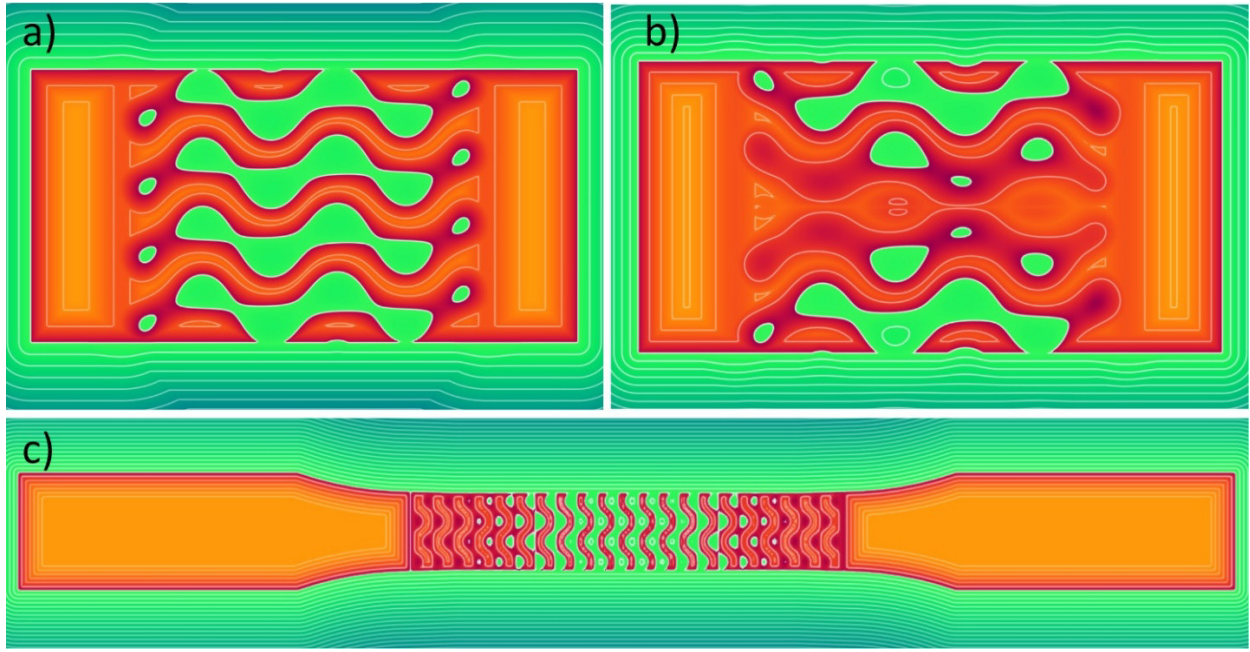
Figure 13) Contour plots illustrate the continuous thickness gradient, minimum at the center, smoothly increasing toward the solid end blocks. Gyroid structures in (a) and (c) use a cubic cell map, while (b) uses a cylindrical one.

For the cube-shaped compression specimens, three volume classes—A, B, and C—were defined, along with a bulk reference specimen without any lattice structure in the gauge region for comparative purposes. Class A, representing approximately 79% relative volume compared to the bulk specimen, included samples with various lattice configurations: Gyroid and Split-P topologies using both cubic and cylindrical cell maps, as well as a stochastic Voronoi-based lattice. Class B, with 72% relative volume (Gyroid cubic and cylindrical cell map, stochastic), and Class C, with 75% relative volume (Split-P cubic and cylindrical cell map, stochastic). All details concerning the compression sample designs are shown in the Figure 14.

For the tensile dog-bone specimens, four volume classes, A through D, were designed, along with a solid, lattice-free dog-bone serving as the 100% volume baseline. Class A (95% relative volume) comprised Gyroid (GY-TA, 0.7–2 mm), Split-P (SP-TA, 0–0.7 mm) and stochastic (ST-TA, 0.7–2 mm) samples. Class B (97% relative volume) included GY-TB (1–2 mm), SP-TB (0–1.1 mm) and ST-TB (1–2 mm) specimens. Class C (93% relative volume) contained GY-TC (0.7–1.5 mm), SP-TC (0–0.5 mm) and ST-TC (0.7–1.5 mm) samples. Class D (96% relative volume) encompassed GY-TD (1–1.5 mm), SP-TD (0–0.9 mm) and ST-TD (1–1.5 mm) specimens. All CAD renderings and details of lattice type, sample name, thickness/offset range, and relative volume are summarized in Figure 15.
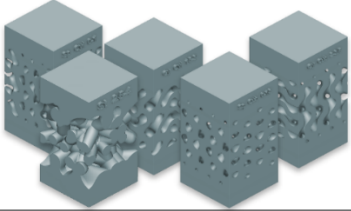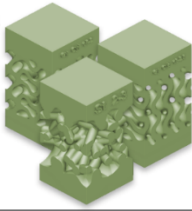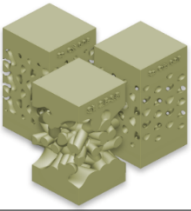
Compression Samples				
Lattice Type	Sample Name	Thickness or Offset [mm]	Volume [mm³]	Relative Volume
Gyroid (Cylindrical Cell)	GY-CYL-A	1.5 − 3	5322	79%
	GY-CYL-B	1.5 − 2	4867	72%
Gyroid (Cubic Cell)	GY-CU-A	2 − 3.5	5320	79%
	GY-CU-B	1.8 − 2.5	4860	72%
Split-P (Cylindrical Cell)	SP-CYL-A	0 − 1	5324	79%
	SP-CYL-C	0 − 0.5	5052	75%
Split-P (Cubic Cell)	SP-CU-A	0 − 1.3	5317	79%
	SP-CU-C	0 − 0.7	5040	75%
Stochastic	ST-A	2.5 − 4	5320	79%
	ST-B	2 − 3	4872	72%
	ST-C	2.5 − 3.5	5052	75%
Bulk	−	−	6750	100%

Figure 14) CAD models of cubic compression specimens (classes A–C, 79–72–75 % relative volume)
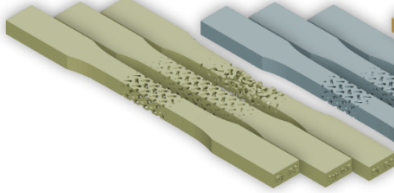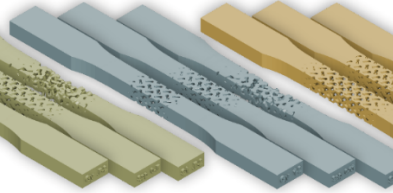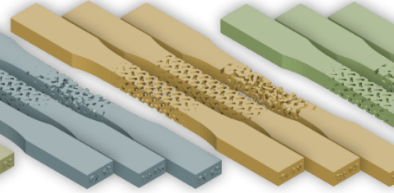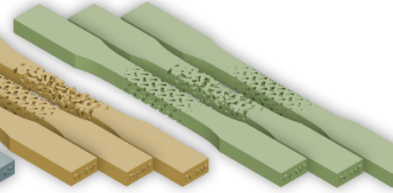
Tensile Samples				
Lattice Type	Sample Name	Thickness or Offset [mm]	Volume [mm³]	Relative Volume
Gyroid	GY-TA	0.7 − 2	2477	95%
	GY-TB	1 − 2	2539	97%
	GY-TC	0.7 − 1.5	2429	93%
	GY-TD	1 − 1.5	2500	96%
Split-P	SP-TA	0 − 0.7	2472	95%
	SP-TB	0 − 1.1	2531	97%
	SP-TC	0 − 0.5	2422	93%
	SP-TD	0 − 0.9	2508	96%
Stochastic	ST-TA	0.7 − 2	2471	95%
	ST-TB	1 − 2	2532	97%
	ST-TC	0.7 − 1.5	2424	93%
	ST-TD	1 − 1.5	2495	96%
Bulk	−	−	2615	100%

Figure 15) CAD models of tensile dog-bone specimens (classes A–D, 95–97–93–96 % relative volume). Tables list lattice type, sample name, thickness/offset and relative volume.

The area-length curves describe a U-shaped profile, with the smallest cross-sectional area at the specimen's midpoint (the thinnest section) rising toward the ends where the sections are thickest. The slope's steepness directly correlates with the thickness gradient; a steeper slope means a greater thickness difference between center and edges, indicating a more abrupt transition, while a gentler slope suggests a smoother, more gradual change. Meanwhile, the persistence of the characteristic oscillations, caused by the porous or lattice architecture, right out to the ends shows that the porosity or lattice structure extends fully to the grips; if those oscillations diminish before reaching the ends, it means the porous pattern was confined to the central region and beyond that the material reverts to solid.

In the cubic compression specimens (Figure 16), cross-sectional areas were extracted at each build height and plotted to show how the programmed thickness gradient interacted with cross-sectional area. Areas were largest at the solid ends, showing a smooth reduction towards the middle where the wall thickness was at its thinnest point. Inherent variations caused by the lattice equation pattern produced periodic oscillations superimposed upon the observed trend. In contrast, the stochastic Voronoi samples yielded irregular, non-periodic area curves, indicating that no coherent layer-wise trend could be defined for their random topology.
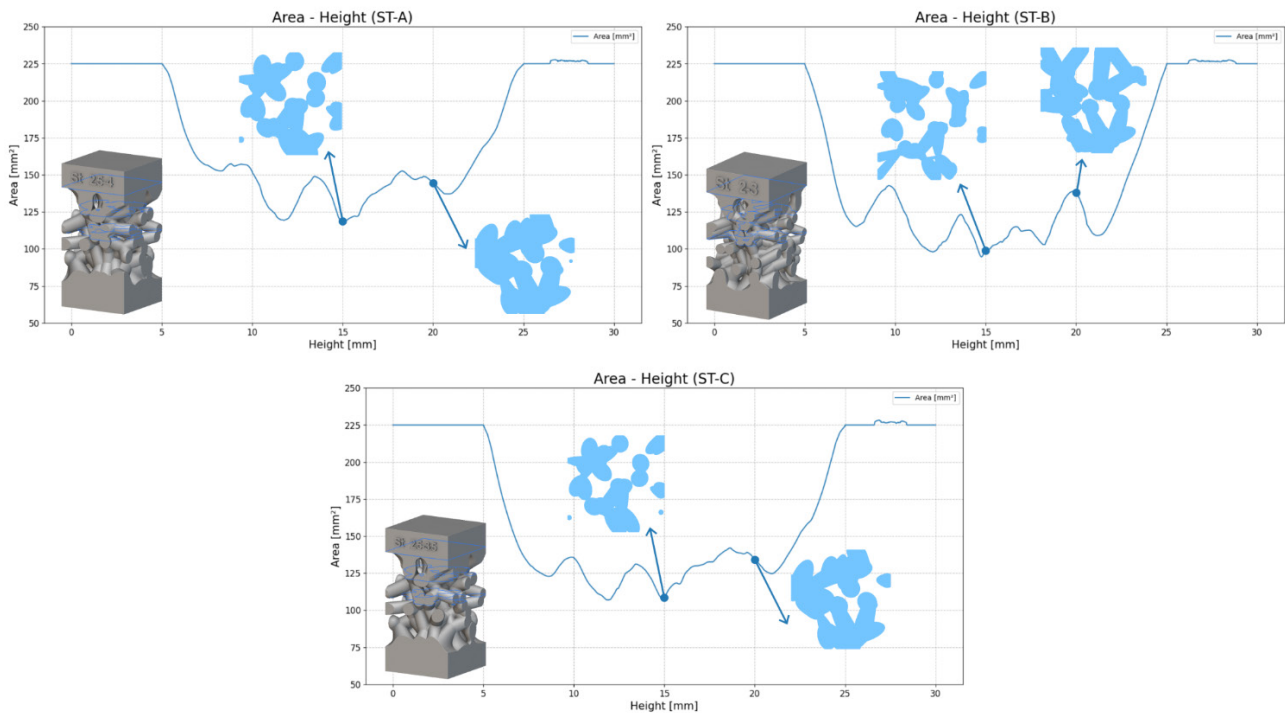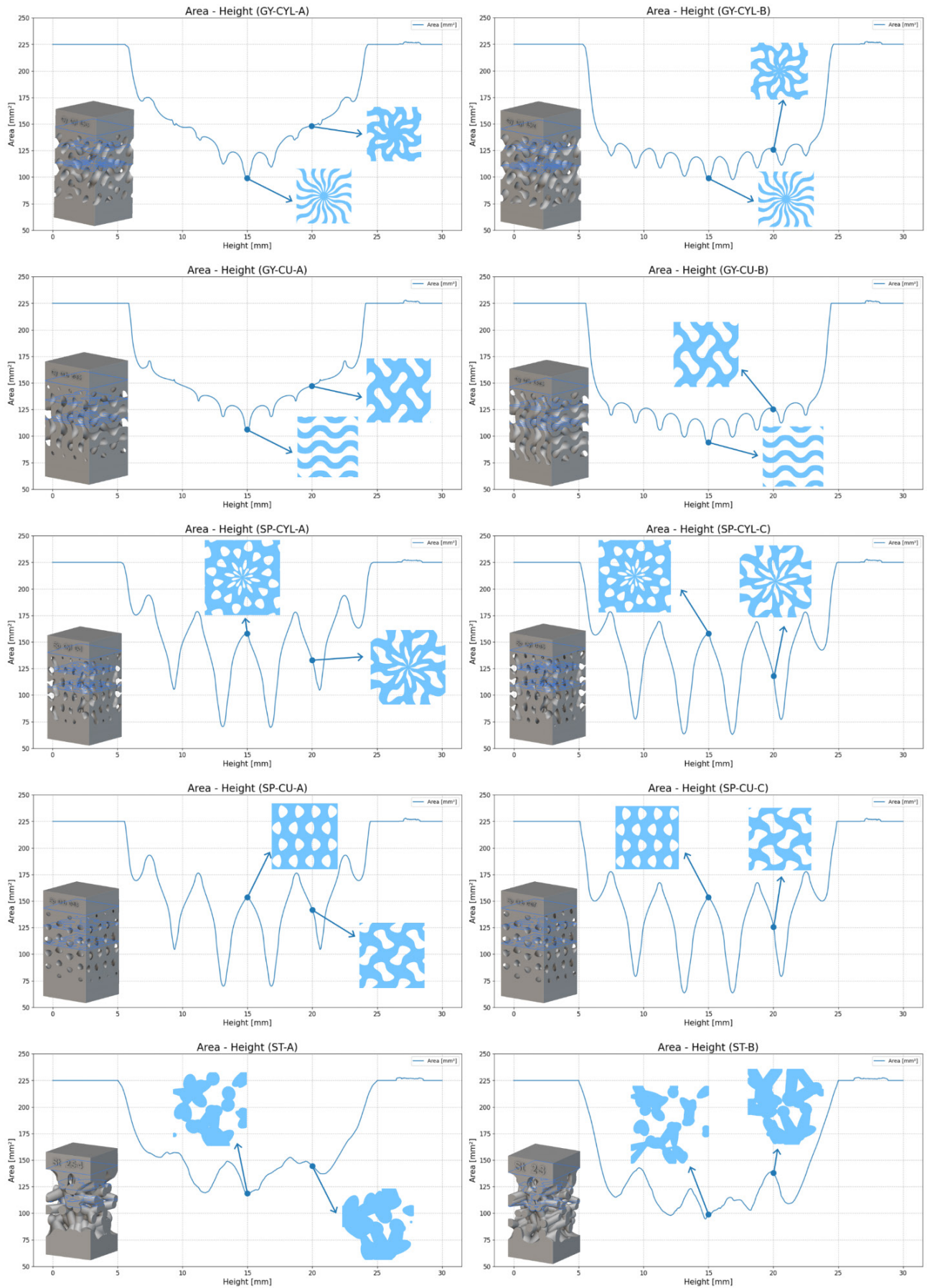
Figure 16) Cross-sectional area at each 0.1 mm slice through the lattice zone and plotted against build-height

In the tensile dog-bone specimens (Figure 17), a similar slice-by-slice area analysis was carried out along the gauge length. The area gradually decreased from the rounded grip sections to a minimum at the gauge center, then increased symmetrically to match the programmed thickness. As before, the stochastic dog-bone series (ST-TA, B, C, D) produced noisy, aperiodic area traces, confirming that no systematic trend was present in their layer-wise surface areas.
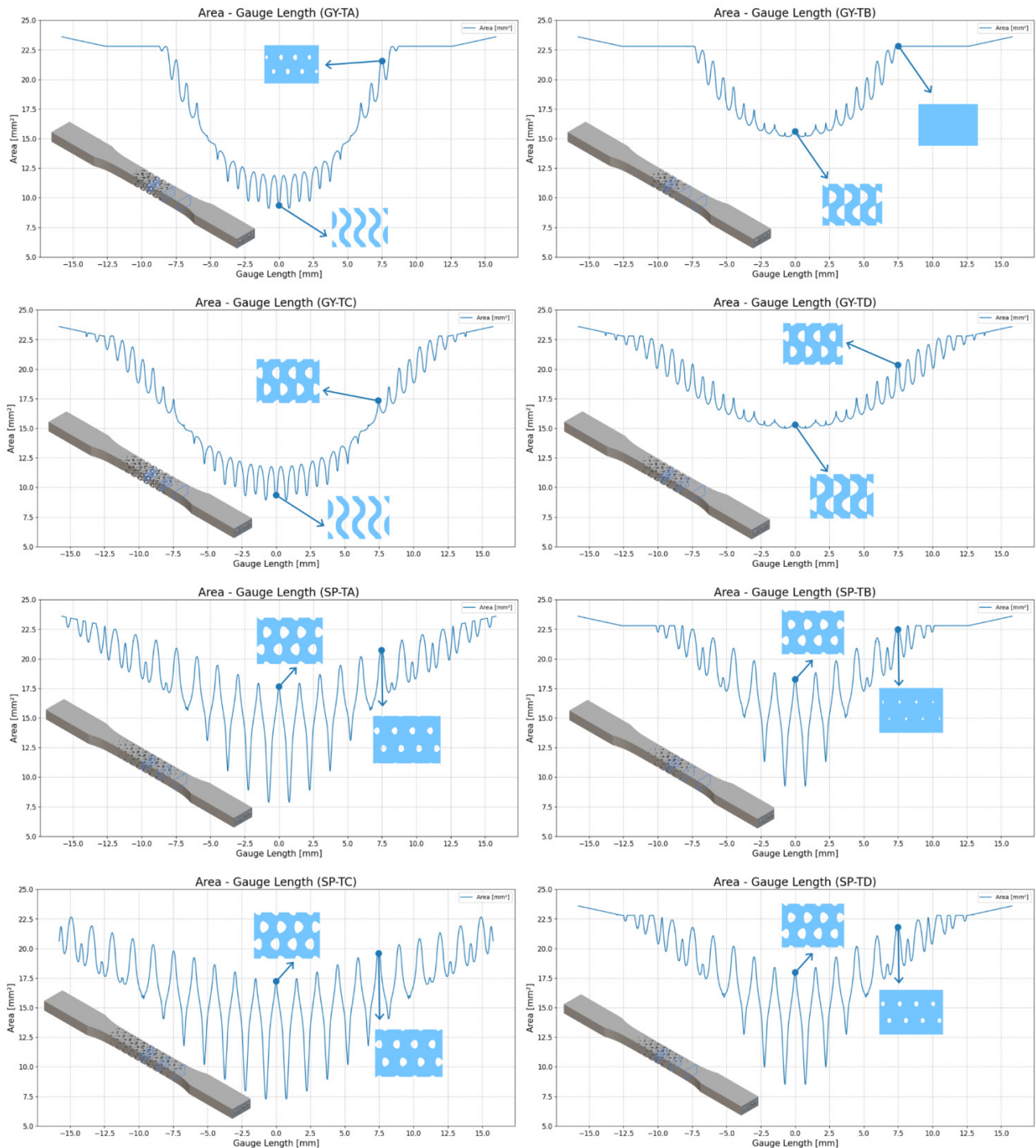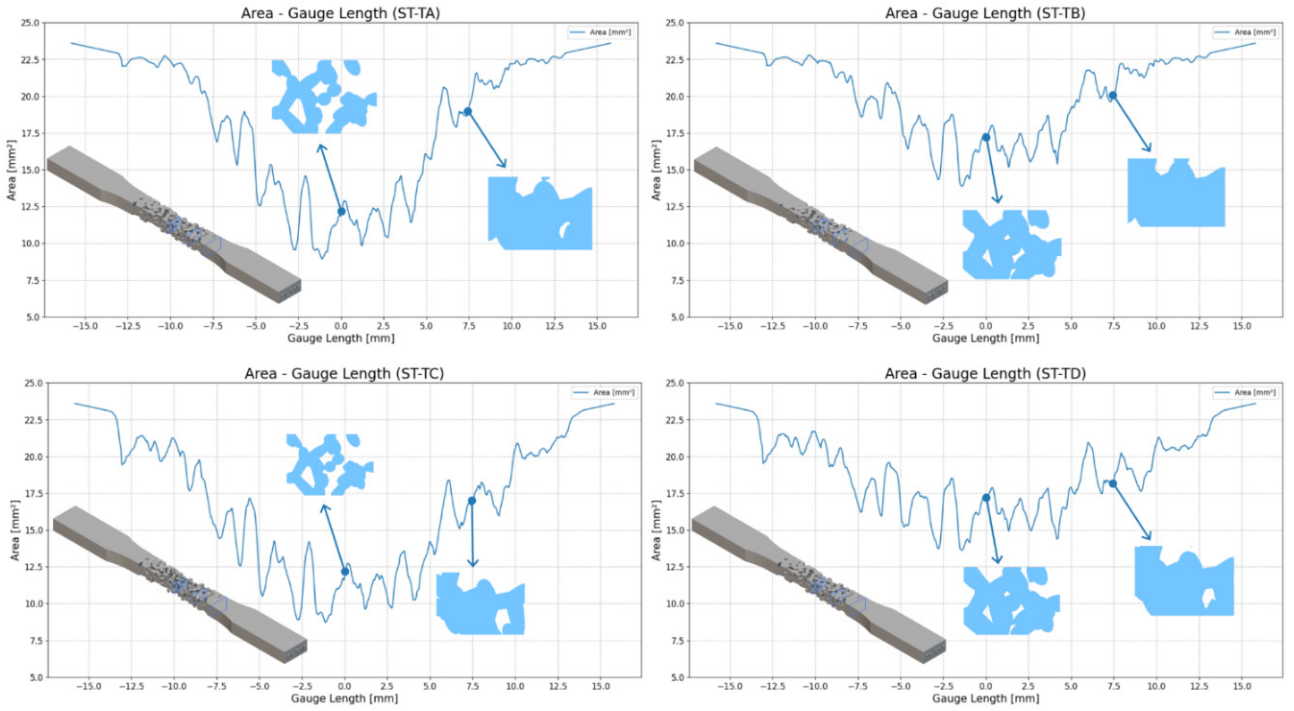
Figure 17) Slice-by-slice area calculation along the gauge length for each dog-bone sample

On each graph in Figure 16 and Figure 17, the overlaid cross-sectional sketches show that locations with smaller measured area correspond to regions of higher porosity. For every sample, two such cross-sections are presented: one at the exact midpoint and another at the halfway point between the midpoint and the specimen tip.

3.2 Production and Material

Samples, both tensile specimens and cubic compression blocks, were produced on a TruPrint 1000 powder-bed fusion system (TRUMPF GmbH & Co. KG, Germany [137]) using gas-atomized AlSi10Mg powder supplied by Electro Optical System (EOS) GmbH, Germany [138]. The Figure 18 shows the TruPrint 1000 machine and its specifications. Representative SEM images of the powder feedstock, obtained using a JEOL SEM machine, are shown in Figure 19; its chemical composition is listed in Table 2.

The process parameters used for the SLM process for both tensile and compression design are also presented in the Table 3. Using a rigid recoater blade, successive 30 µm layers of powder were spread within the build chamber, which had been flooded with high-purity argon (< 100 ppm O_2). Each layer was scanned with a 170 W laser at 800 mm/s: first tracing the contour to sharpen edges, then melting the interior via a stripe-wise hatch (6 mm stripes, 0.1 mm overlap).

TruPrint 1000		
Build volume (cylinder)	mm x mm	Ø 100 x H 100 Optional: Smaller build volume
Processable materials[1]		Weldable metals in powder form, such as: Stainless steels, tool steels, aluminum[2], nickel-based, cobalt- chrome, copper, titanium[2] or precious metal[2] alloys, amorphous metals
Build rate[3]	cm³/h	10 - 50
Layer thickness[4]	μm	20 - 60
Max. laser power at the workpiece (TRUMPF fiber laser)	W	200 Optional multilaser: 2 x 200
Beam diameter	μm	80 Optional: 55/80
O_2 concentration	ppm	Down to 3000 (0.3%) Optional: down to 100 (0.01%)
Scan speed (powder bed)	m/s	Max. 2
Shielding gas		Nitrogen, argon
Power supply	V / A / Hz	230 – 7 – 50/60
Dimensions	mm	780 x 2050 x 1160
Weight (incl. powder)	kg	900

Figure 18) The TruPrint 1000 AM machine and its specifications [137].
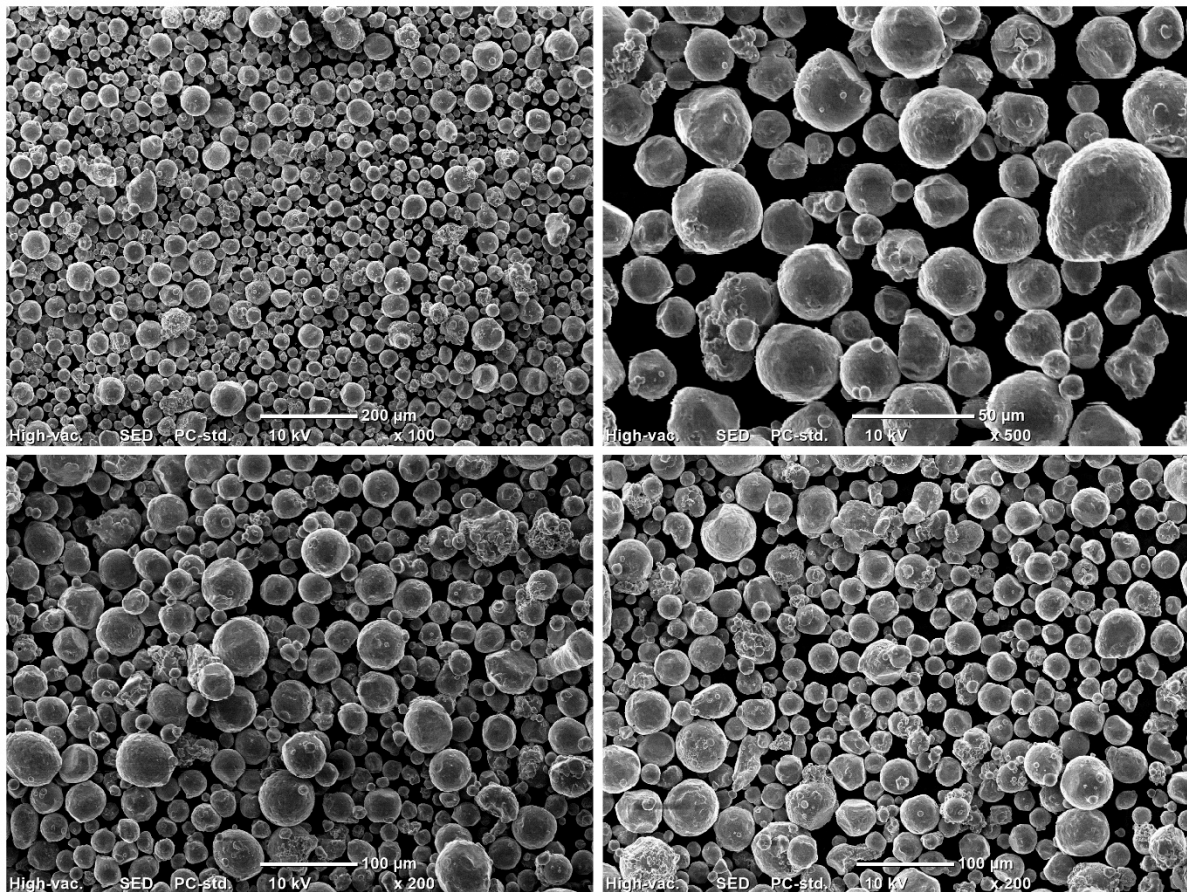
Figure 19) The SEM images of the AlSi10Mg powder used in the AM process

39

Table 2) Chemical composition of powder AlSi10Mg

Element	Al	Si	Fe	Cu	Mn	Mg	Ni	Zn	Pb	Sn	Ti
Composition (wt.%)	Balance	9-11	≤0.55	≤0.5	≤0.45	0.25-0.45	≤0.05	≤0.1	≤0.05	≤0.05	≤0.15

From these parameters the line energy (E_{line}) and the and the volumetric energy density (VED) can be calculated for each layer. Using the equation (1) and (2) these parameters also are listed in the Table 3.

$$E_{line} = \frac{P}{v} \tag{1}$$

$$VED = \frac{P}{v \times h \times t} \tag{2}$$

Table 3) The process parameters of the SLM process.

Parameter	Specification
Shielding gas type	Argon
Shielding gas speed	1.5 m/s
Layer thickness (t)	30 μm
Laser beam diameter	80 μm
Hatch pattern	Stripes
Stripe overlap	0.1 mm
Stripe width	6 mm
Hatch distance (h)	0.1 mm
Laser power (P)	170 W
Exposure speed (v)	800 mm/s
Line energy	0.2125 J/mm
Volume Energy	70.833 J/mm^3

Figure 20 presents in situ views and resulting builds on the TruPrint 1000. First, bright "sparks" trace the laser's contour pass around square test areas and then sweep inward in stripe-wise hatch passes to melt the powder (Figure 20-a). The annotated photo in Figure 20-b shows the build chamber's components: a powder-supply roller on the right, a recoater blade in the center depositing 30 μm layers on the 100 mm diameter platform, and an excess-powder reservoir on the left. Figure 20-c displays a photograph of the completed cubic compression samples immediately after printing; Figure 20-d shows a magnified viewport image of the molten powder fabricating two small cubic samples within a single layer.
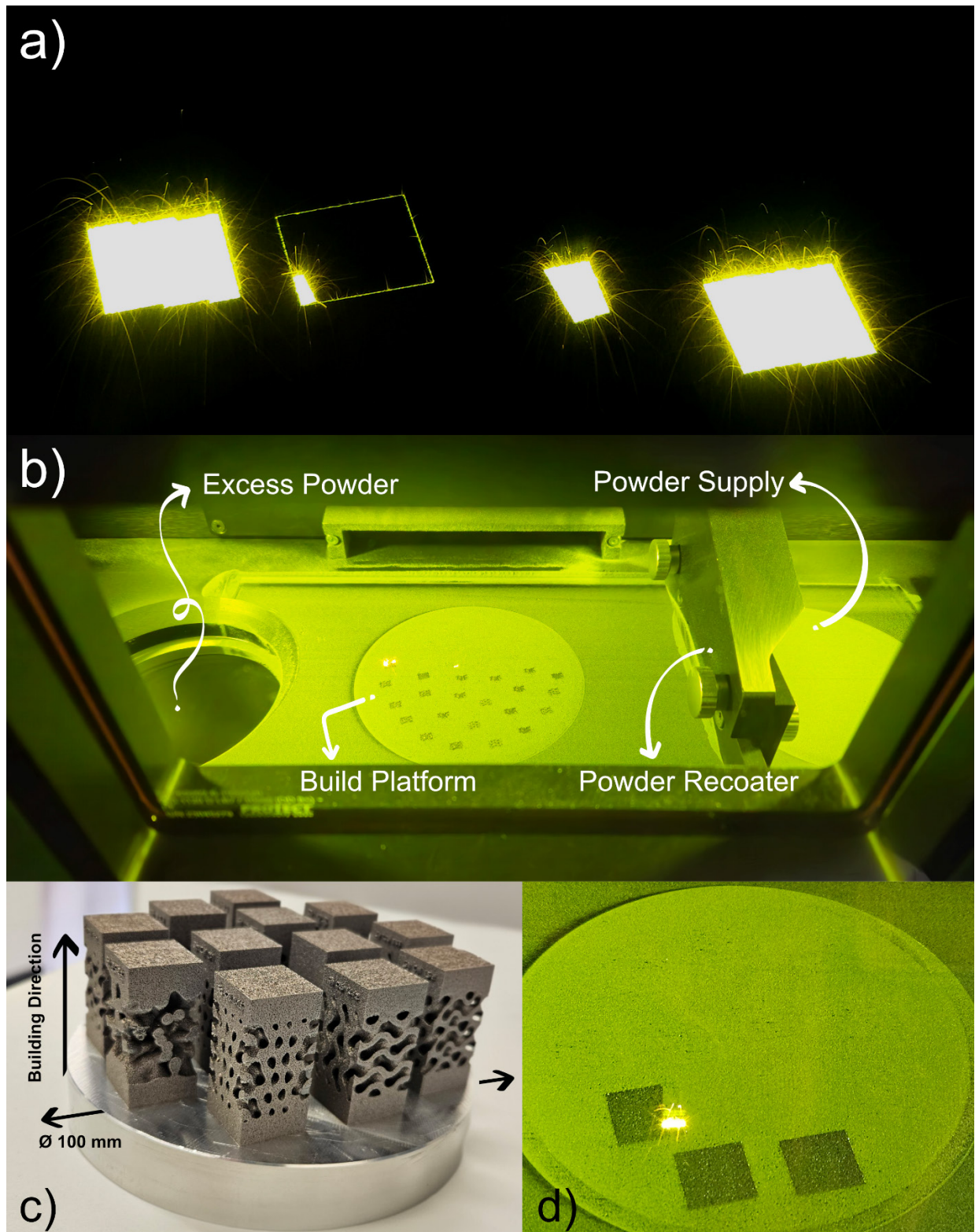
Figure 20) In-situ views and resulting builds on the TruPrint 1000. a) Laser-melting sequences showing the bright contour pass followed by hatch passes across square test areas. b) Annotated photograph of the build chamber: powder-supply roller (right), recoater blade (center), Ø100 mm build platform (middle), and excess-powder reservoir (left). c) Photograph of a completed build job of compression sample. d) Molten powder, cubic samples.

All tensile specimens (three per design) were built in a single job; the larger cubic compression samples (two per design) were split over two jobs, but under identical processing conditions. Following printing, specimens were separated from the build platform using a wire-cutting machine. Figure 21 and Figure 22 shows the cubic and dog-bone as-built samples, respectively.
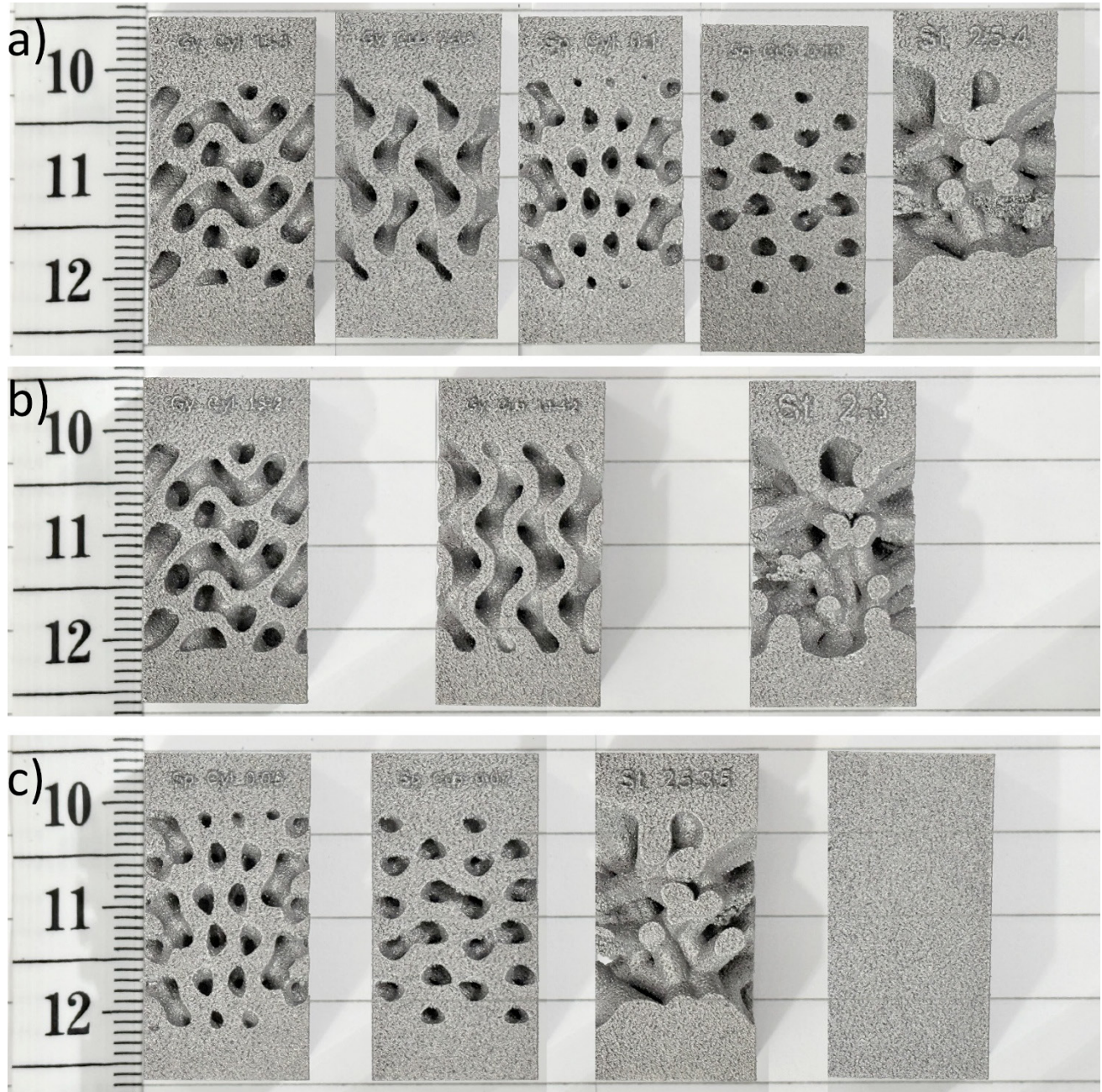
Figure 21) The as-built cubic compression samples cut from the by wire-cutting machine; classes a), b), c), 79–72–75 % relative volume and the last piece the bulk sample.
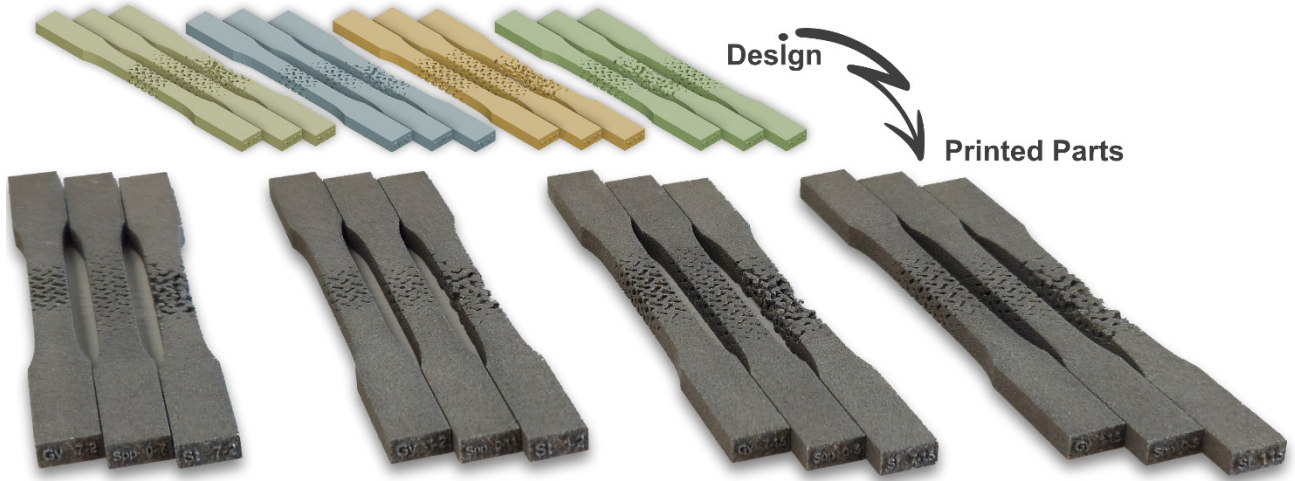
Figure 22) Dog-bone tensile samples printed by SLM method.

3.3 Quality Assurance

X-ray computed tomography (XCT), performed using the "Phoenix v|tome|x S" system, provides a non-destructive method for analyzing internal porosity (Figure 23). Scan parameters for the Phoenix v|tome|x S acquisition were as follows: the 3D cone beam was captured by a 2D flat-panel detector (DXR-250 RT) with an exposure time of 333.107 ms per projection; the X-ray source operated at 180 kV and 60 μA, with a 0.5 mm Cu filter and a standard target, yielding a focal spot size of 10.8 μm. This configuration generated hundreds of projections needed for a full 360° rotation around the sample.

To support this study, the software Dragonfly 2024.1 [139], developed by Comet Technologies Canada Inc., was selected to analyze the XCT data. Within Dragonfly, pores were classified as either closed (completely enclosed within the solid matrix) or open (connected to the exterior surface). Closed and open porosity percentages were then calculated by dividing the respective pore volumes by the total sample volume. To assess dimensional accuracy, the reconstructed surface of the printed sample was registered to its original CAD-derived STL mesh. A deviation map was generated by computing point-to-surface distances between the XCT-derived model and the nominal design mesh, yielding a quantitative distribution of deviations that indicates how closely the as-built geometry matches the intended design.

Figure 23) The software that has been used to analyze the XCT data (DragonFly), and the Phoenix v|tome|x S machine used to capture the data.

3.4 Mechanical Tests

Utilizing an Easydur 3Mz universal testing machine, tensile and compression tests were conducted (Figure 18). For the compression tests, the specimens were sandwiched between platen faces. A thin film of lubricating grease was applied to the contact surfaces to minimize friction and misalignment, thereby ensuring a uniform load distribution across the specimen during testing. Prior to each test, an initial preload of 1000 N was applied to eliminate any play in the machine and ensure full contact. The crosshead displacement rate was then set to 1 mm/s for all tests. Prior to testing the actual samples, a sacrificial "dummy" specimen was loaded to verify proper alignment and prevent any damage to the real test pieces. For the tensile test the displacement rate was set to 3 mm/s to keep the standard strain rate. To improve accuracy and repeatability in tensile testing, a custom fixture was used to maintain a precise 90° orientation between the specimen ends and jaws.

Each compression test was conducted twice, while each tensile test was performed three times. Following the earlier description, two cubic specimens and three specimens with a dog-bone shape were manufactured for each design. Ultimate compressive strength (UCS), ultimate tensile strength (UTS), compressive elastic modulus, and tensile elastic modulus were determined via testing. In addition, the energy absorption of the compression samples was computed.
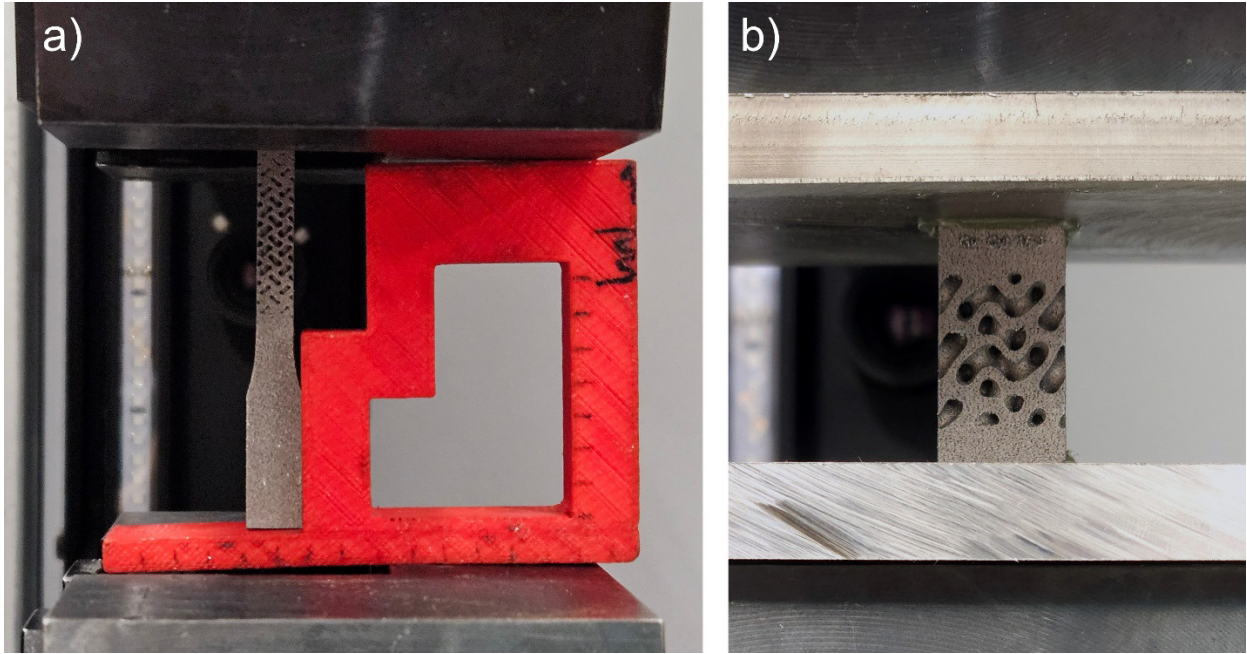
Figure 24) The a) tensile and b) compression test setup using the Easydur 3Mz testing machine

The compressive behavior of cellular materials is distinctly characterized by three phases as it is shown in Figure 19. Initially, the material deforms in a linear-elastic manner (Phase-I) as its cell walls bend. This is followed by a long plateau region (Phase-II), where the cells progressively collapse, allowing the material to undergo large deformations and absorb significant energy at a nearly constant force. Finally, the material enters a densification phase (Phase-III) when the collapsed cell walls press against each other, leading to a rapid increase in stiffness and a sharp rise in the compressive force [140].
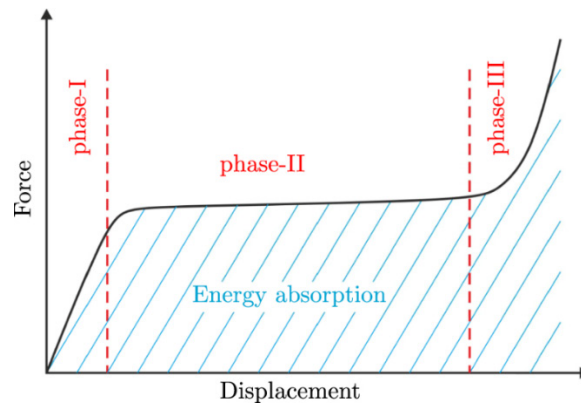
Figure 25) Force-displacement curve characteristic for cellular structures under compression [140].

To quantify the energy-absorption capacity of the compression specimens up to a strain of 0.2, the absorbed energy per unit volume was calculated as the area under the engineering stress–strain curve between $\varepsilon = 0$ and $\varepsilon = 0.2$, using the equation (3).

$$W_{abs} = \int_0^{0.2} \sigma(\varepsilon)d\varepsilon \tag{3}$$

In the Gibson–Ashby framework the relative density is defined as:

$$\bar{\rho} = \frac{\rho^*}{\rho_s} \tag{4}$$

where $\bar{\rho}$ is a normalized (or "relative") value and the ρ^* denotes the foam's apparent density (mass per unit volume including its voids) while the ρ_s identifies the intrinsic density of the solid parent material. By casting mechanical properties in terms of $\bar{\rho}$, the model succinctly captures how porosity governs stiffness and strength in cellular solids [141]. Specifically, open-cell foams obey;

$$\frac{\sigma^*}{\sigma_s} = C_\sigma \left(\frac{\rho^*}{\rho_s}\right)^{\frac{3}{2}} \qquad\qquad C_E = 1.0\ to\ 0.1 \tag{5}$$

$$\frac{E^*}{E_s} = C_E \left(\frac{\rho^*}{\rho_s}\right)^{2} \qquad\qquad C_E = 4.0\ to\ 0.1 \tag{6}$$

enabling direct comparison of measured σ^* and E^* to theoretical predictions based on cell-wall bending, yielding, and fracture mechanisms [142].

3.5 Fracture Analysis

Scanning electron microscopy (SEM) analysis was carried out on the fracture surfaces of the broken tensile specimens using the JEOL device to acquire high-resolution micrographs [143]. By imaging the failed ends of the samples, we were able to observe microscale features such as dimple formation, cell-wall pull-out, and crack-propagation paths, which provided crucial insights into the dominant fracture mechanisms and their relationship to the foam's cellular architecture and mechanical performance.

4 Result and Discussion

4.1 Quality Analysis

The following discussion details key findings from our XCT analysis of printed lattice samples, analyzing porosity and dimensional accuracy. Since all samples were produced using the same manufacturing process, any differences in XCT results must be due to design, not manufacturing inconsistencies. Therefore, two volume-matched subsets were chosen for XCT: three dog-bone tensile samples (Figure 28, GY-TA, SP-TA, ST-TA), with 95% relative volume, and five "A"-group cubic compression specimens (Figure 26, GY-CYL-A, GY-CU-A, SP-CYL-A, SP-CU-A, ST-2.5-A) with 79% relative volume. This choice allows us to isolate the effects of lattice design and part geometry on variations in open/closed porosity and CAD-to-print deviations.

Table 4 summarizes the volumetric porosity for each compression samples. The total porosity varies between 0.34% (SP-CYL-A) and 0.72% (ST-2.5-A). The uniformly low closed porosity (0.10–0.24%) suggests that most defects are open to the surface. Open porosity varies strongly with topology: the strut-based ST-2.5-A exhibits the highest open porosity (0.61%), whereas the SplitP design achieves the lowest (0.24%).

Printed parts exhibited minor under sizing, as evidenced by the slightly negative mean signed deviations between the XCT-reconstructed surfaces and the nominal cubic CAD STL (Table 4, Figure 26). Average deviations fell between –0.08 mm (SP-CYL-A) and –0.13 mm (ST-2.5-A), with Voronoi stochastic strut geometries deviating the most. The significant variation is probably due to the random arrangement of stochastic struts, which causes unpredictable overhangs and unsupported structures that are prone to defects in powder-bed fusion. An example is shown in Figure 27, where red regions indicate positive deviations (printed part locally larger than nominal), and blue regions indicate negative deviations (printed part locally smaller than nominal).

A clear trend emerges when porosity and mean deviation are considered jointly: the sample with the highest total porosity (ST-2.5-A, 0.72%) also exhibited the greatest negative deviation (–0.13 mm), whereas the lowest-porosity design (SP-CYL-A, 0.34%) showed the smallest under sizing (–0.08 mm). This indicates that areas with increased pore volume prevent complete consolidation, resulting in localized shrinkage and material reduction compared to the expected shape [144].
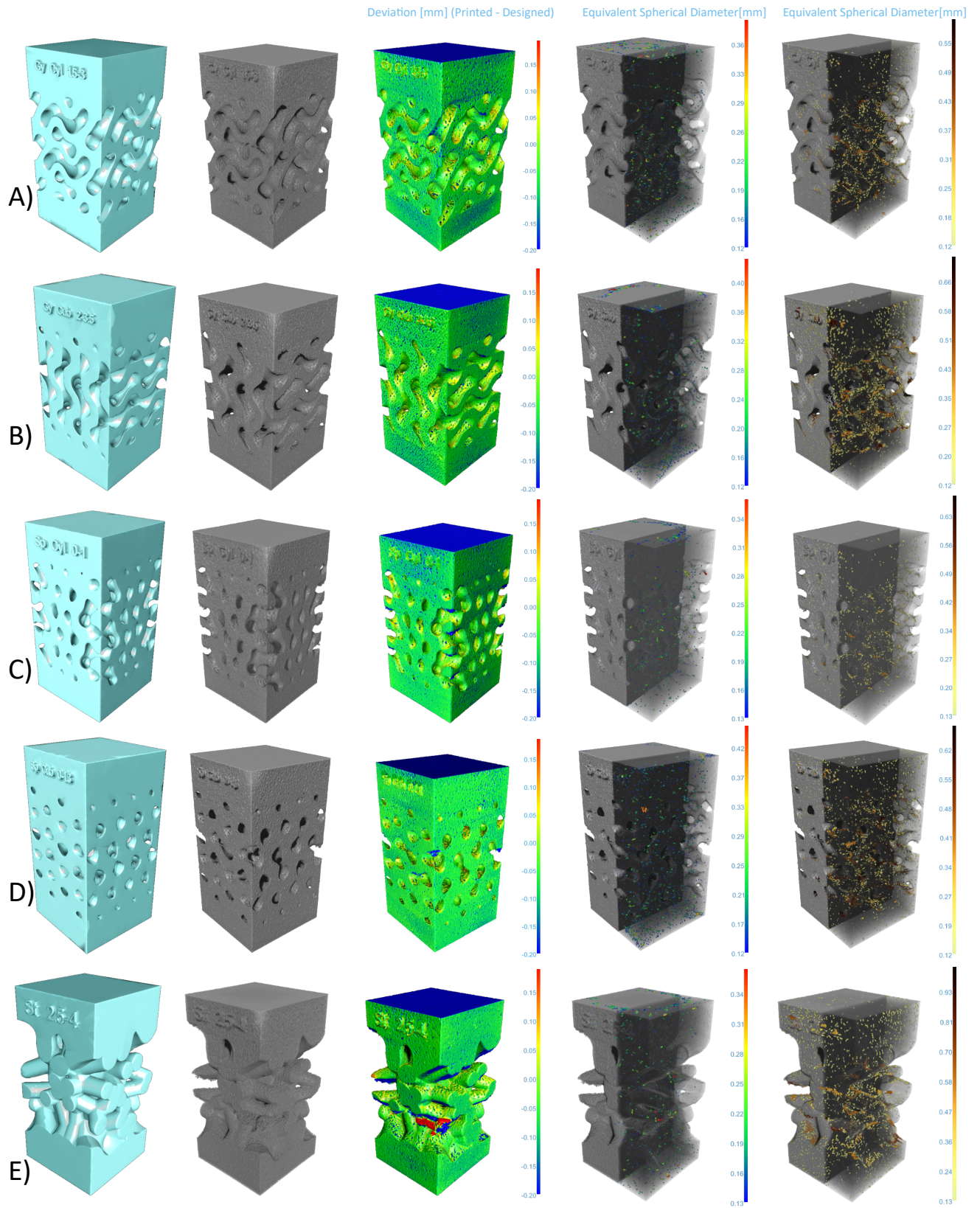
Figure 26) The designed model, XCT-derived model, deviation, close pores and open pores map for A) GY-CYL-A, B) GY-CU-A, C) SP-CYL-A, D) SP-CU-A, E) ST-2.5-A.
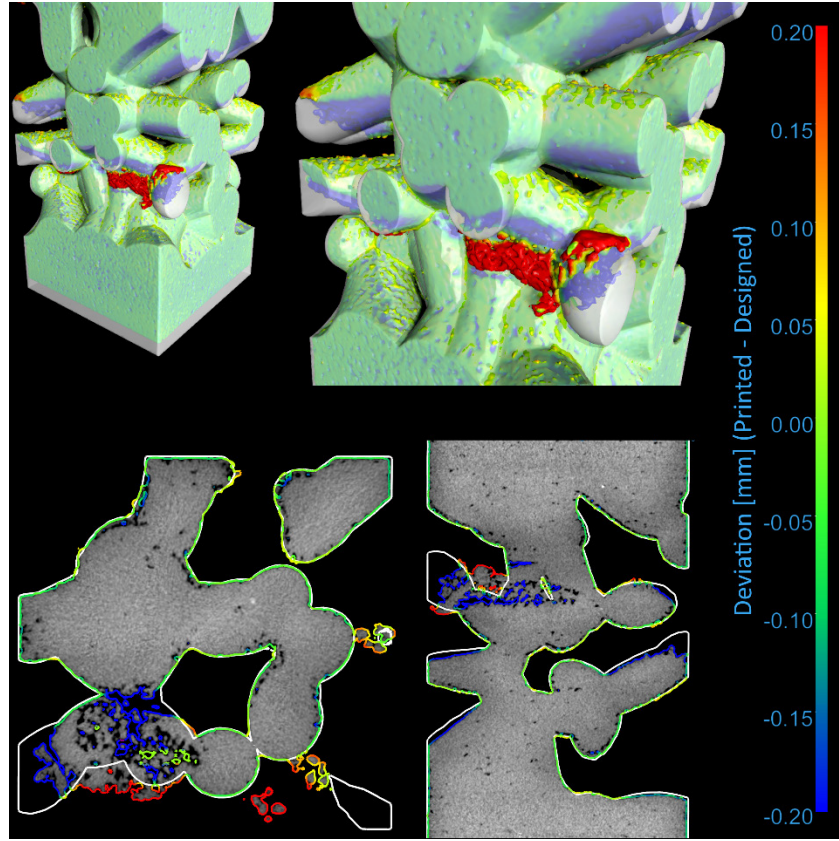
Figure 27) An example of the geometrical inaccuracy between designed part and printed part; positive deviations (larger than normal) are in red, negative (smaller) in blue.

Table 4) The result of XCT on compression samples with 79% relative volume.

Sample	Open Porosity	Close Porosity	Total Porosity	Mean Deviation [mm]
GY-CYL-A	0.37%	0.24%	0.61%	-0.10
GY-CU-A	0.55%	0.16%	0.71%	-0.10
SP-CYL-A	0.24%	0.10%	0.34%	-0.08
SP-CU-A	0.44%	0.18%	0.62%	-0.09
ST-2.5-A	0.61%	0.11%	0.72%	-0.13

Tensile sample analysis focused solely on the gauge section revealed lower overall porosity (Table 5). The range of closed-pore volume is 0.11–0.18%, while open porosity ranges from 0.13% to 0.26%, resulting in total porosities of 0.24%, 0.27%, and 0.44% for ST-TA, GY-TA, and SP-TA, respectively. Good dimensional accuracy is indicated by small mean signed deviations (–0.03 mm to –0.04 mm) between XCT-reconstructed surfaces and the dog-bone CAD STL (Table 5, Figure 28). GY-TA and SP-TA both have an average undersize of –0.03 mm, with ST-TA slightly larger at –0.04 mm.

49

Table 5) The result of XCT on dog-bone samples with 95% relative volume.

Sample	Open Porosity	Close Porosity	Total Porosity	Mean Deviation [mm]
GY-TA	0.13%	0.14%	0.27%	-0.03
SP-TA	0.26%	0.18%	0.44%	-0.03
ST-TA	0.13%	0.11%	0.24%	-0.04

Figure 28) The XCT-derived model, deviation, close pores and open pores map for gauge parts of samples: A) GY-TA, B) SP-TA, C) ST-TA.

4.2 Mechanical Characterization Analysis
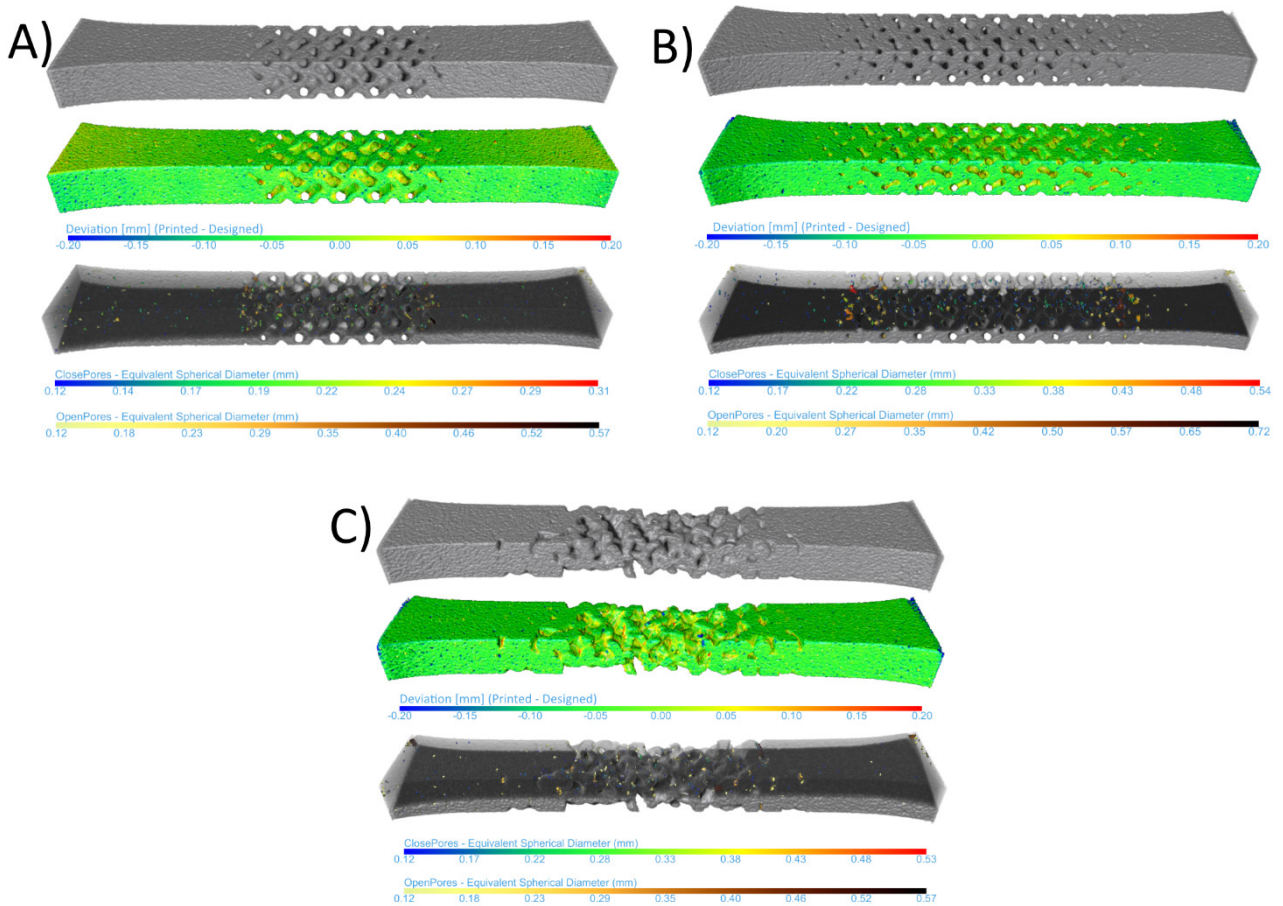
Mean mechanical properties were determined and reported for each specimen from plotted stress-strain curves. The results are presented in two distinct sections: compression tests and tension tests.

4.2.1 Compression Test Analysis

All cubic lattice geometries underwent compression testing, with the reported values representing the means of duplicate trials. As expected for cellular materials, every lattice exhibits the classic three-phase response; a linear-elastic rise to yield (~0–5% strain), a long plateau where struts buckle or collapse at nearly constant stress (5–15%), and finally a densification region where collapsed walls pack together, driving stress sharply upward, where the test was aborted. Compared to the solid ("Bulk") sample, which shows higher stiffness and strength (UCS ≈ 412 MPa) but almost no plateau, lattice structures achieve far greater energy absorption and deformation, though at a reduced peak load.

The Elastic Modulus measures the material's stiffness or resistance to elastic deformation, defined as the slope of the stress-strain curve within its linear elastic region, as demonstrated in Figure 29 for all the samples. For every specimen, this value was obtained by performing a best-fit linear regression on that portion of the curve and the mean value was reported in Figure 30. Across all lattice types, increasing relative volume correlates with increasing stiffness. A consistent pattern emerged in the cell mapping; regardless of lattice type (Gyroid or Split-P) and relative volume, cylindrical cell maps always showed slightly greater stiffness than cubic cell maps. At a constant relative density of 79 %, lattice topology strongly dictates stiffness: SplitP (SP) lattices are the stiffest, averaging 4.09 GPa (SP-CYL-A) and 3.90 GPa (SP-CU-A); gyroid (GY) structures follow at 3.87 GPa (GY-CYL-A) and 3.81 GPa (GY-CU-A); and stochastic (ST) networks are the most compliant at 3.38 GPa (ST-A). In short, SplitP lattices are roughly 5 % stiffer than gyroids and about 20 % stiffer than stochastic foams at the same volume fraction, making them the clear choice when maximizing elastic modulus is the goal.

Ultimate Compressive Strength (UCS) represents the maximum stress the material can withstand before failure begins. As demonstrated in Figure 31, higher relative volume consistently leads to higher strength. Regardless of lattice type (Gyroid or Split-P) and density, cylindrical cell maps continue to show superior strength performance. Considering the samples with 79% of relative volume (Blue bars), Gyroid-cylindrical specimens lead the pack at 149.7 MPa, followed by Split-P-cylindrical (137.2 MPa) and gyroid-cubic (133.7 MPa). Within each topology, the cylindrical cell map outperforms the cubic one: gyroid gains about 12% and Split-P about 12% in UCS when rendered with cylindrical cell map rather than cubic cell map. The TMPS structure's superior performance is evident as the stochastic Voronoi foam achieves a lower yield strength of 98.8 MPa. A density reduction from 79% to 75% leads to an approximate 13% decrease in UCS for Split-P-cylindrical (137 MPa to 120 MPa), an 8% reduction for Split-P-cubic (123 MPa to 112 MPa), and a 16% reduction for stochastic foam (99 MPa to 83 MPa). Reducing the percentage from 79% to 72% caused a substantial drop in gyroid strength: around 20% for cylindrical cells (150 to 119 MPa) and 29% for cubic cells (134 to 95 MPa). The stochastic network experienced a far greater reduction, falling by roughly 39% (99 to 60 MPa). It is worth mentioning that a lighter 72% gyroid-cylindrical lattice (~119 MPa) achieves almost identical compressive strength to a denser 75% Split-P-cylindrical lattice (~120 MPa).

51
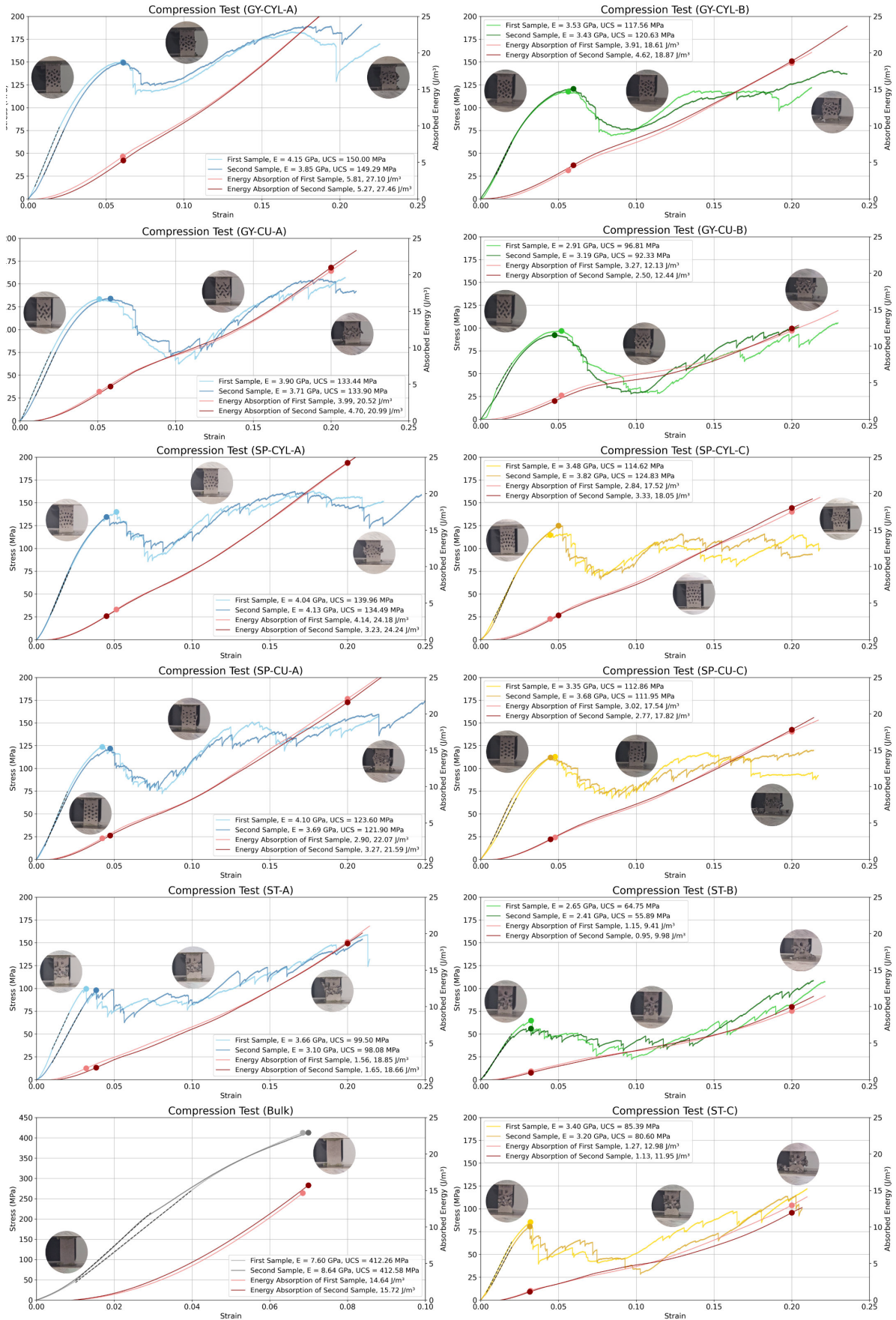
Figure 29) The stress-strain curve as a result of a compression test on all cubic samples, two for each design, demonstrating the UCS, EA, and the in-situ image of a sample at three different stages of a test.
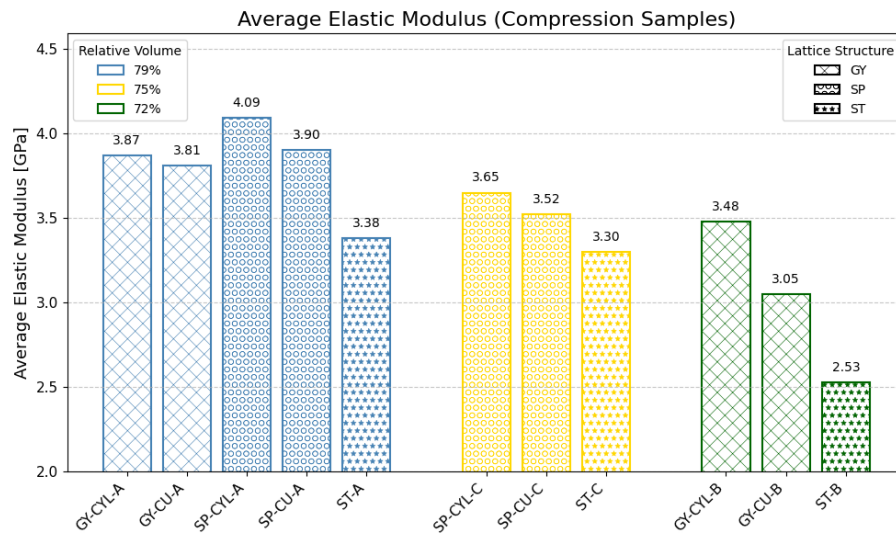
Figure 30) Average Elastic Modulus for each design extracted from the stress-strain curves.
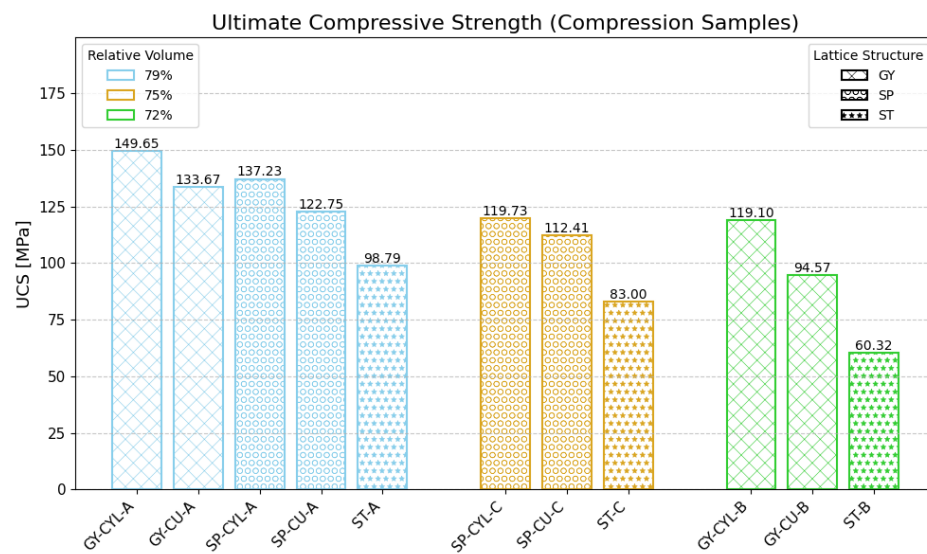
Figure 31) Average Ultimate Compressive Strength for each design extracted from the stress-strain curves.

Energy absorption (EA), calculated from the area under the stress-strain curve, is a measure of toughness and the ability to manage impact. Normalization can also be done by weight, resulting in specific energy absorption (SEA), calculated as the absorbed energy divided by the sample weight. Both values are presented in Figure 32. Once again, higher relative volume results in greater energy absorption, as there is more material to crush and deform. With an absorption of 27.28 J/m³, GY-CYL-A (79% vol) substantially outperformed ST-A (79% vol), which only managed 18.76 J/m³. Significantly, GY-CYL-A result is the highest among all lattices, exceeding the Bulk material's 15.18 J/m³ absorption by a remarkable 80%. Weight considered, Specific Energy Absorption analysis shows the lightweight Gyroid structure (2081.38 J/m³.Kg) to be over 2.3 times better at

absorbing energy per unit mass than the dense bulk material (896.28 J/m³.Kg). Moreover, the cylindrical cell map once again proved beneficial, enabling higher energy absorption than the cubic map for both Gyroid and Split-P designs. Switching from a cylindrical (SP-CYL-A, 24.21 J/m³) to a cubic (SP-CU-A, 21.83 J/m³) Split-P lattice map only decreases energy absorption by about 10%. In contrast, the Gyroid lattice exhibits a different behavior; the alteration in cell mapping is critical and transitioning from the cylindrical GY-CYL-A (27.28 J/m³) to the cubic GY-CU-A (20.76 J/m³) results in a significant performance reduction of approximately 24%. This trend is consistent across other relative volumes when transitioning between cylindrical and cubic cell mappings. The 72% gyroid-cylindrical part absorbed nearly as much energy as the heavier 75% Split-P parts in both AE and SAE terms. Using a gyroid-cylindrical design, you can reduce material by approximately 7% and achieve the same energy absorption as the heavier SplitP sample.
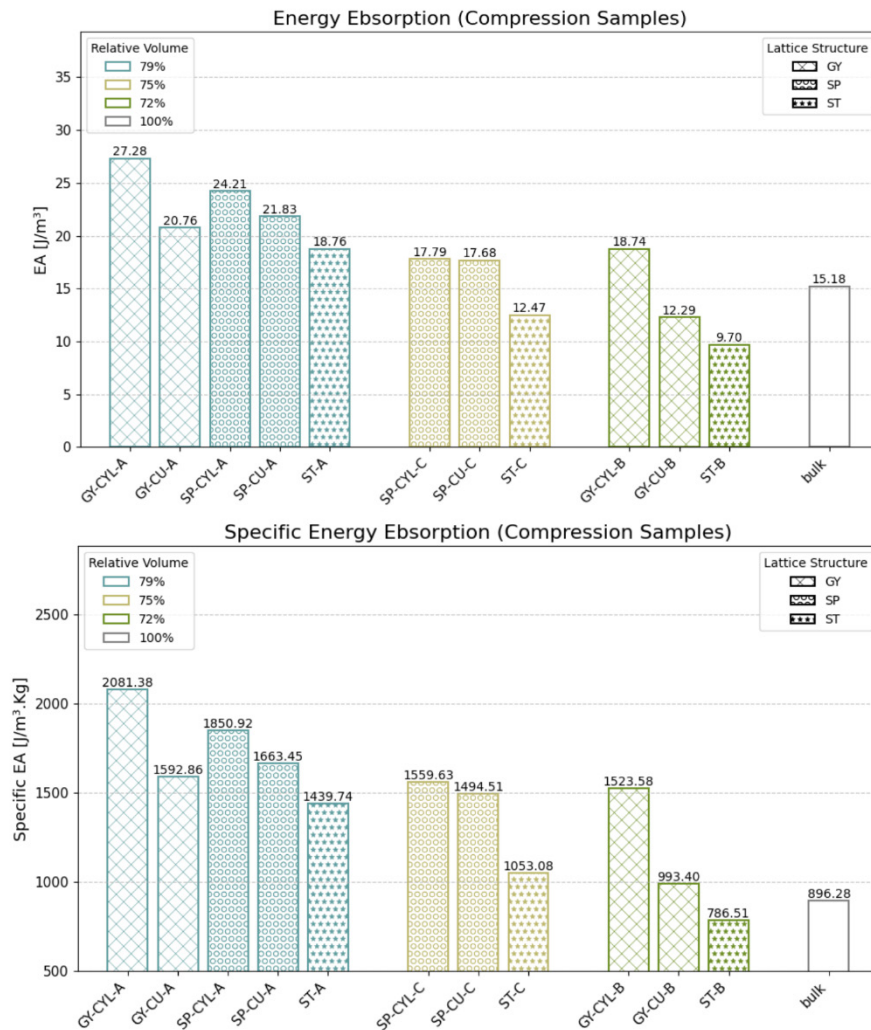
Figure 32) Average Energy Absorption (top), and Specific Energy Absorption (Bottom) for each design extracted from the area under stress-strain curves.

The measured stiffness and strength of our lattice architectures were found to lie squarely within the bounds predicted by the classic Gibson–Ashby scaling laws for open-cell foams [142]. Gibson and Ashby (1982, 1997) showed that Young's modulus and compressive strength in cellular solids follow power laws, equations (5) and (6), with experimentally determined prefactors ranging from approximately 0.1 to 4.0 for modulus and 0.1 to 1.0 for strength, depending on cell structure. As shown in Figure 33, our data points fall entirely within these empirically established bands, in agreement with numerous subsequent studies on lattices [142]. This correspondence confirms that the deformation mechanisms in our specimens are well captured by the Gibson–Ashby framework.
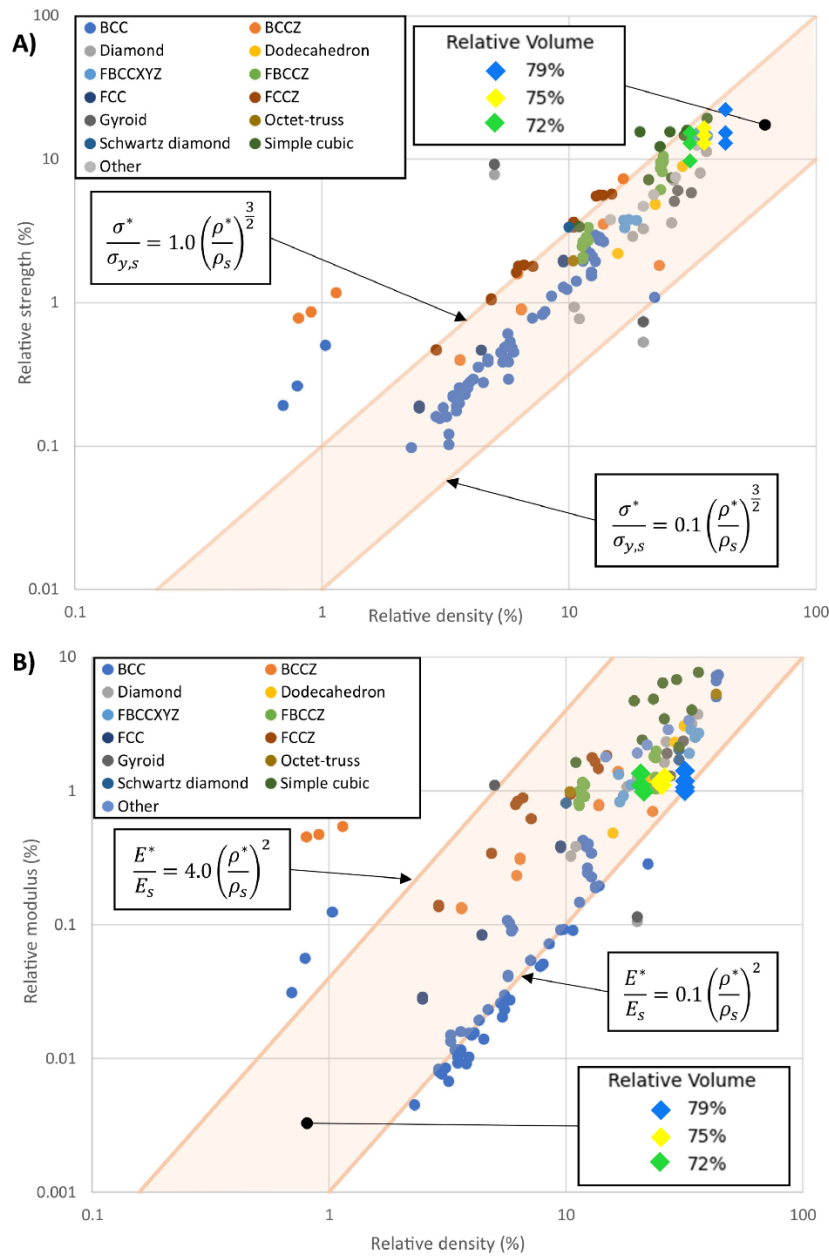
Figure 33) Relative strength (A) and stiffness (B) of various lattice unit cells plotted against relative density, with Gibson–Ashby law [142].

4.2.2 Tensile Test Analysis

Tensile testing was performed on all dog-bone samples, with the reported values averaging three trials for each design. The analysis of their stress-strain curves, Figure 34, revealed a brittle or semi-brittle material response: linear elastic behavior followed by catastrophic failure with minimal plastic deformation. Mechanical performance is heavily influenced by minimum wall thickness as well as relative volume, since tensile failure is most likely to occur in high-stress regions with small surface areas.

Elastic modulus in ST and SP lattices shows an almost inverse relationship with relative volume; a 1–3% decrease in density causes a roughly proportional decrease in stiffness. However, the gyroid's tensile stiffness depends on both its thinnest and thickest walls, simply the thickness gradient. Reducing the maximum wall thickness from 2 mm to 1.5 mm (minimum remains 1 mm, and volume fraction decreases from 97% to 96%) increases the Young's modulus from 4.15 GPa to 4.92 GPa. However, lowering the minimum from 1 to 0.7 mm (while keeping the maximum at 1.5 mm and volume percentage at 93%), E decreases to 4.37 GPa. For gyroids, increased stiffness results from lowering maximum thickness, while lowering minimum thickness decreases stiffness. The Figure 34 displays the average E value for each sample.

Under a tensile load, failure initiates at the weakest point, which is usually the cross-section with the smallest area. Samples with a 1 mm minimum thickness are significantly stronger than those with a 0.7 mm minimum thickness, as the data clearly shows in Figure 35. The impact is clear: with a UTS of 97.37 MPa, the ST-TD sample (1-1.5 mm) significantly outperformed the ST-TA sample (0.7-2 mm), which failed at only 79.77 MPa. The Gyroid architecture shows a more significant trend: the GY-TB sample (1–2 mm) achieved a UTS of 93.95 MPa, exceeding the GY-TA sample's (0.7–2 mm) UTS of 58.19 MPa by over 60%. This confirms that a larger minimum thickness directly increases the structure's ability to withstand tensile forces. With a constant minimum thickness in all Split-P samples, the influence of maximum thickness can be uniquely investigated. Observations indicate a clear trend: as the maximum offset (and thus maximum thickness) is progressively reduced, the tensile strength of the Split-P samples also decreases. Specifically, a reduction in maximum offset from 1.1 mm (SP-TB, 86.93 MPa) to 0.9 mm (SP-TD, 80.08 MPa), and further to 0.5 mm (SP-TC, 68.53 MPa), consistently led to a reduction in UTS.

Although reducing maximum thickness significantly weakens tensile strength, the effect is less pronounced than that of reducing minimum thickness. The total strength reduction across the tested range for Split-P samples, attributed to variations in maximum thickness, was approximately 27%. The reduction observed here is much lower than the nearly 55% reduction found in Gyroid samples of reduced minimum thickness (comparing GY-TB and GY-TA). This comparative analysis reinforces the conclusion that, although overall material density and maximum thickness contribute to the mechanical performance, the absolute thinnest section within the lattice structure represents the most critical point of failure under tensile stress. Therefore, ensuring a robust minimum thickness is paramount for optimizing the tensile strength of such architected materials.
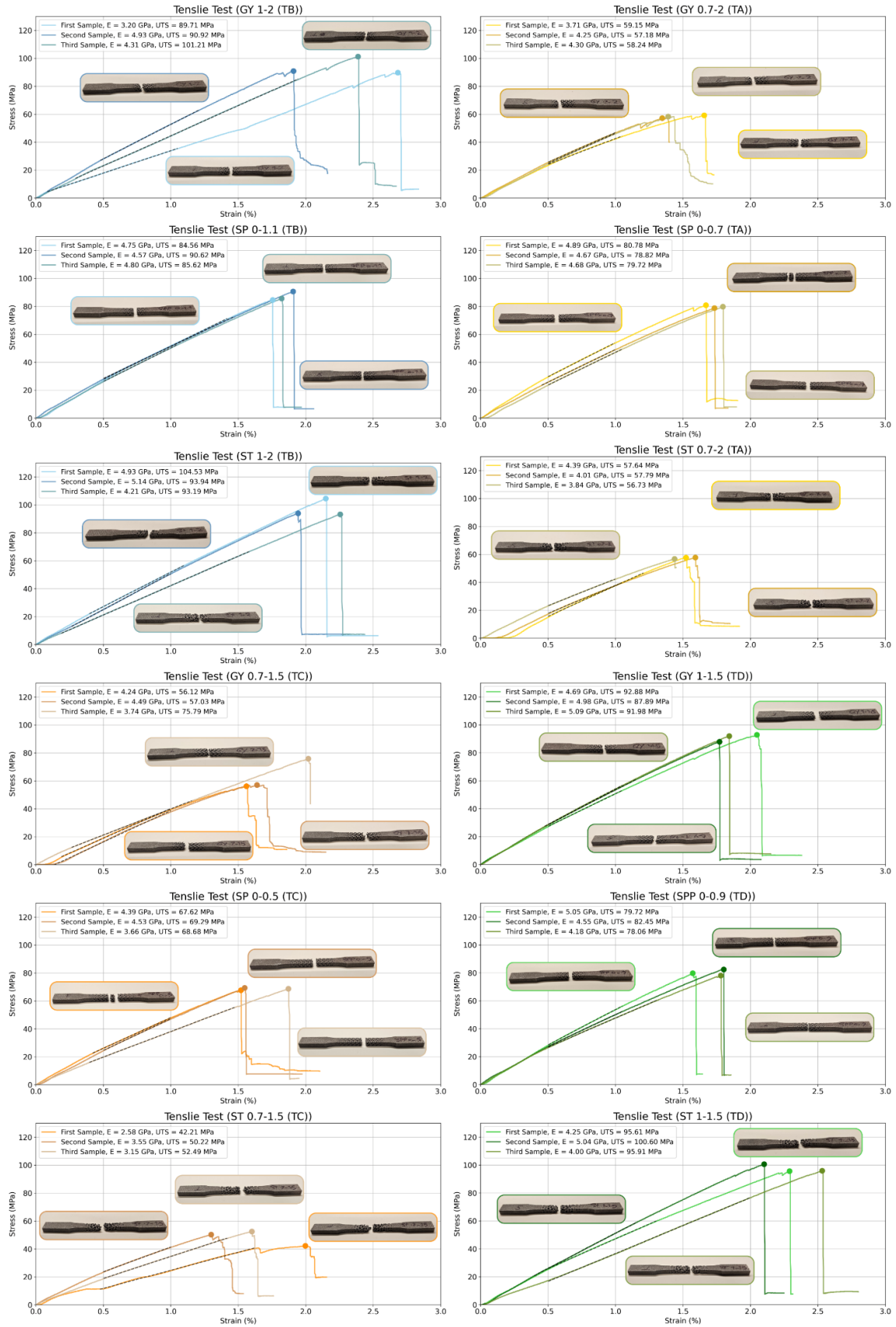
Figure 34) The stress-strain curves, a result of a tensile test on all dog-bone samples, three for each design, demonstrating the UTS and the image of a each sample (colour coded) after failure.
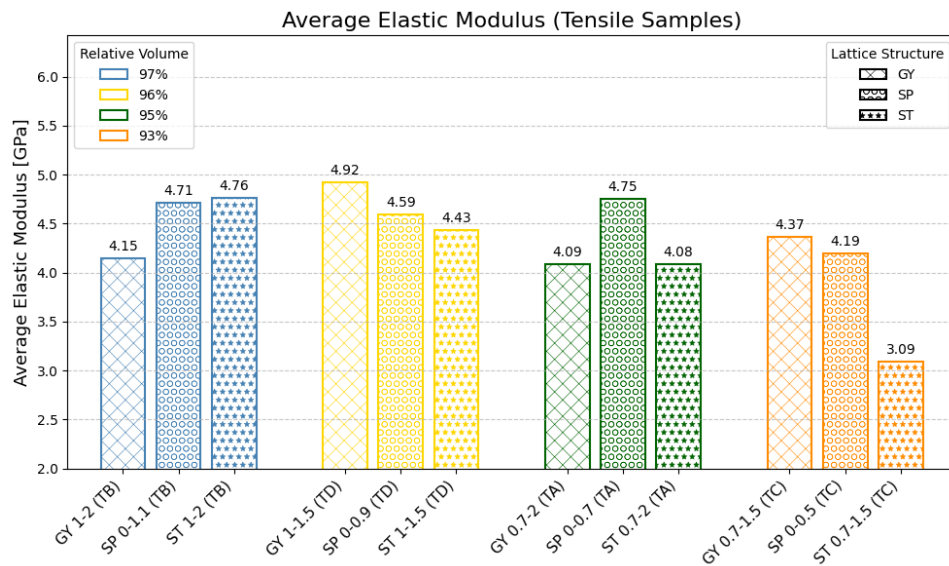
Figure 35) Average Elastic Modulus for each design extracted from the stress-strain curves.
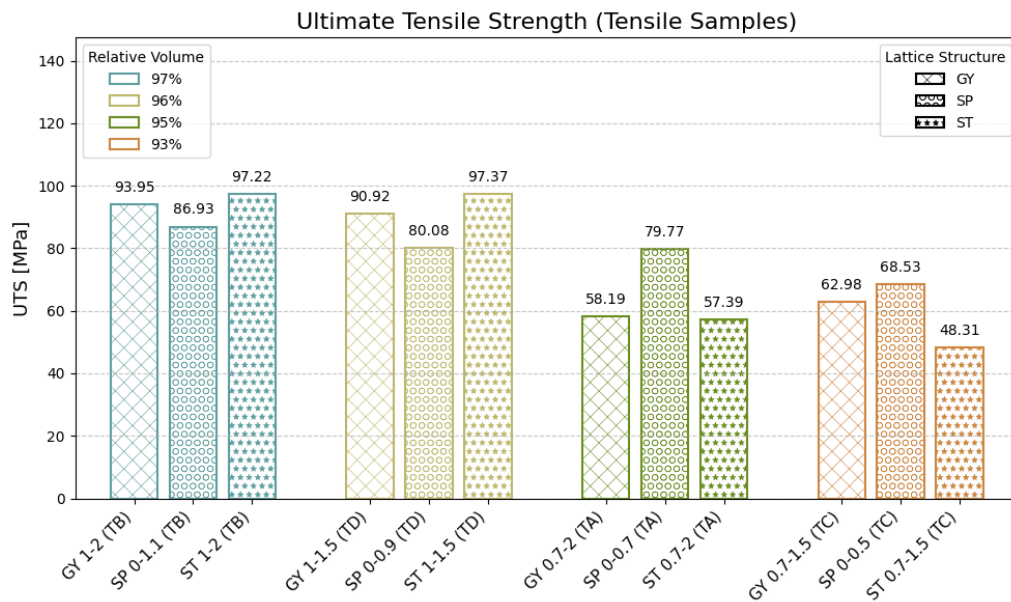
Figure 36) Average Ultimate Tensile Strength for each design extracted from the stress-strain curves.

4.3 Fractography Result

Despite being a ductile alloy, as-built AlSi10Mg (without post-heat-treatment) typically exhibits low macroscopic ductility, especially in thin struts, because of its LPBF microstructure (fine α-Al cells, a rigid Si network, residual stresses, and some porosity) [145]. Figure 37 displays the fracture morphologies for as-built components, including post-compression (Figure 37a), post-tension lattice (Figure 37b), and post-tension bulk samples (Figure 37c,d). Fracture analysis of the LPBF-produced AlSi10Mg alloy samples revealed a

predominantly mixed brittle-ductile fracture behavior. Significant plastic deformation, indicated by dimple formation on the fracture surface, is a key feature of ductile failure. This texture arises from the merging of microscopic voids under stress, absorbing substantial energy before fracture (Figure 37a). In contrast, flat, faceted regions arranged in "river" or "step" patterns, known as stepped cleavage planes, signify a brittle fracture; the crack propagates rapidly with limited plasticity and energy dissipation (Figure 37c,d). Thin, rough struts with porosity or additive manufacturing, like rough build layers as in Figure 37b, defects exhibit low ductility, resulting in sudden fracture under localized high stress and brittle behavior, even in ductile alloys such as AlSi10Mg. This mixed brittle-ductile fracture behavior is also seen in tensile and compressive stress-strain curves.
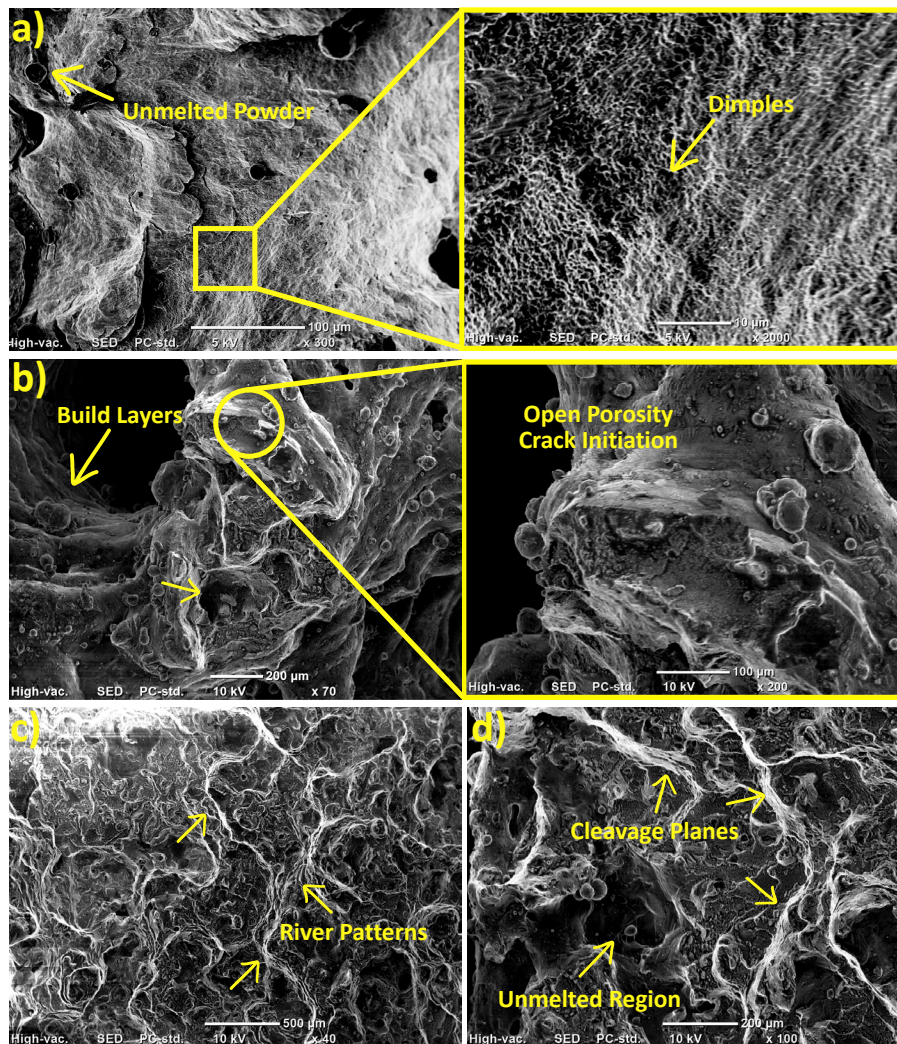
Figure 37) SEM fractography of as-built LPBF AlSi10Mg: (a) dimpled ductile regions of cubic sample after compression test; (b) rough build-layer morphology with unmelted powder and porosity crack initiation of a dog-bone part after tensile test; (c) "river" patterns of stepped cleavage; (d) faceted cleavage planes adjacent to unmelted areas of a bulk dog-bone sample after tensile test, illustrating mixed ductile–brittle failure.

5 Conclusion

In this study, three functional-graded lattice (FGL) architectures—gyroid, split-P, and stochastic Voronoi—were investigated to assess their influence on mechanical performance. Eleven cubic specimens were first designed by varying lattice type, cell mapping strategy, and thickness gradient; these were organized into three groups matched in mass and relative volume. Subsequently, twelve dog-bone specimens were designed with each of the three lattice geometries incorporated into the gauge section and arranged into three mass-equivalent sets with distinct thickness-gradient profiles. All samples were fabricated from AlSi10Mg alloy by laser powder bed fusion. Manufacturing quality and geometric fidelity were verified by X-ray computed tomography inspection. Mechanical responses were characterized through uniaxial compression and tension testing. Finally, fracture surfaces were examined by scanning electron microscopy to elucidate the failure mechanisms associated with each lattice design.

According to the research conducted on the design and mechanical characteristics of the additively manufactured FGLs, the following outcomes can be drawn:

- Higher porosity led to greater undersizing (ST-2.5-A: 0.72% porosity, –0.13 mm; SP-CYL-A: 0.34%, –0.08 mm), indicating that increased pore volume hinders consolidation and causes localized shrinkage.
- Three phases were observed in compression stress-strain curves: linear elasticity, plateau (buckling), and densification. Unlike the solid sample, with its high stiffness and strength (UCS ≈ 412 MPa) but minimal plateau, lattice structures demonstrate significantly enhanced energy absorption and deformation.
- Considering compressive properties, across both Gyroid and Split-P lattices, higher relative volume boosts stiffness, strength (UCS), and energy absorption. In every case, at any density, cylindrical cell maps outperform cubic ones.
- In cubic samples, switching from cylindrical to cubic in Split-P cuts energy absorption by only 10% (24.21→21.83 J/m³), but in Gyroid it drops 24% (27.28→20.76 J/m³). Consequently, a 72% gyroid-cylindrical design matches the energy absorption of a 75% Split-P part, saving 7% material.
- Considering tensile specimens, in ST and Split-P lattices, stiffness scales nearly one to one with relative volume—a 1–3% drop in density yields an almost equal decrease in elastic modulus. Gyroids, however, derive their tensile stiffness from the wall thickness gradient:
    1. Reducing maximum wall thickness from 2 mm to 1.5 mm (minimum held at 1 mm; volume fraction drops 97→96%) raises Young's modulus from 4.15 to 4.92 GPa.
    2. Reducing minimum wall thickness from 1 mm to 0.7 mm (maximum held at 1.5 mm; volume fraction ≈93%) lowers modulus to 4.37 GPa.

    Thus, in gyroid lattices lowering the thickest walls stiffens the structure, while thinning the smallest walls softens it.

- Although density and maximum thickness matter, tensile failure is controlled by the lattice's thinnest section—so maximizing the minimum wall thickness is essential for strength.
- Even though AlSi10Mg is a ductile alloy, thin struts made from it without post-heat treatment tend to exhibit poor macroscopic ductility. AM defects like porosity or rough build layers resulting in sudden fracture under localized high stress and brittle behavior, even in ductile alloys like AlSi10Mg.

In conclusion, this thesis successfully executed a direct comparative analysis of Gyroid, Split-P, and Stochastic Voronoi functionally graded lattice structures fabricated from AlSi10Mg. The investigation revealed distinct mechanical behaviors and failure modes inherent to each topology, providing a systematic understanding of their relative performance under both tensile and compressive loads. These findings offer crucial guidance for engineers and designers, helping them choose the best lattice architecture for specific loads. This is vital for better biomedical implants that match natural biological gradients, and for other applications like aerospace and automotive design.

6 References

[1] I. Gibson, D. Rosen, B. Stucker, Additive Manufacturing Technologies: 3D Printing, Rapid Prototyping, and Direct Digital Manufacturing, Springer, New York, NY, 2015. https://doi.org/10.1007/978-1-4939-2113-3.

[2] K.V. Wong, A. Hernandez, A Review of Additive Manufacturing, International Scholarly Research Notices 2012 (2012) 208760. https://doi.org/10.5402/2012/208760.

[3] C. Weller, R. Kleer, F.T. Piller, Economic implications of 3D printing: Market structure models in light of additive manufacturing revisited, International Journal of Production Economics 164 (2015) 43–56. https://doi.org/10.1016/j.ijpe.2015.02.020.

[4] M. Attaran, The rise of 3-D printing: The advantages of additive manufacturing over traditional manufacturing, Business Horizons 60 (2017) 677–688. https://doi.org/10.1016/j.bushor.2017.05.011.

[5] A. Gebhardt, Layer Manufacturing Processes, in: Understanding Additive Manufacturing, Carl Hanser Verlag GmbH & Co. KG, 2011: pp. 31–63. https://doi.org/10.3139/9783446431621.002.

[6] D.L. Bourell, Perspectives on Additive Manufacturing, Annual Review of Materials Research 46 (2016) 1–18. https://doi.org/10.1146/annurev-matsci-070115-031606.

[7] Committee F42 on Additive Manufacturing Technologies | ASTM, Committee F42 on Additive Manufacturing Technologies | ASTM (n.d.). https://www.astm.org (accessed June 10, 2025).

[8] M.K. Thompson, G. Moroni, T. Vaneker, G. Fadel, R.I. Campbell, I. Gibson, A. Bernard, J. Schulz, P. Graf, B. Ahuja, F. Martina, Design for Additive Manufacturing: Trends, opportunities, considerations, and constraints, CIRP Annals 65 (2016) 737–760. https://doi.org/10.1016/j.cirp.2016.05.004.

[9] M. Leary, 4 - Detail DFAM, in: M. Leary (Ed.), Design for Additive Manufacturing, Elsevier, 2020: pp. 91–122. https://doi.org/10.1016/B978-0-12-816721-2.00004-X.

[10] C.W. Hull, Apparatus for production of three-dimensional objects by stereolithography, US4575330A, 1986. https://patents.google.com/patent/US4575330A/en (accessed June 11, 2025).

[11] C.R. Deckard, Method and apparatus for producing parts by selective sintering, US4863538A, 1989. https://patents.google.com/patent/US4863538A/en (accessed June 11, 2025).

[12] R.D. Goodridge, C.J. Tuck, R.J.M. Hague, Laser sintering of polyamides and other polymers, Progress in Materials Science 57 (2012) 229–267. https://doi.org/10.1016/j.pmatsci.2011.04.001.

[13] S.S. Crump, Apparatus and method for creating three-dimensional objects, US5121329A, 1992. https://patents.google.com/patent/US5121329A/en (accessed June 11, 2025).

[14] B.N. Turner, R. Strong, S.A. Gold, A review of melt extrusion additive manufacturing processes: I. Process design and modeling, Rapid Prototyping Journal 20 (2014) 192–204. https://doi.org/10.1108/RPJ-01-2013-0012.

[15] G.N. Levy, R. Schindel, J.P. Kruth, RAPID MANUFACTURING AND RAPID TOOLING WITH LAYER MANUFACTURING (LM) TECHNOLOGIES, STATE OF THE ART AND FUTURE PERSPECTIVES, CIRP Annals 52 (2003) 589–609. https://doi.org/10.1016/S0007-8506(07)60206-6.

[16] D.T. Pham, R.S. Gault, A comparison of rapid prototyping technologies, International Journal of Machine Tools and Manufacture 38 (1998) 1257–1287. https://doi.org/10.1016/S0890-6955(97)00137-5.

[17] J.-P. Kruth, G. Levy, F. Klocke, T.H.C. Childs, Consolidation phenomena in laser and powder-bed based layered manufacturing, CIRP Annals 56 (2007) 730–759. https://doi.org/10.1016/j.cirp.2007.10.004.

[18] R. Bogue, 3D printing: the dawn of a new era in manufacturing?, Assembly Automation 33 (2013) 307–311. https://doi.org/10.1108/AA-06-2013-055.

[19] R. D'Aveni, The 3-D Printing Revolution, Harvard Business Review (n.d.). https://hbr.org/2015/05/the-3-d-printing-revolution (accessed June 11, 2025).

[20] Minetola, Paolo, Additive Manufacturing Systems and Materials (05SQSYP), (2024). http://iam.polito.it.

[21]   A Review of Vat Photopolymerization Technology: Materials, Applications, Challenges, and Future Trends of 3D Printing, (n.d.). https://www.mdpi.com/2073-4360/13/4/598 (accessed June 11, 2025).

[22]   Polymers for 3D Printing and Customized Additive Manufacturing | Chemical Reviews, (n.d.). https://pubs.acs.org/doi/10.1021/acs.chemrev.7b00074 (accessed June 11, 2025).

[23]   Inkjet Printing—Process and Its Applications - Singh - 2010 - Advanced Materials - Wiley Online Library, (n.d.). https://advanced.onlinelibrary.wiley.com/doi/10.1002/adma.200901141 (accessed June 11, 2025).

[24]   A. Mostafaei, A.M. Elliott, J.E. Barnes, F. Li, W. Tan, C.L. Cramer, P. Nandwana, M. Chmielus, Binder jet 3D printing—Process parameters, materials, properties, modeling, and challenges, Progress in Materials Science 119 (2021) 100707. https://doi.org/10.1016/j.pmatsci.2020.100707.

[25]   Y. Bai, C.B. Williams, An exploration of binder jetting of copper, Rapid Prototyping Journal 21 (2015) 177–185. https://doi.org/10.1108/RPJ-12-2014-0180.

[26]   M. Farbakhti, S. Aghaie, N.S.R. Jafari, S.R.E. Hosseini, A.A.B. Pereira, F.A.O. Fernandes, C. Chen, M. Farbakhti, A Review on the Metal Additive Manufacturing Processes, (2023). https://doi.org/10.20944/preprints202308.0173.v1.

[27]   T.D. Ngo, A. Kashani, G. Imbalzano, K.T.Q. Nguyen, D. Hui, Additive manufacturing (3D printing): A review of materials, methods, applications and challenges, Composites Part B: Engineering 143 (2018) 172–196. https://doi.org/10.1016/j.compositesb.2018.02.012.

[28]   M. Vaezi, H. Seitz, S. Yang, A review on 3D micro-additive manufacturing technologies, Int J Adv Manuf Technol 67 (2013) 1721–1754. https://doi.org/10.1007/s00170-012-4605-2.

[29]   Laser additive manufacturing of metallic components: materials, processes and mechanisms - D D Gu, W Meiners, K Wissenbach, R Poprawe, 2012, (n.d.). https://journals.sagepub.com/doi/full/10.1179/1743280411Y.0000000014 (accessed June 11, 2025).

[30]   Laminated Object Manufacturing, a New Process for the Direct Manufacture of Monolithic Ceramics and Continuous Fiber CMCs - Klosterman - 1997 - Ceramic Engineering and Science Proceedings - Wiley Online Library, (n.d.). https://ceramics.onlinelibrary.wiley.com/doi/10.1002/9780470294444.ch13 (accessed June 11, 2025).

[31]   K. Ishfaq, Z. Abas, M.S. Kumar, M.A. Mahmood, Review of recent trends in ultrasonic additive manufacturing: current challenges and future prospects, Rapid Prototyping Journal 29 (2023) 1195–1211. https://doi.org/10.1108/RPJ-09-2022-0300.

[32]   S.M. Thompson, L. Bian, N. Shamsaei, A. Yadollahi, An overview of Direct Laser Deposition for additive manufacturing; Part I: Transport phenomena, modeling and diagnostics, Additive Manufacturing 8 (2015) 36–62. https://doi.org/10.1016/j.addma.2015.07.001.

[33]   J.M. Flynn, A. Shokrani, S.T. Newman, V. Dhokia, Hybrid additive and subtractive machine tools – Research and industrial developments, International Journal of Machine Tools and Manufacture 101 (2016) 79–101. https://doi.org/10.1016/j.ijmachtools.2015.11.007.

[34]   B. Vayre, F. Vignat, F. Villeneuve, Metallic additive manufacturing: state-of-the-art review and prospects, Mechanics & Industry 13 (2012) 89–96. https://doi.org/10.1051/meca/2012003.

[35]   T. DebRoy, H.L. Wei, J.S. Zuback, T. Mukherjee, J.W. Elmer, J.O. Milewski, A.M. Beese, A. Wilson-Heid, A. De, W. Zhang, Additive manufacturing of metallic components – Process, structure and properties, Progress in Materials Science 92 (2018) 112–224. https://doi.org/10.1016/j.pmatsci.2017.10.001.

[36]   N. Shahrubudin, T.C. Lee, R. Ramlan, An Overview on 3D Printing Technology: Technological, Materials,   and   Applications,   Procedia   Manufacturing   35   (2019)   1286–1296. https://doi.org/10.1016/j.promfg.2019.06.089.

[37]   Thermo-mechanical properties of 3D printed photocurable shape memory resin for clear aligners | Scientific Reports, (n.d.). https://www.nature.com/articles/s41598-022-09831-4 (accessed June 11, 2025).

[38]   L.E. Murr, S.M. Gaytan, D.A. Ramirez, E. Martinez, J. Hernandez, K.N. Amato, P.W. Shindo, F.R. Medina, R.B. Wicker, Metal Fabrication by Additive Manufacturing Using Laser and Electron Beam Melting   Technologies,   Journal   of   Materials   Science   &   Technology   28   (2012)   1–14. https://doi.org/10.1016/S1005-0302(12)60016-4.

[39]   The metallurgy and processing science of metal additive manufacturing - W. J. Sames, F. A. List,   S.   Pannala,   R.   R.   Dehoff,   S.   S.   Babu,   2016,   (n.d.). https://journals.sagepub.com/doi/abs/10.1080/09506608.2015.1116649 (accessed June 12, 2025).

[40]   N.T. Aboulkhair, N.M. Everitt, I. Ashcroft, C. Tuck, Reducing porosity in AlSi10Mg parts processed   by   selective   laser   melting,   Additive   Manufacturing   1–4   (2014)   77–86. https://doi.org/10.1016/j.addma.2014.08.001.

[41]   L. Thijs, F. Verhaeghe, T. Craeghs, J.V. Humbeeck, J.-P. Kruth, A study of the microstructural evolution   during   selective   laser   melting   of   Ti–6Al–4V,   Acta   Materialia   58   (2010)   3303–3312. https://doi.org/10.1016/j.actamat.2010.02.004.

[42]   B. Vrancken, L. Thijs, J.-P. Kruth, J. Van Humbeeck, Heat treatment of Ti6Al4V produced by Selective Laser Melting: Microstructure and mechanical properties, Journal of Alloys and Compounds 541 (2012) 177–185. https://doi.org/10.1016/j.jallcom.2012.07.022.

[43]   Z. Chen, Z. Li, J. Li, C. Liu, C. Lao, Y. Fu, C. Liu, Y. Li, P. Wang, Y. He, 3D printing of ceramics: A review, Journal of the European Ceramic Society 39 (2019) 661–687. https://doi.org/10.1016/j.jeurceramsoc.2018.11.013.

[44]   Additive Manufacturing of Ceramic-Based Materials - Travitzky - 2014 - Advanced Engineering Materials - Wiley Online Library, (n.d.). https://advanced.onlinelibrary.wiley.com/doi/abs/10.1002/adem.201400097 (accessed June 12, 2025).

[45]   S. Bose, E.K. Akdogan, V.K. Balla, S. Ciliveri, P. Colombo, G. Franchin, N. Ku, P. Kushram, F. Niu, J. Pelz, A. Rosenberger, A. Safari, Z. Seeley, R.W. Trice, L. Vargas-Gonzalez, J.P. Youngblood, A. Bandyopadhyay, 3D printing of ceramics: Advantages, challenges, applications, and perspectives, Journal of the American Ceramic Society 107 (2024) 7879–7920. https://doi.org/10.1111/jace.20043.

[46]   J.R.C. Dizon, A.H. Espera, Q. Chen, R.C. Advincula, Mechanical characterization of 3D-printed polymers, Additive Manufacturing 20 (2018) 44–67. https://doi.org/10.1016/j.addma.2017.12.002.

[47]   E.M. Palmero, A. Bollero, 3D and 4D Printing of Functional and Smart Composite Materials, in: D. Brabazon (Ed.), Encyclopedia of Materials: Composites, Elsevier, Oxford, 2021: pp. 402–419. https://doi.org/10.1016/B978-0-12-819724-0.00008-2.

[48]   J. Wong, A. Altassan, D.W. Rosen, Additive manufacturing of fiber-reinforced polymer composites: A technical review and status of design methodologies, Composites Part B: Engineering 255 (2023) 110603. https://doi.org/10.1016/j.compositesb.2023.110603.

[49]   K. Ruan, Y. Peng, Y. Weng, L. Zhou, Y. Xiong, Rotatory additive manufacturing of grid-stiffened continuous fiber-reinforced polymer tubular structures, Composites Part A: Applied Science and Manufacturing 194 (2025) 108896. https://doi.org/10.1016/j.compositesa.2025.108896.

[50]   D. Arslan, M. Mihai, D. Therriault, M. Lévesque, Formulation and characterization of polyetherimide composites reinforced with recycled carbon fibers and thermal black particles for fused filament fabrication, Composites Part A: Applied Science and Manufacturing 194 (2025) 108946. https://doi.org/10.1016/j.compositesa.2025.108946.

[51]   I. Mahapatra, N. Chikkanna, K. Shanmugam, J. Rengaswamy, V. Ramachandran, Evaluation of tensile properties of 3D-printed lattice composites: Experimental and machine learning-based predictive modelling, Composites Part A: Applied Science and Manufacturing 193 (2025) 108823. https://doi.org/10.1016/j.compositesa.2025.108823.

[52]   S.K. Everton, M. Hirsch, P. Stravroulakis, R.K. Leach, A.T. Clare, Review of in-situ process monitoring and in-situ metrology for metal additive manufacturing, Materials & Design 95 (2016) 431–445. https://doi.org/10.1016/j.matdes.2016.01.099.

[53]   C. Wang, X.P. Tan, S.B. Tor, C.S. Lim, Machine learning in additive manufacturing: State-of-the-art and perspectives, Additive Manufacturing 36 (2020) 101538. https://doi.org/10.1016/j.addma.2020.101538.

[54]   S.M. Thompson, L. Bian, N. Shamsaei, A. Yadollahi, An overview of Direct Laser Deposition for additive manufacturing; Part I: Transport phenomena, modeling and diagnostics, Additive Manufacturing 8 (2015) 36–62. https://doi.org/10.1016/j.addma.2015.07.001.

[55]   T.D. Ngo, A. Kashani, G. Imbalzano, K.T.Q. Nguyen, D. Hui, Additive manufacturing (3D printing): A review of materials, methods, applications and challenges, Composites Part B: Engineering 143 (2018) 172–196. https://doi.org/10.1016/j.compositesb.2018.02.012.

[56]   A. Alfaify, M. Saleh, F.M. Abdullah, A.M. Al-Ahmari, Design for Additive Manufacturing: A Systematic Review, Sustainability 12 (2020) 7936. https://doi.org/10.3390/su12197936.

[57]   T. DebRoy, H.L. Wei, J.S. Zuback, T. Mukherjee, J.W. Elmer, J.O. Milewski, A.M. Beese, A. Wilson-Heid, A. De, W. Zhang, Additive manufacturing of metallic components – Process, structure and properties, Progress in Materials Science 92 (2018) 112–224. https://doi.org/10.1016/j.pmatsci.2017.10.001.

[58]   R. Bendikiene, A. Ciuplys, L. Kavaliauskiene, Circular economy practice: From industrial metal waste to production of high wear resistant coatings, Journal of Cleaner Production 229 (2019) 1225–1232. https://doi.org/10.1016/j.jclepro.2019.05.068.

[59]   J.-P. Kruth, G. Levy, F. Klocke, T.H.C. Childs, Consolidation phenomena in laser and powder-bed based layered manufacturing, CIRP Annals 56 (2007) 730–759. https://doi.org/10.1016/j.cirp.2007.10.004.

[60]   J. Coulthard, C.J. Wang, Generative Design and Topology Optimisation of Products for Additive Manufacturing, in: Advances in Manufacturing Technology XXXV, IOS Press, 2022: pp. 81–86. https://doi.org/10.3233/ATDE220570.

[61]   M. Attaran, The rise of 3-D printing: The advantages of additive manufacturing over traditional manufacturing, Business Horizons 60 (2017) 677–688. https://doi.org/10.1016/j.bushor.2017.05.011.

[62]   Multifunctional Mechanical Metamaterials Based on Triply Periodic Minimal Surface Lattices - Al-Ketan - 2019 - Advanced Engineering Materials - Wiley Online Library, (n.d.). https://advanced.onlinelibrary.wiley.com/doi/abs/10.1002/adem.201900524 (accessed June 14, 2025).

[63]   Y. Hwang, Recent Advances in Additively Manufactured Heat Exchangers, (2019). https://www.academia.edu/120118978/Recent_Advances_in_Additively_Manufactured_Heat_Exchangers (accessed June 14, 2025).

[64]   H. Yin, W. Zhang, L. Zhu, F. Meng, J. Liu, G. Wen, Review on lattice structures for energy absorption properties, Composite Structures 304 (2023) 116397. https://doi.org/10.1016/j.compstruct.2022.116397.

[65]   M. Leary, 5 - Design of lattice and zero-mean curvature structures, in: M. Leary (Ed.), Design for Additive Manufacturing, Elsevier, 2020: pp. 123–163. https://doi.org/10.1016/B978-0-12-816721-2.00005-1.

[66]   K.-M. Park, K.-S. Min, Y.-S. Roh, Design Optimization of Lattice Structures under Compression: Study of Unit Cell Types and Cell Arrangements, Materials 15 (2022) 97. https://doi.org/10.3390/ma15010097.

[67]   M. f Ashby, The properties of foams and lattices, Philosophical Transactions of the Royal Society A: Mathematical, Physical and Engineering Sciences 364 (2005) 15–30. https://doi.org/10.1098/rsta.2005.1678.

[68]   N. Kladovasilakis, K. Tsongas, D. Karalekas, D. Tzetzis, Architected Materials for Additive Manufacturing: A Comprehensive Review, Materials 15 (2022) 5919. https://doi.org/10.3390/ma15175919.

[69]   Y. Chen, Y. Ma, P. Liu, Y. Chen, Mechanical Properties of Lattice Structures With a Central Cube: Experiments and Simulations, (2024). https://doi.org/10.20944/preprints202401.2190.v1.

[70]   F. Di Caprio, S. Franchitti, R. Borrelli, C. Bellini, V. Di Cocco, L. Sorrentino, Ti-6Al-4V Octet-Truss Lattice Structures under Bending Load Conditions: Numerical and Experimental Results, Metals 12 (2022) 410. https://doi.org/10.3390/met12030410.

[71]   A counter-example to Kelvin's conjecture on minimal surfaces, (n.d.). https://www.periodicos.capes.gov.br/index.php/acervo/buscador.html?id=W2058123643&task=detalhes&utm_source=chatgpt.com (accessed June 15, 2025).

[72]   L.J. Gibson, M.F. Ashby, Cellular Solids: Structure and Properties, 2nd ed., Cambridge University Press, Cambridge, 1997. https://doi.org/10.1017/CBO9781139878326.

[73]   X. Xiao, S. Joshi, Process planning for five-axis support free additive manufacturing, Additive Manufacturing 36 (2020) 101569. https://doi.org/10.1016/j.addma.2020.101569.

[74]   F. Veloso, J. Gomes-Fonseca, P. Morais, J. Correia-Pinto, A.C.M. Pinho, J.L. Vilaça, Overview of Methods and Software for the Design of Functionally Graded Lattice Structures, Advanced Engineering Materials 24 (2022) 2200483. https://doi.org/10.1002/adem.202200483.

67

[75]   I. Maskery, A.O. Aremu, M. Simonelli, C. Tuck, R.D. Wildman, I.A. Ashcroft, R.J.M. Hague, Mechanical Properties of Ti-6Al-4V Selectively Laser Melted Parts with Body-Centred-Cubic Lattices of Varying cell size, Exp Mech 55 (2015) 1261–1272. https://doi.org/10.1007/s11340-015-0021-5.

[76]   Behance, MT - Asymptotic Gridshells: applications and analysis, Behance (2019). https://www.behance.net/gallery/86066625/MT-Asymptotic-Gridshells-applications-and-analysis (accessed June 18, 2025).

[77]   Y. Guo, K. Liu, Z. Yu, Tetrahedron-Based Porous Scaffold Design for 3D Printing, Designs 3 (2019) 16. https://doi.org/10.3390/designs3010016.

[78]   J. Zhu, H. Zhou, C. Wang, L. Zhou, S. Yuan, W. Zhang, A review of topology optimization for additive manufacturing: Status and challenges, Chinese Journal of Aeronautics 34 (2021) 91–110. https://doi.org/10.1016/j.cja.2020.09.020.

[79]   M. Zhang, C. Liu, M. Deng, Y. Li, J. Li, D. Wang, Graded Minimal Surface Structures with High Specific Strength for Broadband Sound Absorption Produced by Laser Powder Bed Fusion, Coatings 13 (2023) 1950. https://doi.org/10.3390/coatings13111950.

[80]   D. Huang, Z. Li, G. Li, F. Zhou, G. Wang, X. Ren, J. Su, Biomimetic structural design in 3D-printed scaffolds for bone tissue engineering, Materials Today Bio 32 (2025) 101664. https://doi.org/10.1016/j.mtbio.2025.101664.

[81]   N. Khan, A. Riccio, A systematic review of design for additive manufacturing of aerospace lattice structures: Current trends and future directions, Progress in Aerospace Sciences 149 (2024) 101021. https://doi.org/10.1016/j.paerosci.2024.101021.

[82]   J. Yang, H. Liu, G. Cai, H. Jin, Additive Manufacturing and Influencing Factors of Lattice Structures: A Review, Materials 18 (2025) 1397. https://doi.org/10.3390/ma18071397.

[83]   S. Toosi, M.J. Javid-Naderi, A. Tamayol, M.H. Ebrahimzadeh, S. Yaghoubian, S.A. Mousavi Shaegh, Additively manufactured porous scaffolds by design for treatment of bone defects, Front. Bioeng. Biotechnol. 11 (2024). https://doi.org/10.3389/fbioe.2023.1252636.

[84]   Full article: A flexible and easy-to-use open-source tool for designing functionally graded 3D porous structures, (n.d.). https://www.tandfonline.com/doi/full/10.1080/17452759.2022.2048956 (accessed June 19, 2025).

[85]   Three-dimensionally printed vertebrae with different bone densities for surgical training | European Spine Journal, (n.d.). https://link.springer.com/article/10.1007/s00586-018-5847-y (accessed June 19, 2025).

[86]   H. Ramos, R. Santiago, S. Soe, P. Theobald, M. Alves, Response of gyroid lattice structures to impact loads, International Journal of Impact Engineering 164 (2022) 104202. https://doi.org/10.1016/j.ijimpeng.2022.104202.

[87]   O. Al-Ketan, R.K. Abu Al-Rub, Multifunctional Mechanical Metamaterials Based on Triply Periodic Minimal Surface Lattices, Advanced Engineering Materials 21 (2019) 1900524. https://doi.org/10.1002/adem.201900524.

[88]   S. Kavafaki, G. Maliaris, Mechanical Characterization of Triply Periodic Minimal Surface Structures Fabricated via SLA 3D Printing Using Tough Resin: Influence of Geometry on Performance, Engineering Proceedings 87 (2025) 46. https://doi.org/10.3390/engproc2025087046.

[89]   Y. Chen, J.E. Frith, A. Dehghan-Manshadi, H. Attar, D. Kent, N.D.M. Soro, M.J. Bermingham, M.S. Dargusch, Mechanical properties and biocompatibility of porous titanium scaffolds for bone tissue engineering, Journal of the Mechanical Behavior of Biomedical Materials 75 (2017) 169–174. https://doi.org/10.1016/j.jmbbm.2017.07.015.

[90]   C. Koplin, E. Schwarzer-Fischer, E. Zschippang, Y.M. Löw, M. Czekalla, A. Seibel, A. Rörich, J. Georgii, F. Güttler, S. Yarar-Schlickewei, A. Kailer, Design of Reliable Remobilisation Finger Implants with Geometry Elements of a Triple Periodic Minimal Surface Structure via Additive Manufacturing of Silicon Nitride, J 6 (2023) 180–197. https://doi.org/10.3390/j6010014.

[91]   M. Rezapourian, I. Jasiuk, M. Saarna, I. Hussainova, Selective laser melted Ti6Al4V split-P TPMS lattices for bone tissue engineering, International Journal of Mechanical Sciences 251 (2023) 108353. https://doi.org/10.1016/j.ijmecsci.2023.108353.

[92]   M.G. Gado, O. Al-Ketan, M. Aziz, R.A. Al-Rub, S. Ookawara, Triply Periodic Minimal Surface Structures: Design, Fabrication, 3D Printing Techniques, State-of-the-Art Studies, and Prospective Thermal Applications for Efficient Energy Utilization, Energy Technology 12 (2024) 2301287. https://doi.org/10.1002/ente.202301287.

[93]   M. Mazur, M. Leary, M. McMillan, S. Sun, D. Shidid, M. Brandt, 5 - Mechanical properties of Ti6Al4V and AlSi12Mg lattice structures manufactured by Selective Laser Melting (SLM), in: M. Brandt (Ed.), Laser Additive Manufacturing, Woodhead Publishing, 2017: pp. 119–161. https://doi.org/10.1016/B978-0-08-100433-3.00005-1.

[94]   Z. Wang, M. Zhang, Z. Liu, Y. Wang, W. Dong, S. Zhao, D. Sun, Biomimetic design strategy of complex porous structure based on 3D printing Ti-6Al-4V scaffolds for enhanced osseointegration, Materials & Design 218 (2022) 110721. https://doi.org/10.1016/j.matdes.2022.110721.

[95]   Y. Wan, N. Qiu, M. Xiao, Y. Xu, J. Fang, Energy dissipation of 3D-printed TPMS lattices under cyclic loading, International Journal of Mechanical Sciences 294 (2025) 110245. https://doi.org/10.1016/j.ijmecsci.2025.110245.

[96]   W. Tang, H. Zhou, Y. Zeng, M. Yan, C. Jiang, P. Yang, Q. Li, Z. Li, J. Fu, Y. Huang, Y. Zhao, Analysis on the convective heat transfer process and performance evaluation of Triply Periodic Minimal Surface (TPMS) based on Diamond, Gyroid and Iwp, International Journal of Heat and Mass Transfer 201 (2023) 123642. https://doi.org/10.1016/j.ijheatmasstransfer.2022.123642.

[97]   F.S.L. Bobbert, K. Lietaert, A.A. Eftekhari, B. Pouran, S.M. Ahmadi, H. Weinans, A.A. Zadpoor, Additively manufactured metallic porous biomaterials based on minimal surfaces: A unique combination of topological, mechanical, and mass transport properties, Acta Biomater 53 (2017) 572–584. https://doi.org/10.1016/j.actbio.2017.02.024.

[98]   M. Benedetti, A. du Plessis, R.O. Ritchie, M. Dallago, N. Razavi, F. Berto, Architected cellular materials: A review on their mechanical properties towards fatigue-tolerant design and fabrication, Materials Science and Engineering: R: Reports 144 (2021) 100606. https://doi.org/10.1016/j.mser.2021.100606.

[99]   Assessing the mechanical and energy absorption capabilities of lattice structures of F-RD and Fischer–Koch S triply periodic minimal surfaces | Progress in Additive Manufacturing, (n.d.). https://link.springer.com/article/10.1007/s40964-025-01142-0?utm_source=chatgpt.com (accessed June 16, 2025).

[100]   Robocasting of Ceramic Fischer–Koch S Scaffolds for Bone Tissue Engineering, (n.d.). https://www.mdpi.com/2079-4983/14/5/251?utm_source=chatgpt.com (accessed June 16, 2025).

[101]   Energy absorption of 3D printed stochastic lattice structures under impact loading – design parameters, manufacturing, and testing | Progress in Additive Manufacturing, (n.d.). https://link.springer.com/article/10.1007/s40964-025-01094-5?utm_source=chatgpt.com (accessed June 16, 2025).

[102]   Design of Stochastic Lattice Structures for Additive Manufacturing | MSEC | ASME Digital Collection, (n.d.). https://asmedigitalcollection.asme.org/MSEC/proceedings-abstract/MSEC2020/84256/V001T01A036/1095616 (accessed June 16, 2025).

[103]   T. Deng, S. Gong, Y. Cheng, J. Wang, H. Zhang, K. Li, Y. Nie, B. Shen, Stochastic lattice-based porous implant design for improving the stress transfer in unicompartmental knee arthroplasty, J Orthop Surg Res 19 (2024) 499. https://doi.org/10.1186/s13018-024-05006-1.

[104]   J. Ma, Y. Li, Y. Mi, Q. Gong, P. Zhang, B. Meng, J. Wang, J. Wang, Y. Fan, Novel 3D printed TPMS scaffolds: microstructure, characteristics and applications in bone regeneration, Journal of Tissue Engineering (2024). https://doi.org/10.1177/20417314241263689.

[105]   D.W. Abueidda, M. Elhebeary, C.-S. (Andrew) Shiang, R.K. Abu Al-Rub, I.M. Jasiuk, Compression and buckling of microarchitectured Neovius-lattice, Extreme Mechanics Letters 37 (2020) 100688. https://doi.org/10.1016/j.eml.2020.100688.

[106]   I. El Khadiri, M. Abouelmajd, M. Zemzami, N. Hmina, M. Lagache, S. Belhouideg, Comprehensive analysis of flow and heat transfer performance in triply periodic minimal surface (TPMS) heat exchangers based on Fischer-Koch S, PMY, FRD, and Gyroid structures, International Communications in Heat and Mass Transfer 156 (2024) 107617. https://doi.org/10.1016/j.icheatmasstransfer.2024.107617.

[107]   S.-Y. Park, K.-S. Kim, B. AlMangour, D. Grzesiak, K.-A. Lee, Effect of unit cell topology on the tensile loading responses of additive manufactured CoCrMo triply periodic minimal surface sheet lattices, Materials & Design 206 (2021) 109778. https://doi.org/10.1016/j.matdes.2021.109778.

[108]   T. Liu, W. Zhao, Y. Yao, C. Lin, H. Zhao, J. Cai, Mechanical and shape-memory properties of TPMS with hybrid configurations and materials, International Journal of Smart and Nano Materials (2024). https://www.tandfonline.com/doi/abs/10.1080/19475411.2024.2410289 (accessed June 19, 2025).

[109]   D. Mahmoud, M.A. Elbestawi, Lattice Structures and Functionally Graded Materials Applications in Additive Manufacturing of Orthopedic Implants: A Review, Journal of Manufacturing and Materials Processing 1 (2017) 13. https://doi.org/10.3390/jmmp1020013.

[110]   M. Karimzadeh, D. Basvoju, A. Vakanski, I. Charit, F. Xu, X. Zhang, Review of Machine Learning Methods for Additive Manufacturing of Functionally Graded Materials, Materials 17 (2024) 3673. https://doi.org/10.3390/ma17153673.

[111]   Z. Xu 'Loker, N. Razavi, M.R. Ayatollahi, Functionally Graded Lattice Structures: Fabrication Methods, Mechanical Properties, Failure Mechanisms and Applications, in: Reference Module in Materials Science and Materials Engineering, 2022. https://doi.org/10.1016/B978-0-12-822944-6.00019-0.

[112]   Additively Manufactured Functionally Graded Lattices: Design, Mechanical Response, Deformation Behavior, Applications, and Insights | JOM, (n.d.). https://link.springer.com/article/10.1007/s11837-023-06190-x?utm_source=chatgpt.com (accessed June 16, 2025).

[113]   N. Khan, A. Riccio, A systematic review of design for additive manufacturing of aerospace lattice structures: Current trends and future directions, Progress in Aerospace Sciences 149 (2024) 101021. https://doi.org/10.1016/j.paerosci.2024.101021.

[114]   The Mechanical Properties of Functionally Graded Lattice Structures Derived Using Computer-Aided Design for Additive Manufacturing, (n.d.). https://www.mdpi.com/2076-3417/13/21/11667?utm_source=chatgpt.com (accessed June 16, 2025).

[115]   Y. Li, Z. Feng, L. Hao, L. Huang, C. Xin, Y. Wang, E. Bilotti, K. Essa, H. Zhang, Z. Li, F. Yan, T. Peijs, A Review on Functionally Graded Materials and Structures via Additive Manufacturing: From Multi-Scale Design to Versatile Functional Properties, Advanced Materials Technologies 5 (2020) 1900981. https://doi.org/10.1002/admt.201900981.

[116]   C. Tan, J. Zou, S. Li, P. Jamshidi, A. Abena, A. Forsey, R.J. Moat, K. Essa, M. Wang, K. Zhou, M.M. Attallah, Additive manufacturing of bio-inspired multi-scale hierarchically strengthened lattice structures, International Journal of Machine Tools and Manufacture 167 (2021) 103764. https://doi.org/10.1016/j.ijmachtools.2021.103764.

[117]   Graded-material design based on phase-field and topology optimization | Computational Mechanics, (n.d.). https://link.springer.com/article/10.1007/s00466-019-01736-w (accessed June 16, 2025).

[118]   J. Noronha, M. Leary, M. Brandt, M. Qian, AlSi10Mg hollow-strut lattice metamaterials by laser powder bed fusion, Mater. Adv. 5 (2024) 3751–3770. https://doi.org/10.1039/D3MA00813D.

[119]   M. Shinde, I.E. Ramirez-Chavez, D. Anderson, J. Fait, M. Jarrett, D. Bhate, Towards an Ideal Energy Absorber: Relating Failure Mechanisms and Energy Absorption Metrics in Additively Manufactured AlSi10Mg Cellular Structures under Quasistatic Compression, Journal of Manufacturing and Materials Processing 6 (2022) 140. https://doi.org/10.3390/jmmp6060140.

[120]   I. Maskery, N.T. Aboulkhair, A.O. Aremu, C.J. Tuck, I.A. Ashcroft, R.D. Wildman, R.J.M. Hague, A mechanical property evaluation of graded density Al-Si10-Mg lattice structures manufactured by selective laser melting, Materials Science and Engineering: A 670 (2016) 264–274. https://doi.org/10.1016/j.msea.2016.06.013.

[121]   C. Chen, J. Ma, Y. Liu, G. Lian, X. Chen, X. Huang, Compressive behavior and property prediction of gradient cellular structures fabricated by selective laser melting, Materials Today Communications 35 (2023) 105853. https://doi.org/10.1016/j.mtcomm.2023.105853.

[122]   Q. Sun, G. Zhi, S. Zhou, R. Tao, J. Qi, Compressive Mechanical and Heat Conduction Properties of AlSi10Mg Gradient Metamaterials Fabricated via Laser Powder Bed Fusion, Chinese Journal of Mechanical Engineering 37 (2024) 123. https://doi.org/10.1186/s10033-024-01122-5.

[123]   T. Deng, S. Gong, Y. Cheng, J. Wang, H. Zhang, K. Li, Y. Nie, B. Shen, Stochastic lattice-based porous implant design for improving the stress transfer in unicompartmental knee arthroplasty, Journal of Orthopaedic Surgery and Research 19 (2024) 499. https://doi.org/10.1186/s13018-024-05006-1.

[124]   I. Colamartino, M. Anghileri, M. Boniardi, Investigation of the compressive properties of three-dimensional Voronoi reticula, International Journal of Solids and Structures 284 (2023) 112501. https://doi.org/10.1016/j.ijsolstr.2023.112501.

[125]   J.P.M. Cheloni, B. Zluhan, M.E. Silveira, E.B. Fonseca, D.B. Valim, E.S.N. Lopes, Mechanical behavior and failure mode of body-centered cubic, gyroid, diamond, and Voronoi functionally graded additively manufactured biomedical lattice structures, J Mech Behav Biomed Mater 163 (2025) 106796. https://doi.org/10.1016/j.jmbbm.2024.106796.

[126]   D. Mahmoud, M.A. Elbestawi, Lattice Structures and Functionally Graded Materials Applications in Additive Manufacturing of Orthopedic Implants: A Review, Journal of Manufacturing and Materials Processing 1 (2017) 13. https://doi.org/10.3390/jmmp1020013.

[127]   S. Toosi, M.J. Javid-Naderi, A. Tamayol, M.H. Ebrahimzadeh, S. Yaghoubian, S.A. Mousavi Shaegh, Additively manufactured porous scaffolds by design for treatment of bone defects, Front. Bioeng. Biotechnol. 11 (2024). https://doi.org/10.3389/fbioe.2023.1252636.

[128]   Z. Wang, M. Zhang, Z. Liu, Y. Wang, W. Dong, S. Zhao, D. Sun, Biomimetic design strategy of complex porous structure based on 3D printing Ti-6Al-4V scaffolds for enhanced osseointegration, Materials & Design 218 (2022) 110721. https://doi.org/10.1016/j.matdes.2022.110721.

[129]   Stochastic lattice-based porous implant design for improving the stress transfer in unicompartmental knee arthroplasty | Journal of Orthopaedic Surgery and Research | Full Text, (n.d.). https://josr-online.biomedcentral.com/articles/10.1186/s13018-024-05006-1 (accessed June 18, 2025).

[130]   E. Ghio, E. Cerri, Additive Manufacturing of AlSi10Mg and Ti6Al4V Lightweight Alloys via Laser Powder Bed Fusion: A Review of Heat Treatments Effects, Materials (Basel) 15 (2022) 2047. https://doi.org/10.3390/ma15062047.

[131]   N. Top, İ. Şahin, H. Gökçe, The Mechanical Properties of Functionally Graded Lattice Structures Derived Using Computer-Aided Design for Additive Manufacturing, Applied Sciences 13 (2023) 11667. https://doi.org/10.3390/app132111667.

[132]   B. Dangal, S. Jung, The Impact of Additive Manufacturing Constraints and Design Objectives on Structural Topology Optimization, Applied Sciences 13 (2023) 10161. https://doi.org/10.3390/app131810161.

[133]   nTopology, (n.d.). https://ntopology.com.

[134]   K.-M. Park, Kim ,Gil-Oh, Kim ,Jung-Gil, Y. and Roh, Mechanical properties of additive manufactured variable-density Kelvin lattice structures: a novel design method for Kelvin unit cells, Journal of Structural Integrity and Maintenance 7 (2022) 34–45. https://doi.org/10.1080/24705314.2021.1971893.

[135]   Lattice structure optimization and homogenization through finite element analyses - Florian Vlădulescu, Dan Mihai Constantinescu, 2020, (n.d.). https://journals.sagepub.com/doi/10.1177/1464420720945744 (accessed April 8, 2025).

[136]   K.-M. Park, Y.-S. Roh, B.-C. Lee, Effects of the unit-cell size and arrangement on the compressive behaviors of lattice structures in powder bed fusion additive manufacturing, Results in Materials 22 (2024) 100587. https://doi.org/10.1016/j.rinma.2024.100587.

[137]   TruPrint 1000, (n.d.). https://www.trumpf.com/en_INT/products/machines-systems/additive-production-systems/truprint-1000/ (accessed July 8, 2025).

[138]   MDS EOS Aluminium AlSi10Mg, EOS GmbH (n.d.). https://www.eos.info/metal-solutions/metal-materials/data-sheets/mds-eos-aluminium-alsi10mg (accessed July 8, 2025).

[139]   Dragonfly Software for Image Processing and Data Analysis - Dragonfly, (n.d.). https://dragonfly.comet.tech/en (accessed July 8, 2025).

[140]   S. Bieler, K. Weinberg, Energy absorption of sustainable lattice structures under static compression, Meccanica (2025). https://doi.org/10.1007/s11012-025-02003-4.

[141]   L.J. Gibson, M.F. Ashby, Cellular Solids: Structure and Properties, Cambridge University Press, 1997.

[142]   T. Maconachie, M. Leary, B. Lozanovski, X. Zhang, M. Qian, O. Faruque, M. Brandt, SLM lattice structures: Properties, performance, applications and challenges, Materials & Design 183 (2019) 108137. https://doi.org/10.1016/j.matdes.2019.108137.

[143]   Microscopi Elettronici a Scansione (SEM), JEOL (Italia) S.p.A. (n.d.). https://www.jeol.it/microscopi-elettronici-a-scansione-sem/ (accessed July 9, 2025).

[144]   W. Frieden Templeton, S. Hinnebusch, S.T. Strayer, A.C. To, P.C. Pistorius, S.P. Narra, A mechanistic explanation of shrinkage porosity in laser powder bed fusion additive manufacturing, Acta Materialia 266 (2024) 119632. https://doi.org/10.1016/j.actamat.2023.119632.

[145]   M. Sos, G. Meyer, K. Durst, C. Mittelstedt, E. Bruder, Microstructure and mechanical properties of additively manufactured AlSi10Mg lattice structures from single contour exposure, Materials & Design 227 (2023) 111796. https://doi.org/10.1016/j.matdes.2023.111796.

7 Appendix

Table 6) The detailed compression test result

Sample Name	E1 (GPa)	E2 (GPa)	Avg E (GPa)	UCS1 (MPa)	UCS2 (MPa)	Avg UCS (MPa)	EA 1 (J/m³)	EA 2 (J/m³)	Avg EA (J/m³)
GY-CYL-A	4.15	3.58	3.87	150.00	149.29	149.65	27.1	27.46	27.28
GY-CYL-B	3.53	3.43	3.48	117.56	120.63	119.10	18.61	18.87	18.74
GY-CU-A	3.90	3.71	3.81	133.44	133.90	133.67	20.52	20.99	20.76
GY-CU-B	2.91	3.19	3.05	96.81	92.33	94.57	12.13	12.44	12.29
SP-CYL-A	4.04	4.13	4.09	139.96	134.49	137.23	24.18	24.24	24.21
SP-CYL-C	3.48	3.82	3.65	114.62	124.83	119.73	17.52	18.05	17.79
SP-CU-A	4.10	3.69	3.90	123.60	121.90	122.75	22.07	21.59	21.83
SP-CU-C	3.35	3.68	3.52	112.86	111.95	112.41	17.54	17.82	17.68
ST-A	3.66	3.10	3.38	99.50	98.08	98.79	18.85	18.66	18.76
ST-B	2.65	2.41	2.53	64.75	55.89	60.32	9.41	9.98	9.70
ST-C	3.40	3.20	3.30	85.39	80.60	83.00	12.98	11.95	12.47
Bulk	7.6	8.64	8.12	412.26	412.58	412.42	14.64	15.72	15.18

Table 7) The weight of the cubic compression samples.

Sample Name	1st try (g)	2nd try (g)	3rd try (g)	mass (g)
GY-CYL-A	13.11	13.1	13.11	13.11
GY-CYL-B	11.39	11.4	11.42	11.40
GY-CU-A	13.02	13.03	13.04	13.03
GY-CU-B	11.83	11.83	11.83	11.83
SP-CYL-A	13.09	13.07	13.08	13.08
SP-CYL-C	12.29	12.3	12.31	12.30
SP-CU-A	13.11	13.14	13.12	13.12
SP-CU-C	12.36	12.36	12.38	12.37
ST-A	13.03	13.02	13.03	13.03
ST-B	11.83	11.85	11.83	11.84
ST-C	12.33	12.33	12.32	12.33
Bulk	16.95	16.94	16.92	16.94

Table 8) The detailed result of a tensile test, as well as the dog-bone's weight

| Sample Name	E1 (GPa)	E2 (GPa)	E3 (GPa)	Avg E (GPa)	UTS1 (MPa)	UTS2 (MPa)	UTS3 (MPa)	Avg UCS (MPa)	1st (g)	2nd (g)	3rd (g)	mass (g)
GY 1-2 (TB)	3.2	4.93	4.31	4.15	89.71	90.92	101.21	93.95	6.35	6.35	6.35	6.35
SP 0-1.1 (TB)	4.75	4.57	4.8	4.71	84.56	90.62	85.62	86.93	6.32	6.33	6.31	6.32
ST 1-2 (TB)	4.93	5.14	4.21	4.76	104.53	93.94	93.19	97.22	6.31	6.33	6.3	6.31
GY 1-1.5 (TD)	4.69	4.98	5.09	4.92	92.88	87.89	91.98	90.92	6.24	6.23	6.22	6.23
SP 0-0.9 (TD)	5.05	4.55	4.18	4.59	79.72	82.45	78.06	80.08	6.3	6.29	6.29	6.29
ST 1-1.5 (TD)	4.25	5.04	4	4.43	95.61	100.6	95.91	97.37	6.22	6,23	6,19	6.22
GY 0.7-2 (TA)	3.71	4.25	4.3	4.09	59.15	57.18	58.24	58.19	6.19	6.18	6.18	6.18
SP 0-0.7 (TA)	4.89	4.67	4.68	4.75	80.78	78.82	79.72	79.77	6.19	6.2	6.19	6.19
ST 0.7-2 (TA)	4.39	4.01	3.84	4.08	57.64	57.79	56.73	57.39	6.19	6.17	6.17	6.18
GY 0.7-1.5 (TC)	4.24	4.49	3,74	4.37	56.12	57.03	75.79	62.98	6.06	6.05	6.05	6.05
SP 0-0.5 (TC)	4.39	4.53	3.66	4.19	67.62	69.29	68.68	68.53	6.06	6.05	6.07	6.06
ST 0.7-1.5 (TC)	2.58	3.55	3.15	3.09	42.21	50.22	52.49	48.31	6.05	6.03	6.02	6.03
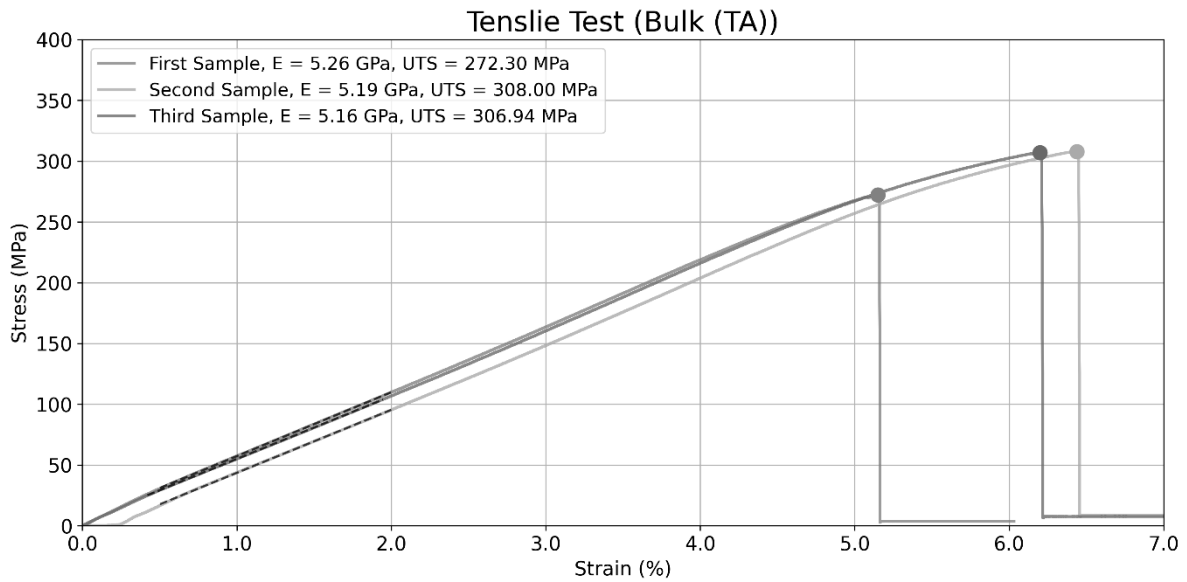
Figure 38) The stress-strain curve of a bulk dog-bone sample as a result of a tensile test.

Table 9) The calculations and C factors for Gibson-Ashby frameworks

	rho*/rho	(rho*/rho)^1.5	sig*/sig	CS	(rho*/rho)^2	E*/E	CE
GY-CYL-A	0.79	70%	37%	0.532797	62%	5.601%	0.089752
GY-CU-A	0.79	70%	33%	0.475919	62%	5.514%	0.088359
SP-CYL-A	0.79	70%	34%	0.488577	62%	5.920%	0.094861
SP-CU-A	0.79	70%	31%	0.43704	62%	5.645%	0.090449
ST-A	0.79	70%	25%	0.351732	62%	4.899%	0.07849
SP-CYL-C	0.75	65%	30%	0.460822	56%	5.290%	0.094042
SP-CU-C	0.75	65%	28%	0.432647	56%	5.094%	0.090564
ST-C	0.75	65%	21%	0.319448	56%	4.783%	0.085024
GY-CYL-B	0.72	61%	30%	0.487343	52%	5.043%	0.097289
GY-CU-B	0.72	61%	24%	0.386985	52%	4.420%	0.085268
ST-B	0.72	61%	15%	0.246833	52%	3.667%	0.07073